1-1-2010

Hybrid Rocket Engine Research In Support Of Prototype Development & Testing

Adam P. Trumpour
Ryerson University

HYBRID ROCKET ENGINE RESEARCH IN SUPPORT OF PROTOTYPE DEVELOPMENT & TESTING

by

Adam P. Trumpour, B.A.Sc., Engineering Science (Aerospace)
University of Toronto, 2005

A thesis submitted to Ryerson University
in partial fulfillment of the
requirements for the degree of
Master of Applied Science
in the program of
Aerospace Engineering

Toronto, Ontario, Canada, 2010

I hereby declare that I am the sole author of this thesis.

I authorize Ryerson University to lend this thesis to other institutions or individuals for the purpose of scholarly research.

Adam Trumpour

I further authorize Ryerson University to reproduce this thesis by photocopying or by other means, in total or in part, at the request of other institutions or individuals for the purpose of scholarly research.

Adam Trumpour

Hybrid Rocket Engine Research in Support of Prototype Development & Testing

Adam Trumpour

Master of Applied Science, Aerospace Engineering, Ryerson University, Toronto, 2010

Abstract

This thesis gives a detailed overview of the design of a small hybrid rocket engine (HRE) that is being built in support of propulsion research activities at Ryerson University, and examines the various research-related issues surrounding the operation and performance of an HRE. The engine design work is undertaken with gaseous oxygen (GOX) as the oxidizer and paraffin and polyethylene as the intended fuels, but the system is readily adaptable to other propellant combinations for future investigations. Particular emphasis was placed on the design and analysis of the GOX injector and the nozzle. The injector orifice design was supported by CFD analysis as well as cold-flow testing. The nozzle was initially designed and fabricated from graphite, but a water-cooled copper design is also considered for those occasions when a fully reusable, non-eroding nozzle is desirable for accurate engine performance measurements. The preliminary nozzle design is supported by a steady-state CFD analysis of the nozzle flows and associated heat fluxes. The overall engine design is further evaluated by examination of internal ballistic simulation results, with respect to such factors as expected performance (chamber pressure, thrust, specific and total impulse) for a given oxidizer mass flow rate and nozzle throat size. The requirements for expected future studies, such as for evaluating engine operation and performance below and above the stoichiometric length of the given engine, have been incorporated where possible into the present design.

Acknowledgments

I must begin by thanking Dr. Greatrix, my supervisor, for giving me the opportunity to pursue this exciting work, and for his constant help, support and advice along the way. Not every thesis supervisor would give their student the chance to actually build a rocket engine, so needless to say, the experience has been truly unique.

To Richard Worsfold and the Ontario Centres of Excellence, for funding this work and the feasibility study that led up to it, go my heartfelt thanks.

Many, many thanks are also due to Jerry Karpynczyk, technical officer at Ryerson University, for helping in so many ways to make this project happen. And for the occasional hot chocolate when it mattered most.

I must also express my great thanks to Dr. Jeff Yokota, Dr. Paul Walsh, and Dr. Jason Lassaline for all their time helping me when Fluent wasn't converging.

To Arny Sokoloff, Dr. Wade Cherrington, Mike Viechweg and all the Continuum Aerospace guys go my thanks not only for their tireless work on the fire control system, casting of fuel grains and logistics of this project, but for so many other things too numerous to mention.

And my deep gratitude to Ken Mason for his many pearls of wisdom, and for putting up with the questions of an eager student.

And last, but by no means least, thanks go to my family for their constant love and support, without which none of this would have been possible. And, Mom and Dad, thanks for never even once complaining about all the hardware that has at one time or another found itself living in the garage.

Adam Trumpour

Ryerson University
April, 2010

Table of Contents

List of Tables

List of Figures

Nomenclature

a:	Empirical regression rate constant
A_e :	Nozzle exit cross-sectional area
A_t :	Nozzle throat cross-sectional area
AP:	Ammonium perchlorate
C:	Orifice discharge coefficient
C_V:	Valve flow coefficient
C_F :	Thrust coefficient
C_f, C_{f0}:	Skin friction coefficient, with and without blowing
C_H:	Stanton number
C_p :	Specific heat
c^* :	Characteristic exhaust velocity
CEA:	NASA Chemical Equilibrium with Applications code
D_c:	Coolant passage hydraulic diameter
D_{port}:	Fuel port hydraulic diameter
D_t:	Nozzle throat diameter
F :	Thrust
f^*:	Zero-transpiration Darcy-Weisbach friction factor
g:	Gravitational acceleration
GOX :	Gaseous oxygen
G:	Total port mass flux
G_{fuel} :	Fuel mass flux
G_{ox} :	Oxidizer mass flux
h:	Convective heat transfer film coefficient
h^*:	Zero transpiration heat transfer coefficient
h_c:	Coolant-side convective heat transfer coefficient
h_g:	Gas-side convective heat transfer coefficient
h_v:	Total heat of fuel vaporization
HDPE:	High density polyethylene
HRE :	Hybrid rocket engine
I_{sp} :	Specific impulse
I_{vac}:	Vacuum specific impulse
k :	Thermal conductivity
k_c:	Coolant thermal conductivity
k_g:	Gas phase conductivity
k_{wall}:	Nozzle wall thermal conductivity
L:	Fuel grain length
l_i:	Orifice length
L_{st}:	Stoichiometric length
LDPE:	Low-density polyethylene
LOX :	Liquid oxygen
$\mathfrak{M}$:	Molecular weight
$\dot{m}$:	Mass flow rate
$\dot{m}_{fuel}$:	Fuel mass flow rate

$\dot{m}_{ox}$: Oxidizer mass flow rate
Ma_e : Nozzle exit Mach number
N_{faces}: Number of faces enclosing a cell
n: Empirical regression rate exponent
Nu: Nusselt number
O/F : Ratio of oxidizer to fuel mass flow rates
P: Fuel port perimeter
p_c : Forward combustion chamber pressure
p_e : Nozzle exit pressure
p_a: Ambient pressure
PMMA: Polymethyl methacrylate
Pr: Prandtl number
$\dot{Q}_c$: Convective heat transfer from flame zone
$\dot{Q}_s$: Heat transfer to fuel surface
$q(\lambda_2)$: Gasdynamic function (injector calculations)
QSHYB: Ryerson *Q*uasi-*S*teady *HYB*rid rocket internal ballistics simulation program
R: Specific gas constant, or effective recovery factor, or nozzle throat radius of curvature
r: Local recovery factor
r_b : Solid fuel surface regression rate
Re: Reynolds number
S_ϕ: Source of ϕ per unit volume
T_{aw}: Adiabatic wall temperature
T_c: Core (freestream) gas temperature
T_f: Combustion (flame) temperature
T_s: Fuel surface temperature
T_{wc}: Coolant-side wall temperature
T_{wg}: Gas-side wall temperature
T_{wall}: Nozzle wall thickness
u: Velocity
u_e: Velocity at edge of boundary layer
UHMWPE: Ultra-high molecular weight polyethylene
v: Gas velocity normal to fuel surface
V: Cell volume
Y: Gas expansion factor

Greek Symbols
β: Blowing coefficient, or ratio of orifice diameter to inlet diameter
Δh: Enthalpy change
γ : Gas ratio of specific heats
ε : Nozzle expansion ratio, or effective propellant surface roughness height
ε/D: Relative surface roughness height
ϕ: A given flow property
ϕ_f: Value of ϕ convected through face f
η_{c^*} : c* efficiency

Γ_ϕ: Diffusion coefficient for ϕ
θ_{cn}: Nozzle exit cone half-angle
λ: Nozzle efficiency, or injector passage drag coefficient
λ_2: Injector velocity coefficient
σ: Bartz correction factor
μ: Dynamic viscosity, or flow coefficient
ν: Kinematic viscosity
ρ_e: Gas density at edge of boundary layer
ρ_f: Solid fuel density
ζ_i: Injector hydraulic loss coefficient

1. Introduction

1.1 Background

Hybrid rocket engines (HREs) are a class of rocket propulsion system that have garnered considerable interest in recent years due to a unique combination of potential advantages as compared to the more conventional all-solid and all-liquid propellant rockets. These advantages include a high degree of environmental cleanliness, safety, controllability, simplicity and ease of manufacturing, all of which contribute to low cost of manufacture and operation.

As their name suggests, HREs employ both a solid and a liquid propellant, most commonly a liquid oxidizer and a solid fuel. In a "classical" HRE, the fuel grain is cast in a combustion chamber and typically contains one or more axial ports along which combustion occurs. The oxidizer is injected into the fuel port(s) at the head end, and an exhaust nozzle accelerates the gas or gas-particle combustion products rightward out of the aft end, producing thrust. This basic configuration is illustrated in Figure 1.1.

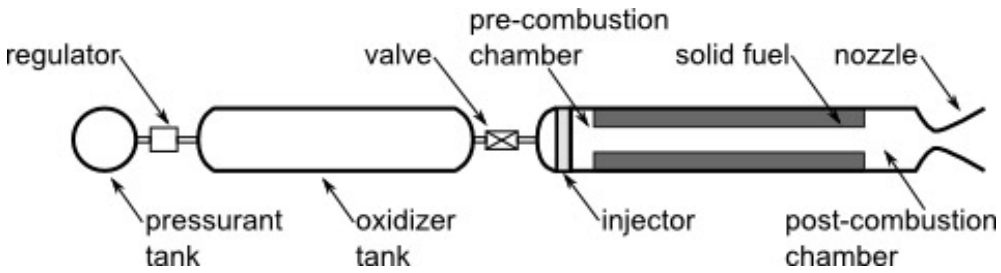

Figure 1.1: Classical HRE configuration

These engines potentially offer higher specific impulse (I_{sp}) and much greater controllability than solid rocket motors, yet greater simplicity and thus potentially lower cost than liquid rocket engines. They are also characterized by increased safety due to the fact that the fuel and oxidizer are stored in different phases and are thus much less likely to form explosive mixtures in the event of a malfunction. As such, they have generated considerable interest for various rocket propulsion applications in recent years[1-3].

However, unlike solid rockets, whose fuel and oxidizer are pre-mixed, or liquid rockets, where propellant mixing and combustion occurs at the droplet scale, hybrid combustion takes place in a macroscopic turbulent boundary layer down the length of the fuel grain. This mechanism tends to lead to lower mixing and combustion efficiencies. The nature of this turbulent diffusion flame combustion mechanism also makes its internal ballistics somewhat more difficult to model accurately than either a traditional solid- or liquid-propellant rocket[1, 3]. Finally, the fuel surface regression rate of an HRE also tends to be significantly lower than that of a solid-propellant rocket motor, often necessitating either complicated fuel grain geometries or an otherwise more elaborate engine design in order to provide a sufficient burning surface area to achieve target thrust levels. This becomes progressively more problematic as engines are scaled to larger sizes, and the added complexity can negate many of the advantages of a classical HRE[2-4].

In recent years, researchers at several institutions have noted that paraffin-based fuels exhibit regression rates three to four times those of conventional HRE fuels, a finding that has prompted new empirical and analytical regression-rate models for this class of fuels[2-6]. Recent work at Ryerson University, building on prior experience modeling erosive burning in solid rocket motors, has led to the development of an internal ballistic simulation computer program (QSHYB) for performance prediction of HREs, including fuel regression rate predictions for a range of fuels, including paraffins[7,8]. To date, the program has shown good agreement with experimental data in a number of cases[7,9].

To assess further and to refine the Ryerson HRE internal ballistics model, and to explore the characteristics of innovative fuels and oxidizer injection methods, an experimental test firing capability is desirable. This thesis presents the design, development, modeling and initial testing of a laboratory-scale HRE for use at Ryerson University. This setup provides the core infrastructure required to test a range of HRE configurations and propellant combinations, and to contribute to advancing the state of the art in this technology. The configuration of the test engine for initial tests is also presented in this document, with a particular emphasis on the design and analysis of the nozzle and the oxidizer injector.

1.2 Previous Laboratory Hybrid Rocket Engine Studies

Although the basic principles behind hybrid rocket engines have been known at least since the 1930's [2], HRE development work was relatively uncommon over the following

50 years, as the majority of rocket research tended to focus on large, high-performance liquid-propellant rocket engines for military and space launch applications, and on solid-propellant motors for applications benefitting from their storability, simplicity, and high thrust. In spite of this comparatively low level of interest, significant research work was done during the 1960's on HRE development and the development of corresponding internal ballistics models. The 1980's and 1990's saw a considerable increase in HRE research, as it became more widely recognized that the technology can potentially occupy a significant niche as a low-cost alternative to liquid rocket engines, in cases where controllability and safety are important. A significant amount of this research has been occurring in academia, as a growing number of universities have sought to study the mechanisms of hybrid rocket combustion and performance. Several universities have developed small, laboratory-scale hybrid rocket engines using a range of configurations and a range of propellant combinations. A survey of some of these projects, the experimental facilities they produced, and the research they enabled, serves as a solid reference point for the present work.

The paper by Schulze and Meyer (1991)[10] presents information on a small-scale hybrid rocket engine development effort that is pertinent to this thesis. Similar to the present thesis, the project's goal was to develop a small, low-cost HRE using off-the-shelf components for research purposes, as a technology demonstrator, and ultimately as a viable propulsion system for a flight vehicle. This was accomplished over the course of 6 months, including 7 test firings. The engine employed gaseous oxygen (GOX) as the oxidizer and low-cost, recycled high-density polyethylene (HDPE) as the fuel. Initially,

3 tests were conducted using a 2-inch (50.8 mm) diameter, Schedule 40 galvanized steel pipe with threaded ANSI class 150 flanges to verify the effectiveness of the oxidizer feed system, ignition system and instrumentation, and to gather data to size a more optimized thrust chamber for the 4 subsequent tests. This refined test engine employed a flanged Varian stainless steel ultra-high vacuum chamber with 0.060 in. (1.52 mm) walls as the combustion chamber, a 2.36 in. (59.94 mm) diameter, 11.5 in. (292.1 mm) length HDPE fuel grain, a glass-filled phenolic post-combustion chamber, and an isomolded ATJ graphite nozzle bonded and sealed in place using RTV silicone. Ignition was accomplished via a commercial Estes C6 or A3 solid rocket motor mounted in a housing at the head end. Control and measurement of the GOX flow rate in these tests was rudimentary, employing a needle valve to allow adjustment of the flow, calibrated at 1.5 turns, but lacking any means for measuring the actual mass or volume flow rate during a test. GOX was fed at a 300 psig (2.068 MPa) pressure, with varying GOX needle valve settings and a chamber pressure of around 100 psig (0.690 MPa) for the test engine. The typical burn duration was 15 seconds, with observed fuel regression rates of about 0.00155 in/s (0.0394 mm/s). Erosion of the graphite nozzle throat was considerable, estimated at about 0.0385 in/s (0.978 mm/s), due to oxidation, despite the fact that the combustion mixture was on the fuel-rich side. Chamber pressures for the initial pipe engine were allowed to go as high as 220 psig (1.517 MPa), yielding an average regression rate of 0.0155 in/s (0.394 mm/s), flame temperature of 4500°F (2755 K), and significant nozzle erosion.

Recognizing the problem of low regression rate in traditional HTPB rubber-based HRE fuels, a team from the University of Arkansas at Little Rock[11] employed a lab-scale HRE to conduct a survey of potential hydrocarbon fuel additives and assess their effect on regression rate. The additives considered were paraffin, norbornylene and naphthalene, chosen on the basis of their containing only carbon and hydrogen, having a lower pyrolysis / vaporization energy than pure HTPB, and not interfering with polymerization. The additives were cast, 40% by mass, with HTPB and 1% graphite opacifier in a 10 in. (254 mm) paper phenolic liner with 0.75 in. (19.05 mm) central port. The resulting fuel grains were fired in the university's lab-scale HRE, which consists of a 2 in. x 10 in. (50.8 mm x 254 mm) thrust chamber capable of operating at pressures up to 500 psi (3.448 MPa) and GOX flows up to 0.16 lb/s (0.073 kg/s).

All burns were conducted for 3 seconds, with the exception of a single 6-second burn. It was found that the 40% paraffin grains showed little difference in regression compared to pure HTPB, at oxygen fluxes from 0.0789 to 0.2337 lbm/in^2-s (55.4 to 164.3 kg/m^2-s) and corresponding regression rates from 0.02865 to 0.07895 in/s (0.7277 to 2.005 mm/s), at chamber pressures ranging from 200 to 400 psi (1.379 to 2.758 MPa). 40% naphthalene was found to only yield about a 10% increase in regression rate over pure HTPB. The grains were tested at oxygen fluxes from 0.0571 to 0.2316 lbm/in^2-s and corresponding regression rates from 0.02428 to 0.06920 in/s (0.6167 to 1.7577 mm/s), at chamber pressures ranging from 150 to 450 psi (1.034 to 3.103 MPa). Due to the difficulty in manufacturing the grains stemming from its high sublimation, naphthalene was deemed an impractical HRE fuel additive. Norbornylene was not fired due to safety

concerns stemming from the high degree of sublimation it experienced, and the resulting low flash point and offensive odor.

The study by Yuasa *et al* (1999)[12] at the Tokyo Metropolitan Institute of Technology considered an alternate approach to improving HRE regression rate performance: the use of swirl injection. A laboratory-scale HRE employing GOX and transparent PMMA (polymethyl methacrylate or Plexiglas) fuel was constructed to enable this work, and about 50 firings were carried out for the evaluation of the technique. Due to the transparent fuel grain, spectroscopy was used to analyze the combustion products. Rapid ignition and stable combustion were observed, largely independent of swirl intensity, while regression rate was found to be strongly dependent on injector geometry, and increased significantly with increasing swirl intensity due to the increased oxygen flow velocity and gas density near the wall of the fuel grain. The swirl succeeded in reducing the thickness of the boundary layer over the fuel grain surface due to the additional tangential velocity component near the surface, while also providing an increase in pressure. It additionally has the potential of increasing the residence time of the combustion gases in the chamber, thereby improving combustion efficiency. The laboratory-scale test engine for the study incorporated a PMMA fuel grain with 150 mm length and 40 mm inner diameter, inserted in a motor case that was also constructed from PMMA. The nozzle section was made from oxygen-free copper, with a 10.5 mm throat diameter. As with Schulze and Meyer (1993)[10], ignition was achieved using a small Estes solid rocket motor. The GOX mass flow was held constant at 22 g/s using a calibrated choking orifice, and burn durations were 10 s. Instrumentation allowed the

measurement of nozzle throat wall temperature, thrust and chamber pressure, in addition to spectral observation of the combustion process. Chamber pressure varied with swirl number Sg from 0.35 MPa for no swirl, to a maximum of 0.52 MPa for Sg = 5, with regression rate varying from 0.20 mm/s (Sg = 0) to 0.33 mm/s (Sg = 5). The theoretical peak thrust for the engine was 78 N, though actual performance was lower than this, increasing with Sg but still limited due to insufficient vaporization of fuel. One complication that was observed was highly uneven erosion of the fuel grain, due to oxidizer impingement on the wall near the head end.

In a follow-on to their previous work, the Tokyo Metropolitan Institute of Technology team's laboratory-scale HRE[13] received a modified injector that avoided GOX impingement on the fuel grain wall. Investigating the axial variation of regression rate using the new injector in the old 150 mm long chamber yielded expressions for regression rate as a function of length at a range of Sg values. These expressions allowed the determination of an optimum fuel grain length of 450 mm. Using this grain length and this injector, the delivered *Isp* was found to be as high as 97% of the theoretical value.

The study by Corpening *et al* (2003)[14], carried out at Purdue University, developed a laboratory-scale HRE for a series of tests involving 98% H_2O_2 with dicyclopentadiene (DCPD), and lithium aluminum hydride (LAH)-loaded DCPD. DCPD was found to offer superior regression performance compared to a baseline H_2O_2 / low-density polyethylene (LDPE) grain and comparable performance to HTPB. The LAH-loaded grains showed

no marked increase in regression performance, but low combustion efficiency, ranging from 63-80%. The test engine was fabricated from 1.5 in. (38.1 mm) Schedule 40 steel pipe 17 inches (431.8 mm) in length, with an ANSI class 150 flange welded to either end and protected by a paper phenolic liner. A class 150 stainless steel flange closed out the head end and housed a stainless steel spray nozzle as the injector. The first 5 firings were conducted with a silica phenolic nozzle with a hole drilled through as the throat, but this nozzle was found not to be easily reusable, motivating the design of a water-cooled copper nozzle for the last 14 tests. The nozzle incorporated a circumferential water channel with one inlet and one exit, with a ring brazed in place to restrict the area and thus increase the water velocity and the resulting heat transfer. The copper nozzle was housed in a bored-out piece of Schedule 80 stainless steel pipe welded to an ANSI class 150 flange, with ¾ inch tube fittings used for water inlet and exits. A water flow rate of 3.5 lb/s (1.6 kg/s) was calculated to keep the gas side wall temperature around 850 Kelvin, and the water feed system was designed to provide up to 5.5 lb/s (2.5 kg/s) to incorporate a factor of safety. A chamber pressure of 200 psia (1.38 MPa) was targeted for the tests. Burn durations varied from 1.767 to 7.56 seconds, and typical thrust levels were around 20 lbf (89 N).

The team at Stanford University[15] pioneered the investigation of a new class of fuels that offers a novel approach to achieving high regression rates in HREs. These fuels form a liquid melt layer of relatively low viscosity and surface tension that is hydrodynamically unstable and can lead to significant droplet entrainment in the core gas flow in addition to the conventional mechanism of solid fuel gasification. This effect was first observed in

cryogenic solid pentane, and the classical hybrid combustion theory is generalized in this work to account for it. It also suggested that paraffin and PE waxes would exhibit a similar behaviour, and this was corroborated by a series of lab-scale tests. The laboratory-scale HRE used for testing employed GOX as the oxidizer and SP-1, a paraffin-based fuel. The HRE's outer diameter was 3.25 in (82.6 mm), with a fuel port diameter ranging from 0.5 to 1.2 in. (12.7 to 30.5 mm). The nozzle and chamber liner were fabricated from ATJ graphite. A choking orifice was used to fix the oxidizer flow rate, and a methane/GOX torch igniter was used to initiate combustion. Regression rates approximately three times greater than HTPB for a given mass flux were demonstrated, owing to the reduced effective heat of gasification, decreased blocking factor in the boundary layer, and higher heat transfer resulting from increased surface roughness.

In the work reported by Grosse (2009)[16], the development of a laboratory-scale HRE is described, where they employed a perforated diaphragm placed in the midst of the fuel grain as a means of increasing both regression rate and combustion efficiency, while eliminating the need for a post-combustion chamber and its associated weight and loading penalties. Paraffin was employed as the fuel, with chilled N_2O as the oxidizer. The diaphragm was tested at locations 24, 33, 50, 70 and 100% down the grain from the head end, and both single-hole and four-hole configurations were tested. The diaphragm was constructed from carbon-fiber-enforced-carbon (CFC) with a silicon carbide coating, and the ratio of diaphragm opening area to nozzle throat area was held constant at 1.80. The test motor featured a 162 mm length microcrystalline paraffin fuel grain, with an initial port diameter of 29.2 mm. The paraffin was cast as a cylinder with a central steel

mandrel to form the axial port, and cut to length after cooling. A 35 mm long polyethylene splash ring was installed ahead of the grain to straighten the N_2O flow and thereby mitigate the problem of oxidizer impingement on the comparatively high regression rate fuel grain, and a similar, 10-mm retaining ring was inserted between the aft end of the grain and the nozzle in order to protect the grain's end face from regression. The chamber and injector manifold were machined from aluminum, with a high-temperature nickel alloy nozzle housing, containing a high density graphite nozzle, bolted to the aft end. The nozzle was found to experience little to no erosion after a given burn due to the fairly moderate thermal and chemical loads delivered by the paraffin / N_2O propellant combination. Oxidizer injection was via a replaceable industrial swirl injector with 90° full cone angle, and a cavity near the injector contained a 10 to 14 g piece of ammonium perchlorate / HTPB composite propellant as an ignition compound.

Tests were conducted at thrust levels ranging from 200 to 900 N, with burn durations of 3 and 4.5 seconds. Chamber pressure ranged from about 10 to 35 bar (145 to 510 psi). It was noted that locating the diaphragm at the 24 and 33% locations resulted in a noticeable increase in chamber pressure of about 15% over the baseline case, due to the large increase in efficiency and the higher regression rate. The 33% location showed the largest increase in performance. The 1-hole diaphragm delivered an Isp of 202 s, while the 4-hole version offered a slight increase to 206 s. The 1-hole device at the 24% location showed high combustion efficiency, but a lower regression rate downstream than with the 33% location. Both diaphragm configurations at the 50% and 70% locations showed no marked increase in performance over the 24% and 33% locations. The thrust

and combustion efficiencies of all configurations appear to decline with increasing N_2O mass flow or with increasing O/F ratio.

The work by Einav *et al* (2009)[17] presents the development of a laboratory-scale HRE to investigate the effect of ammonium perchlorate (AP) and polystyrene additives on the regression rate behaviour of HTPB. Polystyrene was selected based on the theory that using a material with a vaporization temperature much lower than that of HTPB would result in the production of craters on the burning surface of the fuel, increasing flow turbulence and resulting in an enhanced regression rate. AP was chosen as an oxidizer, along with ferric oxide, a common solid propellant burn rate catalyst. The HRE system was a modular design incorporating a combustion chamber containing the fuel grain, an aft subassembly incorporating a postcombustion chamber and nozzle, and a head end assembly incorporating a precombustion chamber, injector, and methane-oxygen spark igniter. Metallic components were fabricated from low-carbon steel, and the pre- and post-combustion chambers were lined with silica-phenolic sleeves to provide insulation. The fuel grains were 400 mm in length with a single circular port 42 mm in diameter and web thickness of 15 mm. Room temperature N_2O was employed as the oxidizer, with flow rate control provided by a calibrated needle valve. A regulated gaseous N_2 supply was used to supercharge the N_2O to 7 MPa (1015 psia) and a coriolis mass flow rate gauge was used to measure the actual oxidizer mass flow.

Three injector configurations were tested including a 42-orifice, self-impinging doublet configuration employing two concentric rings of orifices with impingement angle of 60°

and an impingement distance of 4.5 mm, a 6-element BETE Fog Nozzle Inc. impingement-on-pin injector, and a Spraying Systems Co. Fogjet model FF fine-spray, multi-nozzle showerhead injector. In cold flow testing, the impingement-on-pin configuration produced the best visual spray quality and was used for the majority of hot-fire tests. The nozzle used for initial tests was a single-piece, medium density graphite design. For later tests, tungsten and pyrolitic graphite throat inserts were used to minimize erosion.

Hot-fire testing indicated that increasing the AP content of the fuel yields an increase in regression rate, with a maximum occurring between 15 and 40% by weight. Above this level, the propellant behaves like a conventional solid propellant and can no longer be extinguished by terminating the oxidizer flow. A significant increase was obtained with the addition of both AP and large particles of polystyrene, with regression rates of up to 3.5 mm/s at 5.5 MPa chamber pressure and average oxidizer mass flux of 140 kg/m^2-s. The addition of polystyrene on its own with no AP showed no significant increase in regression rate.

The work by Carmicino *et al* (2009)[18] presents ongoing European HRE research, where they are employing a laboratory-scale HRE to investigate the effect of aluminum particulate additives on the regression rate performance of HTPB fuels, as well as considering different methods of GOX injection and their effects on combustion efficiency, stability, and regression rate. The HRE employs a flanged combustion chamber that houses the fuel grain and both pre- and post-combustion chambers, as well

as a port at mid-grain to house an ultrasonic transducer for instantaneous regression rate measurements. Two injector configurations were used: a single-orifice axial injector employing a converging nozzle with 8 mm exit diameter, and a radial injector, made by assembling a cap with 16, 2.5 mm diameter radially-drilled orifices onto the injector face. In this design, the pre-combustion chamber is needed to shift the strong recirculation zones caused by axial oxidizer injection toward the fore end of the grain when using the axial injector, as well as to avoid oxidizer impingement on the fuel grain when using the radial injector. Upstream of the injector, a sonic orifice was employed in conjunction with a copper-constantan thermocouple for flow rate measurement, and to decouple the feed system from the combustion chamber dynamics.

The nozzle was fabricated from a copper alloy with 16 mm throat diameter, 82 mm length, and expansion ratio of 2.44. Water cooling was employed to ensure erosion-free operation. Most of the fuel grains tested involved a single cylindrical port, typically 25 mm in diameter though some firings were also conducted with 50 and 75 mm ports. For the final 3 tests, multiport grains were used with 5 25-mm diameter circular ports and a central port with 42-mm diameter. Grain length varied somewhat, from between 539 and 574 mm.

The motor was ignited pyrotechnically, using a small cartridge of a few grams of gunpowder, electrically initiated. Burn durations ranged from 8 to 27.9 s. GOX flow rates ranged from 0.0320 kg/s to 0.2241 kg/s, and chamber pressures ranged from 4.57 to 26.70 atm (67.2 to 392.5 psi). Test results indicated that axial injection results in higher

regression rates for a given fuel, as compared to radial injection. With axial injection, aluminized HTPB did not display a significant increase in regression rate, although it did show a small increase in the radial configuration. Additionally, axial injection yielded higher combustion efficiency in all cases, and stable operation, and no influence of aluminum addition on combustion stability was observed.

The work by Connell *et al* (2009)[19] resulted in the development of a simplified semi-emperical model for the design and parametric optimization of a laboratory-scale HRE in terms of oxidizer flow, chamber pressure and nozzle throat diameter, and the construction of a laboratory-scale HRE to characterize hybrid fuel combinations, initially GOX with PMMA and HTPB fuels. The combustion chamber was fabricated from 304L schedule DXH stainless steel seamless tubing, with injector and aft-end closures machined from 304L stainless steel bar stock. The chamber was a modular design, enabling fuel grains of different lengths to be tested, though a 139.7 mm length (5.5 in) grain was found to be sufficient to provide a 4 s burn duration at a 30 g/s oxidizer flow rate. Fuel grains were cast into paper phenolic tubing. Pre- and post-combustion chambers were lined with medium grade, low-density graphite with inner diameter of 19 mm (0.75 in), outer diameter of 27 mm (1.06 in), and lengths of 38.1 mm (1.5 in) and 76.2 mm (3 in) respectively. Nozzles were machined from isomolded high-density graphite, with a 30° half-angle convergent section and 15° half-angle divergent section. A straight-drilled throat 6.35 mm (0.25 in) in length was used to reduce erosion effects, and the entire unit was sealed with high-temperature Viton o-rings. The oxidizer feed system was designed to allow mass flows of up to 100 g/s, regulated using interchangeable orifices. Typical

chamber pressures ranged from 150 to 200 psig, with thrust levels around 30 N and approximately 6 second burn durations. Measured combustion efficiencies ranged from 89-92%, and regression rates varied from 0.7 to 1.6 mm/s for oxidizer mass fluxes ranging from 60 to 120 kg/m^2-s for HTPB fuel.

1.3 Summary

A growing volume of research in recent years has identified HREs as a potentially significant technology that may help to reduce the costs of space launches. To develop this technology to maturity requires a better understanding of the diffusion flame combustion mechanism and other operational issues that characterize the performance of HREs, and small, laboratory-scale HRE systems have proven their worth in facilitating this. Additionally, research has indicated that paraffin-based fuels offer a potentially significant increase in regression rate performance compared to conventional hybrid fuels such as HTPB (hydroxyl-terminated polybutadiene). Past work at Ryerson University has led to the development of an internal ballistics simulation model for the prediction of HRE performance. In order to help refine this model, the present effort is applied to the design, development and testing of a laboratory-scale HRE for use at Ryerson University.

2. Research Hybrid Rocket Engine Preliminary Design

2.1 Project Objectives

One of the goals of this thesis was to help develop an HRE test facility at RU that is simple, versatile and low-cost, and allows for the rapid acquisition of experimental data for a range of propellant combinations and rocket engine configurations. It was decided early on in the process that this necessitated a prototype sub-scale hybrid rocket engine as the first test item, an engine that was small and safe enough to be operated at University facilities, rather than an elaborate remote test site, while still providing sufficient burn duration to allow for the acquisition of meaningful data. The initial drivers for the HRE design may accordingly be summarized as follows:

1. thrust level suitable for laboratory testing;
2. burn duration long enough to allow for meaningful steady-state operation;
3. appropriate physical size given requirements (1) and (2) above, subject to the need to maintain structural integrity of the fuel grain;
4. maximum use of low-cost, off-the-shelf components;
5. modular design of engine components; and
6. large factors of safety on all pressurized and structural components.

To begin the design process, it was necessary to determine the general configuration and construction of the engine and associated infrastructure, guided by the above constraints. Figure 2.1 illustrates the key features of the setup, as initially conceived.

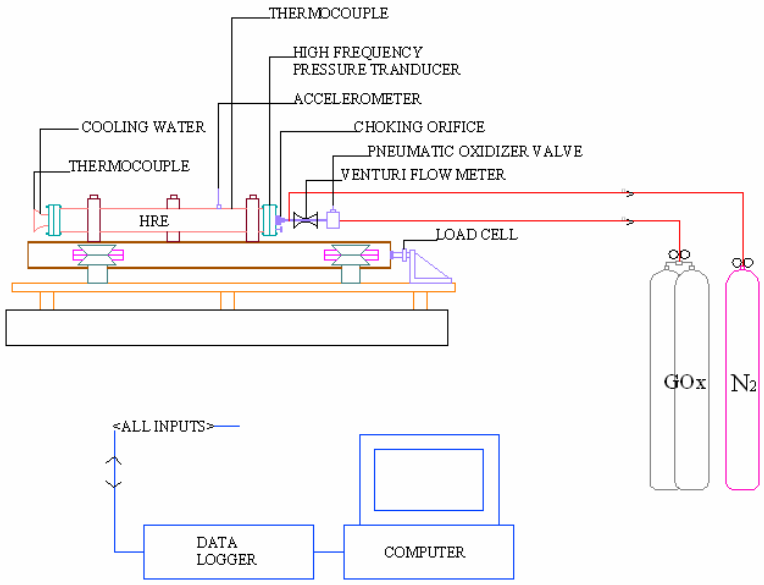

Figure 2.1: Preliminary test setup

To meet the requirements for robustness, modular design and use of off-the-shelf components, it was decided to construct the engine itself using steel flanged pipe. A flanged injector bolts on to the head end, and a retaining ring is bolted into place in the aft end to secure the nozzle. The fuel grain is cast or loaded into an ablative phenolic liner that protects the combustion chamber from the exhaust gases.

2.2 Propellants

2.2.1 Gaseous Oxygen

The oxidizer selected for lab-scale testing was gaseous oxygen (GOX). Liquid oxygen (LOX) was the oxidizer of greatest interest for practical launch vehicle applications, primarily due to its high storage density as a cryogenic oxidizer, relatively high performance and ease of handling compared to some of the more exotic oxidizers, but GOX was preferred for the present laboratory test program due to its availability in small

quantities and substantially simpler handling in the lab, as compared with LOX. The use of GOX also serves to simplify the head-end injector design, allowing research to focus on the combustion processes downstream of the injector plate, and as it is supplied in industrial compressed gas cylinders, it may be fed into the engine without the need of any additional pressurant system.

2.2.2 Fuels

One key advantage of an HRE is that a greater range of potential fuels becomes available than with any other chemical propulsion system, owing to the fact that most materials will combust in a high temperature, high pressure oxidizing environment. True practicality as an HRE fuel however requires two key characteristics. First, the delivered I_{sp} must be sufficiently high to carry out the intended mission. Thermodynamically, this requires as high a heat of combustion as possible. In addition, I_{sp} tends to increase with decreasing molecular weight of the exhaust products, so fuels that are richer in hydrogen tend to offer superior performance. Second, high regression rates are desirable. There are many factors which influence regression rate, but in general lower specific heat capacity, lower thermal conductivity, higher surface roughness, and lower viscosity and surface tension of the melt layer will increase regression.

2.2.2.1 Paraffin Wax

Due to its promising regression rate behaviour, non-toxicity, ready availability and low cost, paraffin wax was selected as a principal fuel constituent for initial testing. Paraffins are a class of alkane hydrocarbons of the form C_nH_{2n+2}, where n is referred to as the carbon number. Commercial paraffin waxes are typically supplied as a blend of paraffins

with a range of carbon numbers n > 20. Work at Stanford University[20] and elsewhere[16, 21] has noted that paraffin waxes produce a melt layer with much lower viscosity and surface tension than traditional hybrid fuels, and that this leads to regression rates 3 to 4 times greater, allowing an HRE using these fuels to achieve higher thrust levels with less burning surface area. This is particularly significant as it allows for a much simpler port geometry than would be possible with slower-regressing fuels. Often, a single cylindrical port is sufficient. While this is less significant at this small scale and low thrust level, it becomes increasingly important as the technology is scaled to larger engine sizes.

The wax selected for the present work was the International Group Inc's IGI 1260 fully-refined paraffin. The paraffin fractions in this blend typically have carbon numbers from 30 to 45, in the fractions specified in Table 2.1:

Table 2.1: IGI 1260 Composition

Carbon #	% mass
30	2.93
31	3.58
32	4.45
33	5.25
34	6.55
35	7.83
36	9.5
37	9.87
38	9.79
39	8.95
40	8.3
41	7.01
42	6.24
43	4.68
44	3.27
45	1.81

For practical use in a HRE, it is usually desirable to add an opacifier to the paraffin to reduce radiative heat transfer from the combustion zone to the bulk of the fuel, which could rapidly soften it and compromise its structural integrity. Carbon black is commonly used for this purpose, in between 0.5% and 2% concentrations by mass. Additional additives may also be employed to tailor the physical properties of the paraffin. Paraffins are typically more brittle than other common hybrid fuels, so additives to reduce brittleness may be desirable. The very low melting temperature and low melt layer viscosity can additionally cause even more of an increase in regression rate than may be desirable, resulting in significant amounts of unburned wax being ejected from the engine. Accordingly, additives to increase melting temperature and/or melt layer viscosity may be desirable. A detailed investigation of fuel chemistry provides an ideal avenue for later work. For initial study purposes, pure IGI 1260 paraffin wax mixed with 2% carbon black, and cast into a cartridge, serves as the baseline fuel.

2.2.2.2 Ultra High Molecular Weight Polyethylene (UHMWPE)

As an additional fuel for early testing, and to provide a point of comparison with the paraffin grains, UHMWPE was selected. Polyethylene is a thermoplastic polymer of ethylene (C_2H_4), having long molecular chains with very little cross-linking. UHMWPE in particular offers extremely long chains and high strength and toughness, as well as relatively high density. For these tests, Tivar® 1000 natural virgin UHMWPE supplied by the Pena-Plas Co. was used. This material has a quoted density of 930 kg/m^3, melting point of 135°C, and thermal conductivity of 0.4099 W/m-K.

2.3 Initial Design Decisions and Thermochemistry

Having selected the propellant combination, the initial design drivers were used to select the HRE operating parameters that are necessary inputs to begin the system design. Requirement (1) placed an upper limit on thrust of about 400 N, while (2) suggested that the burn time should exceed 3 seconds for engines of this scale.

The need for a low-cost, laboratory-scale engine additionally motivated the choice of a chamber pressure (p_c) in the vicinity of 300 psi (2.1 MPa), as a compromise between the desire for high I_{sp}, which increases with pressure, and the desire to operate safely in an academic laboratory environment with readily available GOX hardware, which drove the design value for p_c downwards.

Using NASA's Chemical Equilibrium with Applications (CEA) code[22], thermochemical simulation of the combustion of IGI-1260 paraffin with GOX at the design p_c can be performed. Figure 2.2 illustrates the resulting plot of vacuum and sea-level I_{sp} as a function of oxidizer-to-fuel (O/F) mixture ratio for optimal expansion to atmospheric pressure. Equilibrium reactions were assumed, that is, that the combustion products are allowed to shift arbitrarily fast to maintain chemical equilibrium as they expand and cool through the nozzle. This tends to result in a somewhat high estimate of I_{sp}. The alternative computational approach is assuming frozen flow, in other words that no further shift in the chemical equilibrium occurs during expansion through the nozzle. This approach typically yields a low estimate of I_{sp}.

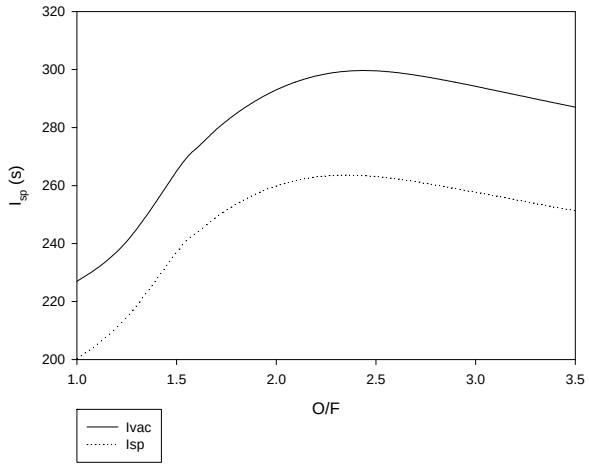

Figure 2.2: Paraffin I_{sp} vs. *O/F* at p_c = 2.1 MPa, optimal expansion, sea level and vacuum cases

Based on Figure 2.2, the optimal *O/F* for GOX/paraffin is approximately 2.5 at the design-point chamber pressure. It is frequently desirable in rocket design to aim for slightly fuel-rich operation in order to reduce the flame temperature and avoid the presence of an oxidizing environment that can greatly diminish the life of chamber and nozzle components. This, combined with the tendency of HREs to exhibit an increase in *O/F* over the course of a firing as the port diameter increases, motivated the selection of an initial nominal design *O/F* of 2.0.

It should be noted that unlike in a solid or liquid rocket, where a desired *O/F* ratio may be easily designed for by varying the physical mixture of oxidizer and fuel in the solid propellant grain, in the case of the former, or by varying the ratio of injected oxidizer to fuel flow rate in the case of the latter, these quantities are not completely independent in an HRE. This will be discussed further. However, the selection of an initial design-point

O/F is a necessary starting point for the design, and it is possible to drive the design towards a desired *O/F* to some extent.

Since initial testing will also involve UHMWPE, an additional thermochemical simulation was performed for this fuel. As the CEA code did not include PE in its database, the Martin Marietta "Propep" code was employed for the purpose. The resulting plot of I_{sp} vs. O/F ratio for PE and GOX at a chamber pressure of 300 psia is illustrated in Figure 2.3.

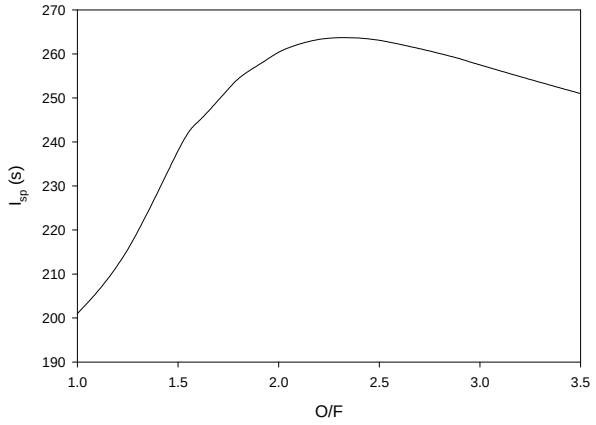

Figure 2.3: Polyethylene I_{sp} vs. *O/F* at p_c = 2.1 MPa, optimal expansion, sea level

The plot indicates that the ideal peak sea level I_{sp} for the GOX-PE combination is very similar to that of paraffin (263.7 s, compared to 263.5 s for paraffin), and occurs at a similar O/F ratio (2.3, as compared to 2.4 for paraffin). It should be noted that the stoichiometric O/F mixture ratio, which provides the peak adiabatic flame temperature with complete reaction of the various chemical constituents, may not align in value with that shown above for peak I_{sp}, given that in many cases, some unreacted products in the exhaust actually help in thrust delivery (e.g., as a result of a lower net gas molecular

weight, even though somewhat cooler). For the above cases, the respective stoichiometric ratios are slightly higher.

For the GOX-paraffin propellant combination at the design *O/F* and p_c, the CEA code was then used to provide estimates of the combustion gas properties assuming that the flow is frozen at the combustion chamber. The gas properties of particular relevance were flame temperature (T_f), ratio of specific heats (γ), molecular weight ($\mathfrak{M}$), specific gas constant (R), specific heat (C_p), dynamic viscosity (μ) and thermal conductivity (k).

2.4 Theoretical Performance Calculations

The parameters determined from thermochemical simulation allow for the calculation of several key rocket performance parameters. A key assumption for the initial design phase, which allows many of these parameters to be expressed by relatively simple thermodynamic functions, is that of the *ideal rocket*. This assumes that:

1. The working fluid is homogeneous
2. The working fluid is an ideal gas
3. The rocket chamber and nozzle are adiabatic
4. The flow is frictionless and boundary layer effects are neglected
5. There are no shock waves or discontinuities in the flow
6. The propellant flow is steady and constant
7. The exit gas velocity is axially-directed
8. The flow is quasi one-dimentional; that is, gas properties are approximately constant over a given cross-section

9. Chemical equilibrium is established in the combustion chamber and does not shift during expansion through the nozzle

Having made these assumptions, the characteristic exhaust velocity (c^*), a measure of propellant and chamber performance, may be determined from

$$c^* = \frac{\eta_{c^*}\sqrt{\gamma R T_f}}{\gamma\left(\frac{2}{\gamma+1}\right)^{\frac{\gamma+1}{2\gamma-2}}} \tag{2.1}$$

Here, η_{c^*} is an efficiency factor to allow for combustion inefficiencies. This efficiency tends to be somewhat low for hybrids, typically around 0.85 to 0.90. The thrust coefficient is defined as

$$C_F \equiv \frac{F}{A_t p_c} = \gamma\sqrt{\left(\frac{2}{\gamma-1}\right)\left(\frac{2}{\gamma+1}\right)^{\frac{\gamma+1}{\gamma-1}}\left(1-\left(\frac{p_e}{p_c}\right)^{\frac{\gamma-1}{\gamma}}\right)} + \frac{A_e}{A_t p_c}\left(p_e - p_a\right) \tag{2.2}$$

Assuming isentropic flow through the nozzle, the nozzle exit Mach number (Ma_e) and nozzle area expansion ratio (ε) may also be determined from

$$\mathrm{Ma_e} = \sqrt{\left(\frac{2}{\gamma-1}\right)\left(\left(\frac{p_e}{p_c}\right)^{\frac{1-\gamma}{\gamma}} - 1\right)} \tag{2.3}$$

$$\varepsilon = \frac{1}{\mathrm{Ma_e}}\left(\left(\frac{2}{\gamma+1}\right)\left(1+\left(\frac{\gamma-1}{2}\right)\mathrm{Ma_e}^2\right)\right)^{\frac{\gamma+1}{2\gamma-2}} \tag{2.4}$$

Specific impulse may then be calculated:

$$I_{sp} = \frac{\lambda C_F c^*}{g} \tag{2.5}$$

where g is the gravitational acceleration and the nozzle efficiency term (λ) is defined as

$$\lambda = \frac{\text{actual thrust}}{\text{ideal thrust}} = \frac{1}{2}\left(1 + \cos\theta_{cn}\right) \tag{2.6}$$

for an ideal conical nozzle, where θ_{cn} is the effective nozzle expansion cone half-angle.

By varying the exit pressure and employing the above equations, curves of Ma_e, ε, C_F and I_{sp} may be generated:

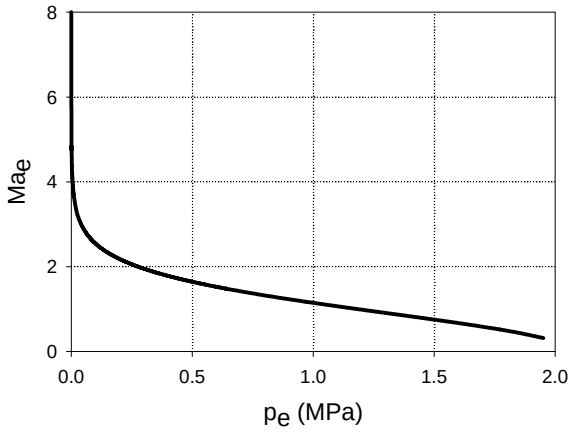

Figure 2.4: Ma_e vs. p_e

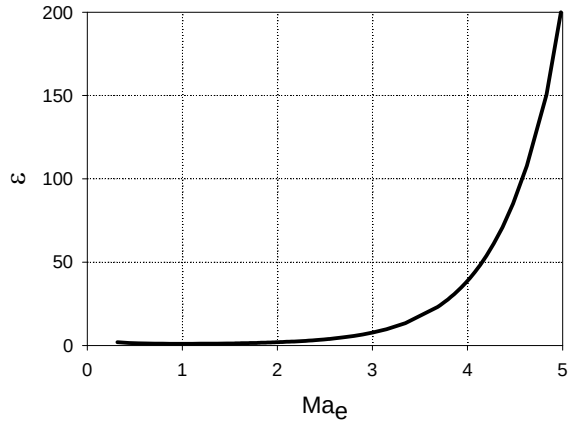

Figure 2.5: ε vs. Ma_e

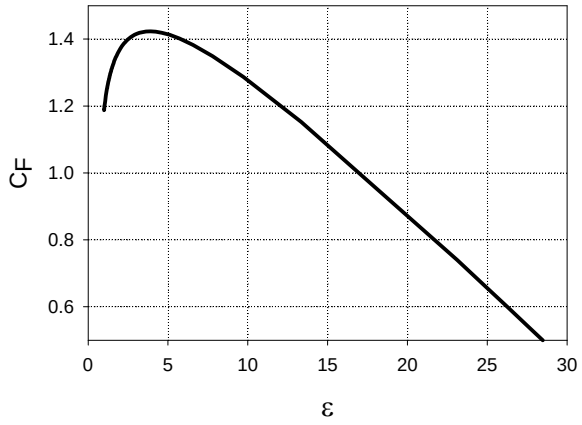

Figure 2.6: C_F vs. ε

From these plots, the maximum value of C_F, and thus I_{sp} (occurring when the exit pressure equals ambient pressure), and the corresponding values of ε and Ma_e, can be determined.

Knowing I_{sp} and choosing a target thrust level of 100 N, total propellant mass flow rate is determined from

$$\dot{m} = \frac{F}{I_{sp} g} \tag{2.7}$$

The corresponding oxidizer and fuel flow rates are determined given the design *O/F*.

As the engine is intended for static firings, the nozzle was designed for optimal expansion at ground level, with the expansion ratio as determined by Eq. (2.4). The nozzle throat area was then calculated from

$$A_t = \frac{\dot{m} c^*}{p_c} \tag{2.8}$$

Knowing A_t and ε, the nozzle exit area can then be calculated from the definition of ε.

2.5 Summary of Preliminary Engine Design

Having made the basic design choices, and using a simple preliminary regression rate model (further discussion in Section 2.6.2) and some initial assumptions about nozzle configuration (further discussion in Section 2.9), the preliminary design process yielded the following parameters (based on a GOX/paraffin propellant combination):

Table 2.2 Hybrid Rocket Engine Design Parameters (GOX/Paraffin)

Chamber I.D.:	2.152 in. (5.47 cm)
Chamber pressure:	2.1 MPa (300 psi)
Expansion Ratio:	3.9
Stoichiometric O/F:	2.5
Stoichiometric Flame Temperature:	3502 K
Initial Thrust target:	100 N
Initial Design O/F:	1.8
Design Flame Temperature:	2895 K
Isp:	209 s
Mass flowrate (total):	0.0487 kg/s
Oxidizer flowrate:	0.031 kg/s
Nozzle Contour	
Throat diameter:	6.68 mm
Exit diameter:	13.2 mm
Half-angle	
Convergent:	60^0

Exit:	15^0
Throat curvature:	5 mm
Length	
Convergent:	16.7 mm
Exit:	12.8 mm
Total:	29.5 mm
Fuel Grain	
Initial oxidizer flux:	110 kg/m^2s
Grain OD:	2.152 in. (5.47 cm)
Initial Port Diameter:	0.75 in. (1.9 cm)
Grain length:	7 in. (17.78 cm)
Max. burn duration:	18.5 s

3. Internal Ballistic Model and Simulation

3.1 Classical Regression Rate Model

While HREs incorporate certain elements of both solid- and liquid-propellant rocket engines, their internal ballistics are very different from either, owing to the turbulent diffusion flame combustion process they exhibit. Work by Muzzy (1963) produced Schlieren photographs that physically visualized the boundary layer, and guided work by Marxman *et al* (1964) in the development of a hybrid rocket combustion model[2].

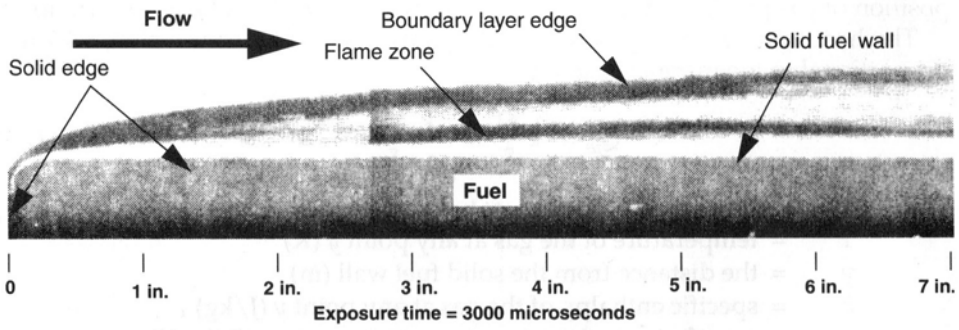

Figure 3.1a: HRE boundary layer Schlieren photograph[1]

The key feature of this model, as confirmed by the Schlieren photographs, is a turbulent boundary layer with a flame zone established within the boundary layer, standing off from the fuel surface. Fuel enters the flame zone due to vaporization from the fuel grain surface, while oxidizer diffuses in from the port free-stream flow, and the flame zone occurs in the region in the boundary layer where the resulting mixture ratio of oxidizer to fuel (O/F ratio) is roughly stoichiometric. A visual summary of the model is illustrated in Figure 3.1b.

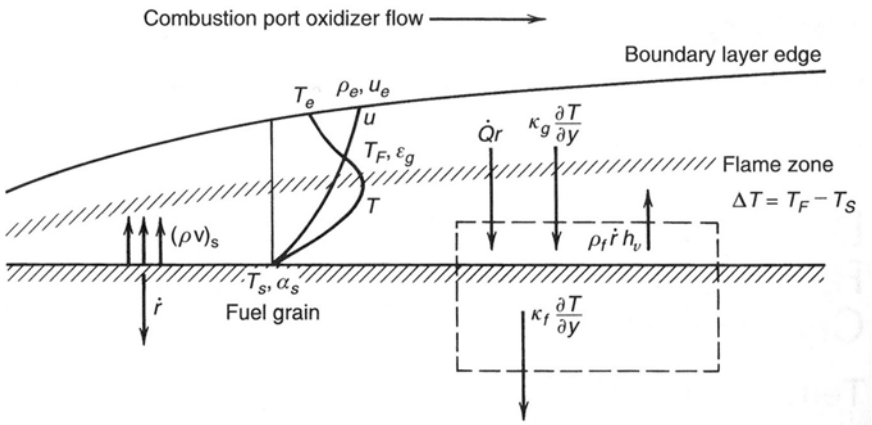

Figure 3.1b: HRE combustion model[3]

Assuming steady state operation and neglecting radiation ($\dot{Q}_r$) and conduction within the fuel mass ($k_f \frac{\partial T}{\partial y}$), the convective heat transfer from the flame zone to the fuel surface results in gasification of the fuel according to:

$$\dot{Q}_c = \rho_f r_b h_v \tag{3.1}$$

where the h_v, term represents the heat required to decompose the solid fuel at its initial temperature into vapors and other fragments that can enter the flame zone. Typically it incorporates the heat of vaporization, the heat to warm the solid to the fuel grain surface temperature, and any depolymerization or other thermal changes prior to gasification. Further, the heat transferred through the boundary layer to the fuel grain surface occurs by conduction:

$$\dot{Q}_s = k_g \left.\frac{\partial T}{\partial y}\right|_{y=0} \tag{3.2}$$

Using the definition of the Stanton number

$$C_H = \frac{h}{\rho_e u_e C_p} \tag{3.3}$$

and the fact that the heat flux at the fuel surface is given by

$$\dot{Q}_s = h(T_f - T_s) \tag{3.4}$$

the heat flux rate can be expressed in terms of the Stanton number as

$$\dot{Q}_s = C_H \rho_e u_e \Delta h \tag{3.5}$$

where ρ_e and u_e are the density and velocity at the edge of the boundary layer, and Δh is the change in enthalpy between the flame zone and fuel surface. In addition, the heat transfer coefficient at the fuel surface can be related to the skin friction coefficient via the modified Reynolds' analogy:

$$C_H = \frac{C_f}{2} \mathrm{Pr}^{-2/3} \tag{3.6}$$

where C_f is the skin friction coefficient including blowing. Combining Eqs. (3.1), (3.5), and (3.6), the fuel regression rate may be expressed as

$$r_b = \frac{C_f}{2} \frac{\Delta h}{h_v} \frac{\rho_e u_e}{\rho_f} Pr^{-2/3} \tag{3.7}$$

Experiments investigating the effect of blowing on the skin friction coefficient[3] have related C_f to the skin friction coefficient without blowing (C_{fo}) according to

$$\frac{C_f}{C_{f_0}} = 1.27\beta^{-0.77} \quad (5 \le \beta \le 100) \tag{3.8}$$

where the blowing coefficient β is defined as

$$\beta = \frac{(\rho v)_s}{\rho_e u_e C_f / 2} \tag{3.9}$$

Here, v is the gas velocity normal to the fuel surface. Thus the quantity $(\rho v)_s$ represents the mass flow rate leaving the fuel surface. C_{fo} is in turn related to the local Reynolds number by the relation

$$\frac{C_{f_0}}{2} = 0.0296\,\mathrm{Re}_x^{-0.2} \quad (5\text{x}10^5 \le \mathrm{Re}_x \le 1\text{x}10^7) \tag{3.10}$$

Noting additionally that $\rho_e u_e$ is the definition of the port mass flux G, and that in a turbulent boundary layer Pr is very nearly equal to 1, Eq. (3.8) can be rewritten as

$$r_b = 0.036 \frac{G^{0.8}}{\rho_f} \left(\frac{\mu}{x} \right)^{0.2} \beta^{0.23} \tag{3.11}$$

where μ is the combustion gas viscosity and x is the axial location down the fuel port. It should be noted that the constant of 0.036 applies only when British engineering units are used. Eq. (3.11) has been shown to provide a reasonably good estimate of the regression rate from theory, but for greater accuracy, it is noted in practice that the general form of the equation may be expressed as

$$r_b = aG^n x^m \tag{3.12}$$

where the coefficient a incorporates the properties of the propellants and combustion products, while the exponents n and m relate to the fluid dynamics. These are typically determined experimentally, for a given propellant combination and engine geometry, through hot fire testing of the engine. The inclusion of the axial distance effect in Eq. (3.12) is related to left-to-right boundary layer growth and lower resulting turbulent shear stress.

3.2 Preliminary Design Using Empirical Model

As seen from Eq. (3.11), the fuel regression rate at a given point on the surface of a classical HRE's fuel port is a function of several parameters, although the dominant factor is the local total port flow mass flux G. This quantity varies both with distance down the length of the port, and with time over the course of the burn due to the widening of the port as the surface regresses. For preliminary design purposes however, it has been found that hybrid combustion can be reasonably modeled by considering a simplified space-averaged regression rate r_b, estimated using an expression of the form

$$r_b = aG_{ox}^n \tag{3.13}$$

where G_{ox} is the average port oxidizer flux, and a and n are empirically-determined constants. As a reasonably large body of experimental HRE regression rate data exists and has been used in conjunction with this model to determine the constants a and n for a range of propellant combinations, this model serves as a useful tool for preliminary HRE design. In the case of the paraffin / GOX combination, values of a and n of 0.488 and 0.62 respectively were chosen[20], providing r_b in mm/s when G_{ox} is given in units of g/cm^2-s. For simulation of the polyethylene / GOX propellant combination, a and n were taken to be 0.132 and 0.498 respectively[4].

From Eq. (3.13), the total fuel mass flow rate is computed from

$$\dot{m}_{fuel} = r_b \rho_{fuel} PL \tag{3.14}$$

where P is the average internal core peripheral distance, and L is the fuel grain length. In a typical firing, the O/F will vary along the length of the fuel grain, becoming increasingly fuel-rich as one moves aft due to the cumulative vaporization of fuel from

the grain surface upstream and the reduction in oxidizer as it reacts. Additionally, the point at which a given O/F ratio occurs will move aft as the central port widens. The distance down the grain at which the particular desired O/F occurs is termed the *stoichiometric length* (L_{st}). A common design-point for sizing an HRE sets the fuel grain length to equal L_{st} at the middle of the burn. From Eq. (3.14), L_{st} may be determined for a circular port as shown by

$$L_{st} \approx \frac{G_f D_{port}}{4 r_b \rho_{fuel}} \tag{3.15}$$

Two additional constraints also affect the grain design. While in principle burn duration can be increased by increasing the grain outer diameter, doing so increases the stresses in the grain and can lead to cracking. It is typically observed that for paraffin, the ratio of grain outer diameter to port diameter should be kept below about three to avoid cracking. The desired oxidizer mass flow rate also imposes a lower limit on port diameter, since too high a port mass flux will cause the flame to blow out. This limit has been observed to range typically from about 350 kg/m^2-s for liquid oxidizers, to 700 kg/m^2-s for gases[1]. These requirements, combined with the desire for a suitably long burn duration at the design thrust level and the desire for ease of manufacturing using off-the-shelf components drove the selection of a 2.5-inch (6.35-cm) nominal Schedule 80 steel pipe for the chamber, with the correspondingly sized phenolic liner dictating a grain outer diameter of 2.152 in. (54.66 mm). An initial ¾ inch (19.05 mm) port diameter was additionally selected in order to be a standard size while also being consistent with the need to keep stresses in the fuel grain suitably low. Other groups' experience with paraffin fuels has indicated that it is particularly prone to cracking or fragmenting under high stresses, so this is a particularly important requirement. In particular, it was noted[23]

that for paraffin fuel grains, the ratio of grain outer diameter to port diameter should be kept below 3 to avoid cracking.

Given the oxidizer mass flux required to achieve the target thrust level, this port geometry results in a conservative oxidizer mass flux of 109.8 kg/m^2-s for initial low thrust tests, with ample margin to run subsequent tests at higher oxidizer mass flow rates, and therefore higher thrust levels, with the same fuel grain.

Using Eq. (3.15) suggested a stoichiometric length of approximately 7 in. (17.78 cm) for the paraffin grain. While the basic design of the HRE was set based on a paraffin fuel grain, the desire to also test with polyethylene required a much longer chamber owing to the much lower regression rate. Using polyethylene, Eq. (3.15) dictates a stoichiometric grain length of approximately 25 inches. The engine's combustion chamber was accordingly designed to accommodate a grain of up to 25 inches length, assuming no pre- or post-combustion chamber.

3.3 Ryerson University QSHYB Model

As an alternative internal ballistics model, previous work at Ryerson University on the modeling of erosive burning in solid rocket motors was extended by Greatrix[7,8] and is being considered for its applicability to HREs. Neglecting any pressure-based burning rate component (such as from the addition of an oxidizer to the hybrid fuel grain), this model expresses the regression rate as

$$r_b = \frac{h^*}{\rho_s C_p} ln\left(1 + \frac{C_p}{C_s} \frac{(T_f - T_s)}{(T_s - T_i - \Delta H_s / C_s)}\right) \tag{3.16}$$

where h^* is the convective heat transfer coefficient without blowing and can be expressed via Reynolds' analogy as

$$h^* = \frac{k^{2/3} C_p^{1/3}}{\mu^{2/3}} \frac{G f^*}{8} \tag{3.17}$$

Here, f^* is the Darcy-Weisbach friction factor (again, without blowing). The semi-empirical expression developed by Colebrook[24] has been shown to be accurate over a wide range of Reynolds numbers:

$$(f^*)^{-1/2} = -2\log_{10}\left(\frac{2.51}{\mathrm{Re}_d (f^*)^{1/2}} + \frac{\varepsilon/d}{3.7}\right) \tag{3.18}$$

Here, d denotes the hydraulic diameter of the fuel port, and ε is the effective burning surface roughness height.

3.4 QSHYB Simulation

Having arrived at a preliminary engine design, the internal ballistic simulation program QSHYB can then be employed to simulate the firing of the engine, and refine the engine's design where indicated. This Ryerson-developed HRE internal ballistic model is intended to provide greater accuracy in modeling the firing than that provided by the simpler expressions used for preliminary design (e.g., Eq. (3.13)), and will ultimately be improved with the aid of experimental data obtained from hot-fire testing. As the code requires several inputs pertaining to the combustion gas properties in the flame zone (flame temperature, molecular weight, γ, C_p, viscosity and conductivity), NASA's CEA code was employed to determine these properties for a stoichiometric mixture of fuel and

GOX, which is expected to correspond to the conditions in the boundary layer flame zone.

The QSHYB simulation run can be continued until the solid fuel grain is nearly consumed. Figure 3.2a shows the resulting sea-level thrust curve for the GOX/paraffin fuel combination with 7 inch grain length, while Figure 3.2b shows the regression rate behaviour at the mid-grain position over the course of the engine's firing.

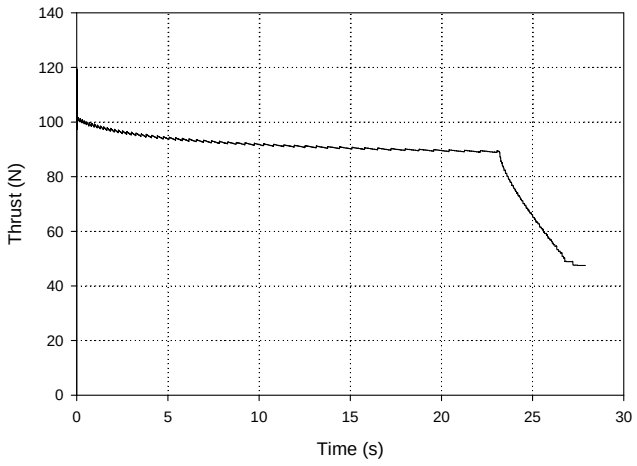

Figure 3.2a: QSHYB predicted sea-level thrust curve, GOX/paraffin engine

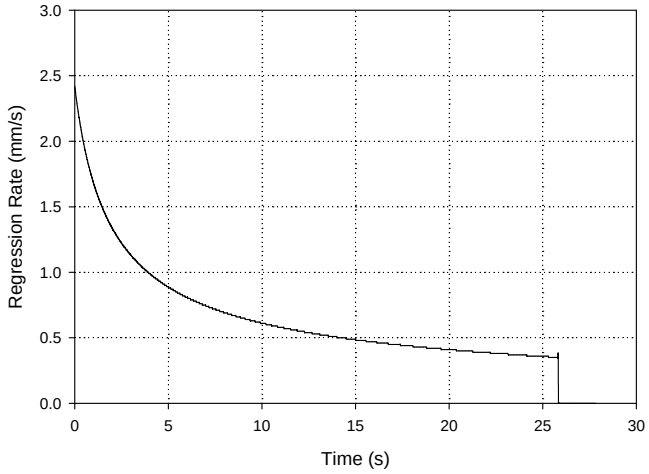

Figure 3.2b: QSHYB predicted regression rate history at mid-grain, GOX/paraffin engine

Grain burnthrough (engine internal casing liner being reached) is predicted to begin at about the 23 second mark, with a steep thrust tailoff until practically all the fuel is consumed. The performance as predicted by the QSHYB code is in good agreement with the preliminary design, although it predicts a slightly longer burn duration, and slightly lower regression rate, than did the preliminary calculations. The predicted thrust curve is as expected for a 100-N thrust engine, and the predicted regression rates are also in line with those reported in the literature for HREs burning paraffin and GOX[20].

An additional QSHYB simulation was conducted for the polyethylene grain, with polyethylene modeled in NASA's CEA code as $(CH_2)_x$ (cr). The fuel grain used for this run was 24 inches in length to provide a more optimal length for the slower-regressing polyethylene, and all other parameters related to grain and nozzle geometry were the same as for the paraffin grain. The same oxidizer flow rate was also used. The resulting

thrust curve is shown in Figure 3.3a, and the regression rate profile is shown in Figure 3.3b.

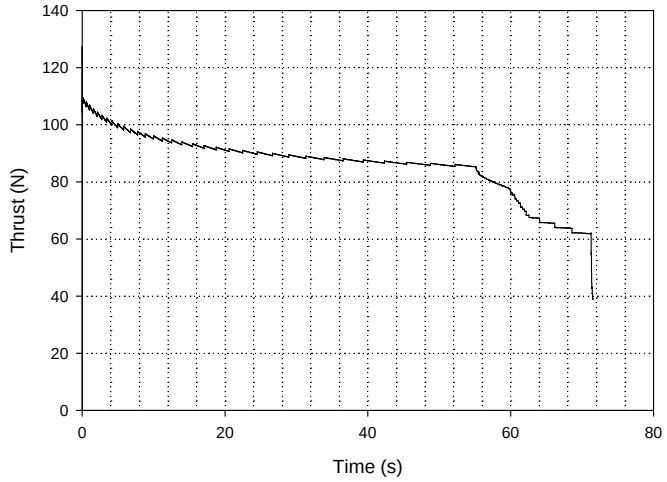

Figure 3.3a: QSHYB predicted sea-level thrust curve, GOX/PE engine

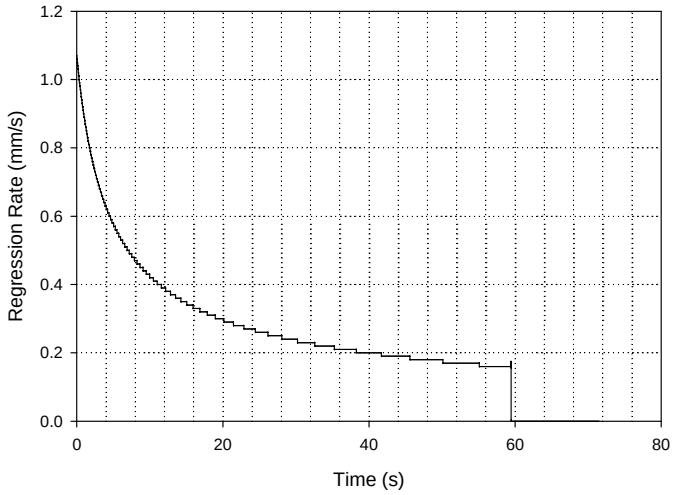

Figure 3.3b: QSHYB predicted regression rate history at mid-grain, GOX/PE engine

For this run, the grain burnthrough begins about 55 seconds, with the stoichiometric length equaling the grain length at about 60 seconds. The thrust tailoff with the

polyethylene grain occurs more gradually than with the paraffin grain, owing to the lower average regression rate.

4. System Components

4.1 Combustion Chamber

4.1.1 Chamber

For fabrication of the physical engine structure, commercially-available heavy-walled carbon steel DOM (drawn-over-mandrel) tubing was selected. Carbon steel was selected for its combination of high strength, low cost, and ready availability. As this engine was intended for use as a robust testbed for static firings and must be strong enough to withstand both current and future test requirements, some of which may well involve running at higher chamber pressures, it was decided to ensure that the chamber walls were sufficiently thick to provide a large safety factor for any foreseeable operating pressure. The chamber tubing was supplied by CPI Automation Inc, and basic chamber dimensions are as follows:

OD: 3.000 in = 76.20 mm

ID: 2.250 in = 57.15 mm

Wall: 0.375 in = 9.525 mm

Length: 27.188 in = 690.575 mm

As discussed in Section 3.2, the length of the chamber was chosen based on the stoichiometric length of the longest (polyethylene) grain to be fired. For the paraffin fuel grain, or for shorter polyethylene grains, this length also allows space for a pre-

combustion chamber at the head end and a post-combustion chamber at the aft end to promote better mixing and combustion of any unburned fuel still resident in the core flow. The actual length of these chambers will vary in the planned experimental test series, so the overall chamber was sized to be of sufficient length for the largest planned chamber sizes.

The combustion chamber is illustrated in Figure 4.1:

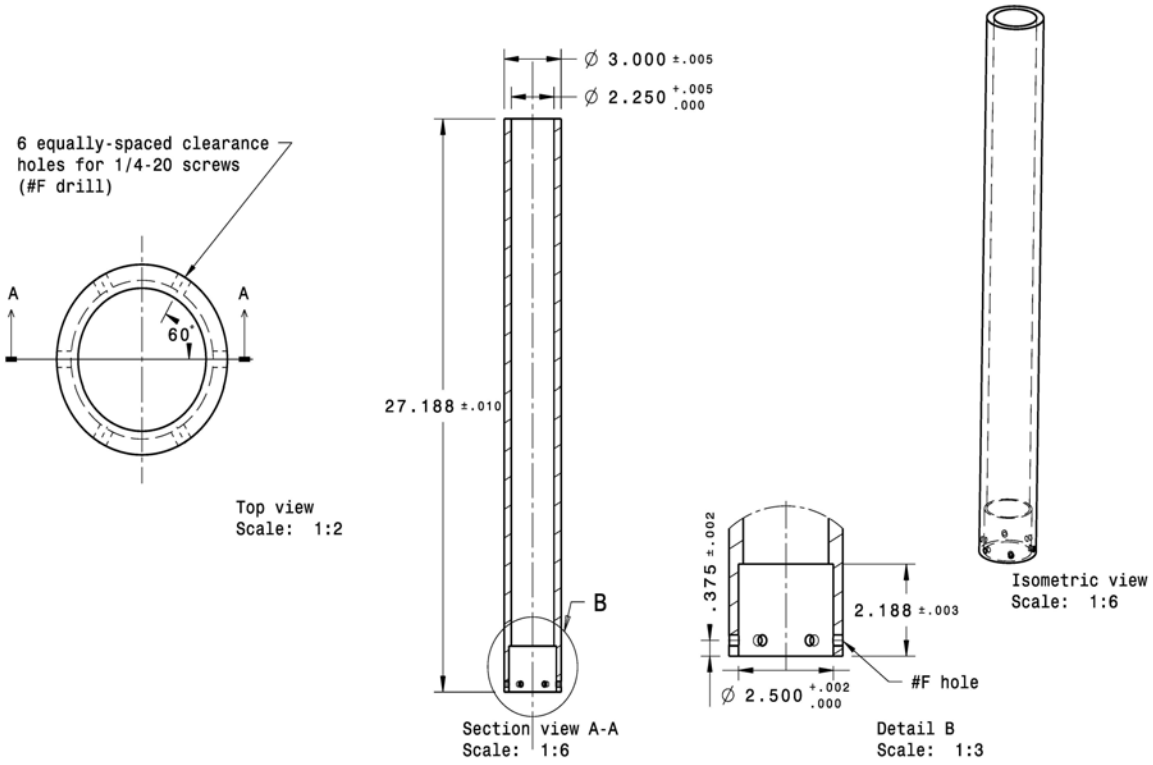

Figure 4.1: Combustion Chamber (dimensions in inches)

Performing a hoop stress analysis assuming a yield stress of 353.4 MPa (typical of AISI 10XX carbon steels) and allowing a maximum operating pressure 50% higher than the design chamber pressure results shown below:

$$p_{yield} = \frac{t_w \sigma_{yield}}{r} = \frac{(0.0095\ \text{m})(353.4 \times 10^6\ \text{Pa})}{0.02858\ \text{m}} = 117.47\ \text{MPa} = 17\,038\ \text{psi},$$

$$\text{Assume MEOP} = 1.5 \text{ x } p_c = 450\ \text{psi},$$

$$\text{Factor of Safety} = \frac{17038}{450} = 37.9$$

For a laboratory (therefore non-flyable) engine where high mass is not a problem, this allows a very high degree of safety, effectively eliminating the possibility of a burst thrust chamber.

A standard 2.5 inch 900# orifice weld neck flange was machined to fit over the head end of the chamber tubing and welded in place. This allows for the oxidizer injector section to be easily replaced as future research requirements might dictate. The aft end was machined to allow a standard nozzle blank to be inserted and sealed with a pair of O-rings. A retaining ring was bolted in place to secure the nozzle, and to allow it to be replaced if damage occurs or future research goals require such a change. The flange is illustrated in Figure 4.2, the aft retaining ring in Figure 4.3, and the complete chamber assembly with nozzle in place is shown in Figure 4.4.

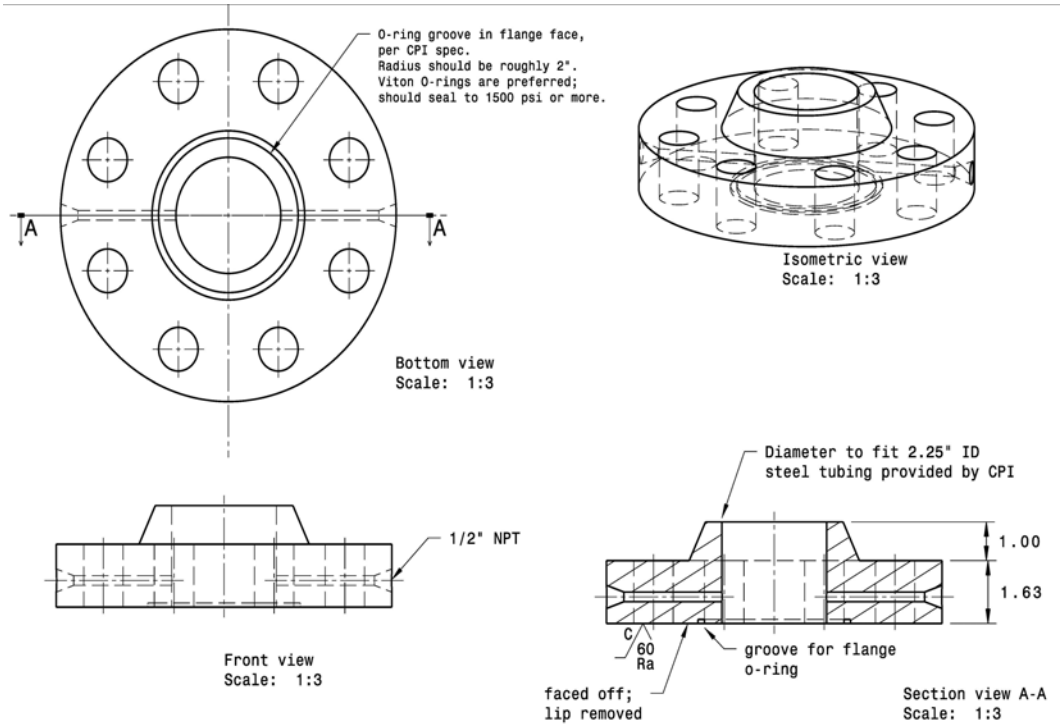

Figure 4.2: Flange drawing

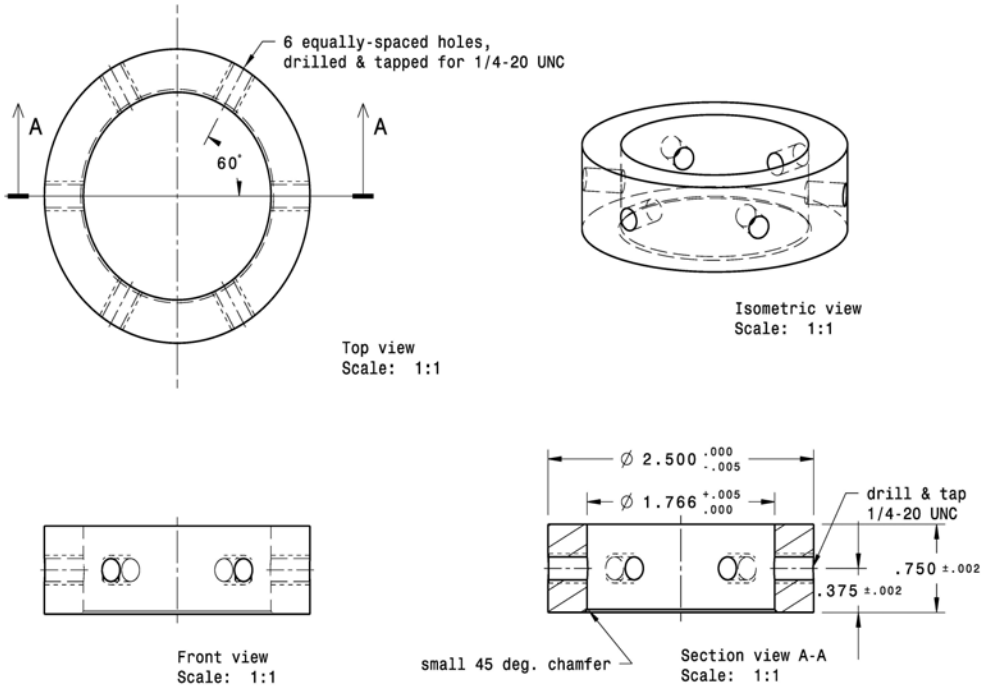

Figure 4.3: Nozzle retaining ring drawing

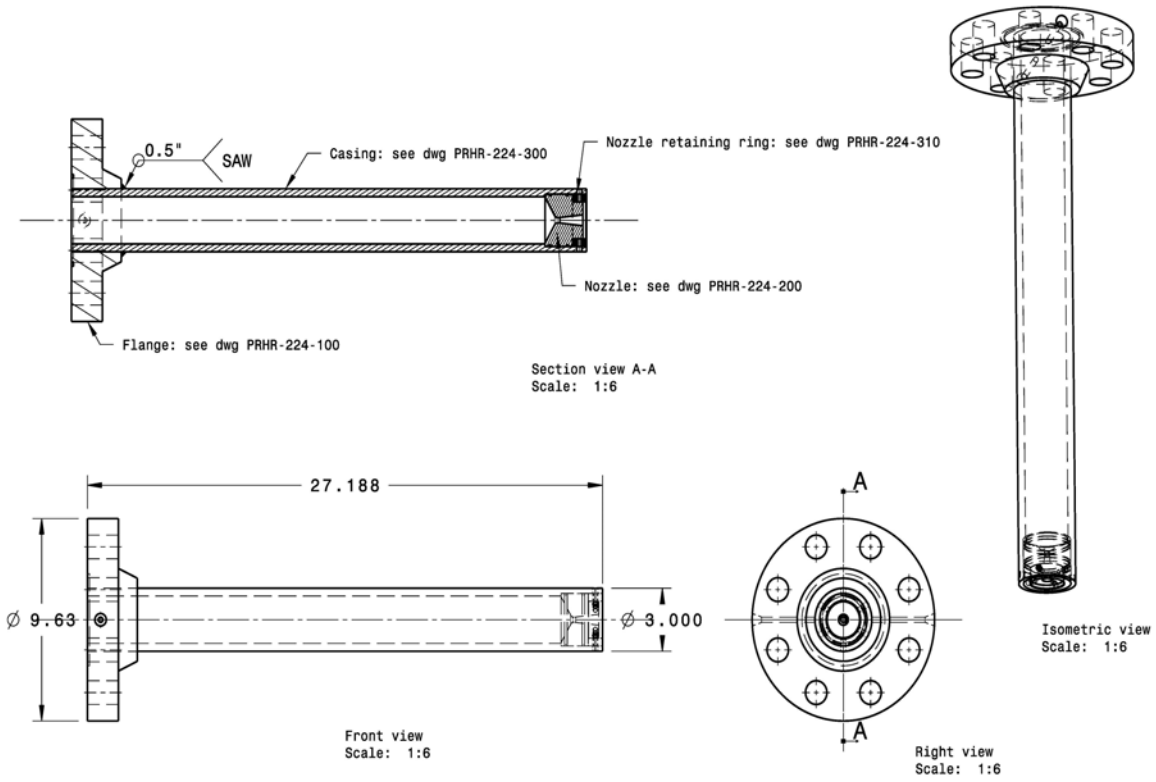

Figure 4.4: Complete chamber assembly drawing

The completed combustion chamber components are shown in Figure 4.5a (complete chamber), Figure 4.5b (head end flange) and Figure 4.5c (aft end, with nozzle retaining ring removed).

Figure 4.5a: Complete combustion chamber assembly

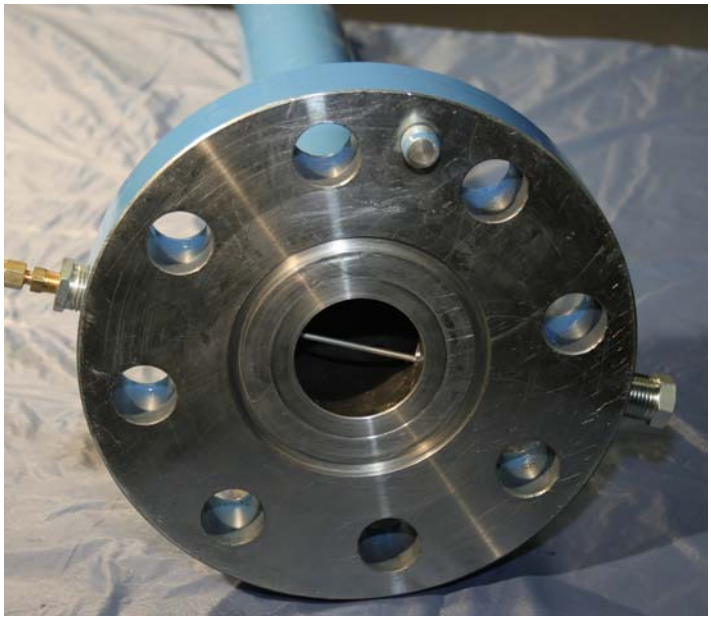

Figure 4.5b: Chamber head end flange

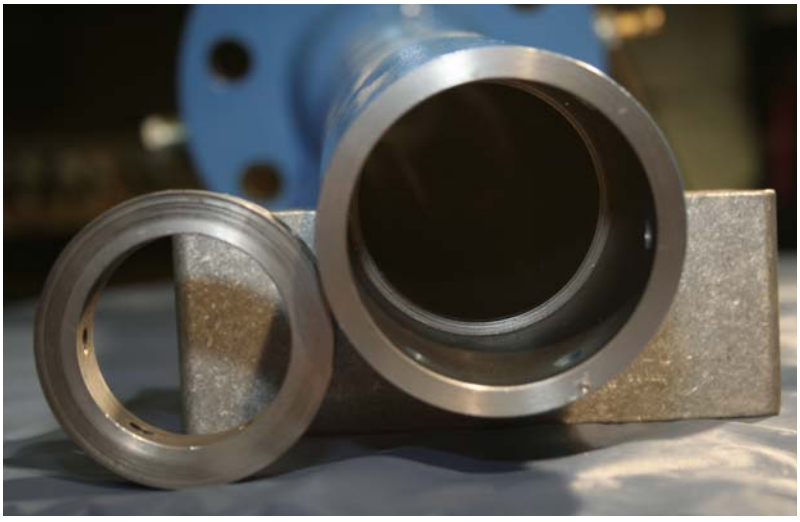

Figure 4.5c: Chamber aft end and nozzle retaining ring

4.1.2 Chamber Liner

Due to the high temperatures in the combustion chamber (well above the melting point of steel), it was necessary to provide sufficient insulation or cooling to prevent the inner wall of the chamber from becoming excessively hot. To achieve this, a length of Type XX paper-phenolic tubing was selected as an ablative liner. The tubing is an off-the-shelf item and has the following dimensions:

OD: 2.250 in = 57.15 mm

ID: 2.00 in = 50.8 mm

Wall: 0.125 in = 3.18 mm

Length: 25 in (note: supplied in 40-in. lengths) = 63.5 cm

This tubing serves two functions. It provides a convenient, replaceable cartridge to cast the fuel grain into, and also shields any exposed steel walls of the pre- and post-combustion chambers from hot gases. Since these regions do not have the benefit of being effectively insulated by the fuel grain, providing adequate insulation in these areas is especially critical.

Phenolic composites of various types have been commonly used as ablative liners in rocket applications. Paper-phenolics are the least expensive, though they do tend to erode at a higher rate than other types. The actual erosion rate depends greatly on the actual conditions in the chamber, including heat flux, local gas properties and composition, and flow, so testing is required to accurately characterize it. It is expected

that initial short-duration firings will confirm that the current liner will be suitable for all planned burn durations, but if it experiences higher than expected erosion in the pre- and/or post-combustion chambers, it will be replaced with a more resistant liner.

4.2 Feed System

4.2.1 Overall Design

The primary function of the prototype engine's feed system is to supply gaseous oxygen (GOX) to the injector at the design pressure and flowrate. Since accurate measurement of the oxidizer flowrate is an essential component of internal ballistics modeling and overall system performance calculations, the feed system also incorporates a means of flowrate measurement. Its secondary function is to supply compressed nitrogen to purge the system at the end of a firing and allow for the rapid extinguishing of the fuel grain on command, both for safety and to ensure that the fuel grain's end-of-firing condition and geometry are not distorted due to additional burning, smoldering, or heat soak-back. As a tertiary function, the feed system also supplies a low flow of GOX for smooth ignition of the engine. An additional low flowrate propane feed is available for future upgrades to provide a spark-initiated torch ignition capability.

Due to the relatively high pressures involved, the feed system design also has a considerable impact on the overall safety. Accordingly, it was decided to incorporate features including check valves to prevent backflow, a rupture disk near the engine injector to prevent overpressure, and a choking orifice to decouple the feed system from the combustion chamber.

The basic configuration of the feed system is illustrated schematically in Figure 4.6a:

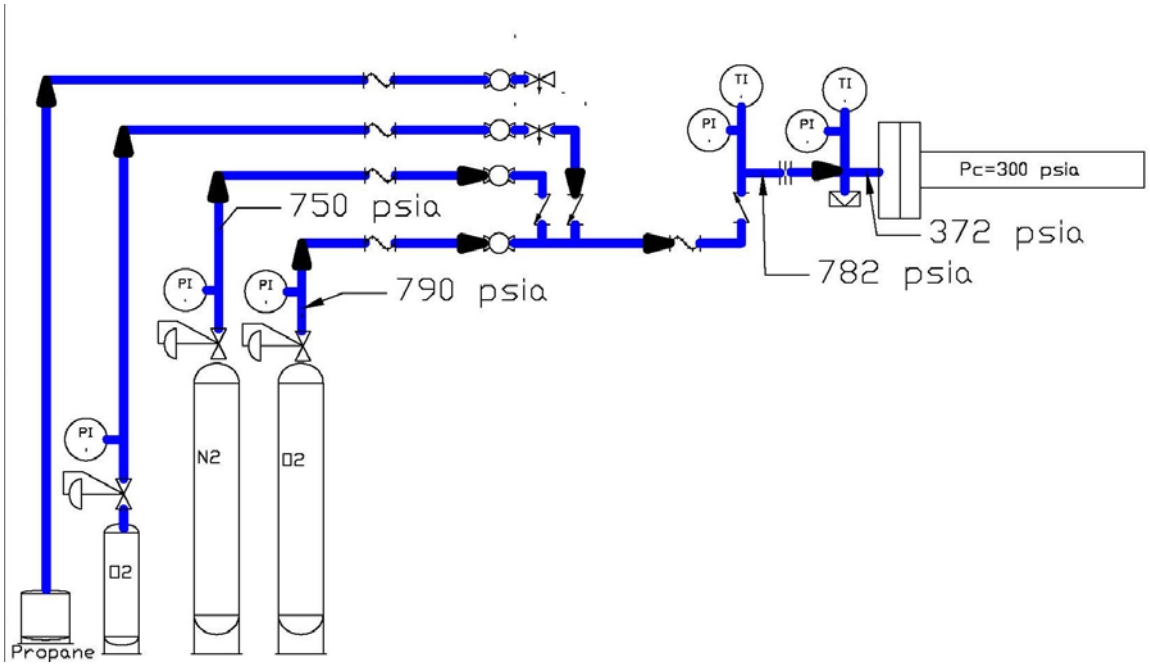

Figure 4.6a: Feed system schematic diagram

4.2.2 Subsystems

In its physical implementation, the feed system consists of three major subsystems: a set of rigid plumbing mounted to the head end of the engine, a feed distribution panel incorporating the actuated GOX, N_2 and ignition valves, and the GOX, N_2 and ignition supply tanks. The three subsystems are connected via lengths of stainless braided Teflon flex hose with industrial 37° flare (JIC – Joint Industrial Council standard) tube fittings. All feed system components are cleaned and degreased to a high level in accordance with

standard guidelines for the cleanliness of high pressure oxygen systems. The physical layout of the feed system is illustrated in Figure 4.6b:

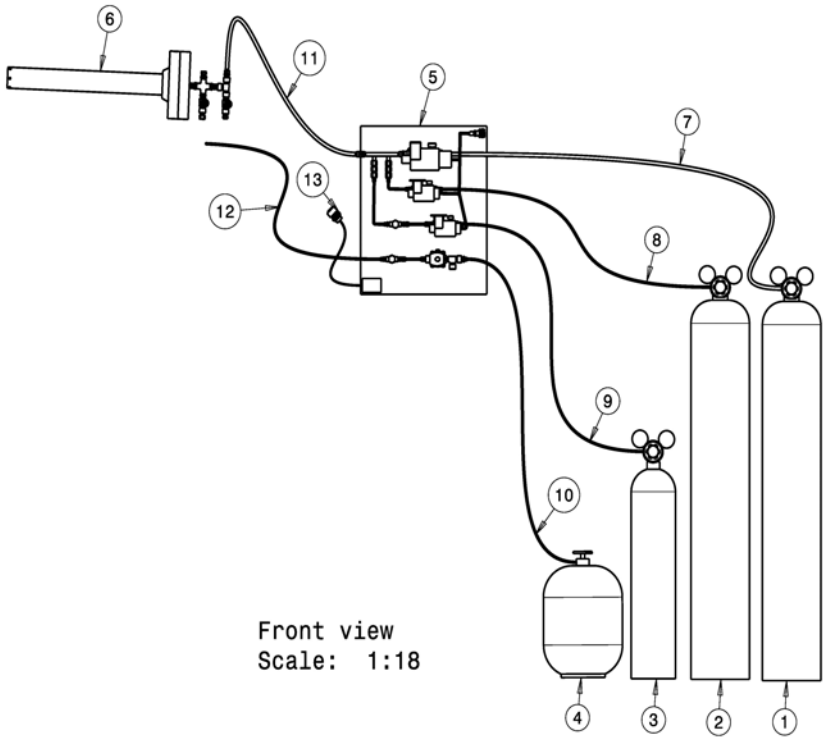

	Name	Description
1	Oxygen supply cylinder	Std. T cylinder, with Tescom high-flow regulator to 1/2" JIC male fitting
2	Nitrogen supply cylinder	Std. T cylinder with regulator, to 1/4" JIC male fitting
3	Ignition oxygen supply cylinder	Small oxygen cylinder with regulator, to 1/4" JIC male fitting
4	Ignition propane supply cylinder	20# propane LPG cylinder with regulator, to 1/4" JIC male fitting
5	Fluid distribution panel	See dwg. PRHR-224-810
6	Engine	
7	Main O2 supply hose	stainless steel braded teflon hose, 2500 psi rating, -8AN (1/2" JIC) x 10 ft
8	N2 supply hose	Stainless steel braided teflon hose, 2500 psi rating, -4AN (1/4" JIC) x 10 ft
9	Ignition O2 supply hose	Stainless steel braided teflon hose, 2500 psi rating, -4AN (1/4" JIC) x 10 ft
10	Ignition propane supply hose	Stainless steel braided teflon hose, 2500 psi rating, -4AN (1/4" JIC) x 10 ft
11	main oxidizer line	Stainless steel braided teflon hose, 2500 psi rating, -8AN (1/2" JIC) x 8 ft
12	Ignition propane to engine	(currently unused)
13	Valve control cable	Male 24-pin Amphenol cannon-type connector, to fluid distribution panel

Figure 4.6b: Feed System Layout

4.2.2.1 Engine Head End Plumbing

The engine head end plumbing attaches directly to the injector flange via a 3/8" NPT (National Pipe Tapered) fitting, and to the high pressure hose from the feed distribution panel. This is illustrated in Figure 4.7:

Figure 4.7: Head end plumbing and instrumentation

In spite of the relatively low oxidizer flowrates involved in the initial configuration of this system, it was decided to size the feed system plumbing to be conservatively large in order to ensure a minimal pressure drop in the feed system due to viscous flow losses, while also providing ample margin for future tests at higher flowrates. Accordingly, 3/8" NPT pipe fittings were used for the head end plumbing, with ½" JIC tube fittings on the main flex hose line.

A choking orifice was included to fix the GOX flowrate at the 0.0307 kg/s specified during preliminary design, and to insure that this flowrate remains constant in spite of any downstream pressure fluctuations in the engine itself. The feed pressures were sized conservatively based on an injector inlet pressure (choking orifice downstream pressure) 25% greater than the chamber pressure to provide greater combustion stability, and an

orifice inlet pressure at least double this to ensure that the orifice remains choked throughout operation. This suggested a feed pressure of at least 750 psia (5.17 MPa). Assuming isentropic flow, the mass flow rate through a choked orifice of area *A* may be determined from

$$\dot{m} = Ap_1\sqrt{\frac{\gamma}{RT_1}\left(\frac{2}{\gamma+1}\right)^{\frac{\gamma+1}{\gamma-1}}} \tag{4.1}$$

where all flow properties are specified upstream of the orifice, and p_1 and T_1 are the stagnation pressure and temperature respectively. In practice, this is usually modified to account for flow losses through the use of a discharge coefficient, *C*:

$$\dot{m} = CAp_1\sqrt{\frac{\gamma}{RT_1}\left(\frac{2}{\gamma+1}\right)^{\frac{\gamma+1}{\gamma-1}}} \tag{4.2}$$

C is primarily a function of the physical characteristics of the orifice and is determined experimentally. The orifice used in the present work was supplied by O'Keefe Controls, Inc., who additionally supplied flow rate data for their orifices. This data suggested a *C* value of approximately 0.77. Using Eq. (4.2) and suitable values of γ and *R* for gaseous oxygen allowed for the determination of the required orifice diameter to provide the design GOX flow rate at a range of feed pressures.

Table 4.1 Choking Orifice Sizes

P_1 (psia):	P_1 (Pa):	Area (m^2)	diameter (mm)	diameter (in)
750	5171068	3.05336E-6	1.97	0.0776
760	5240015	3.01319E-6	1.96	0.0771
770	5308963	2.97405E-6	1.95	0.0766
780	5377910	2.93592E-6	1.93	0.0761
790	5446858	2.89876E-6	1.92	0.0756
800	5515806	2.86253E-6	1.91	0.0752

Choosing the closest standard orifice size resulted in the selection of a 0.076 in. (1.93 mm) diameter stainless steel orifice, with an upstream (feed) pressure of 782 psi (5.388 MPa). To determine the actual mass flowrate during operation, it is necessary to measure both pressure and temperature immediately upstream of the orifice, so a pressure transducer and thermocouple are incorporated into the plumbing for this purpose.

A rupture disk is provided downstream of the orifice in order to allow for any unforeseen excessive pressure spikes in the chamber. The disk is designed to fail at 1000 psi (6.89 MPa) and vent any excess pressure.

4.2.2.2 Feed Distribution Panel

To provide a modular, easy-to-use setup, it was decided to incorporate the main GOX valve, the N_2 purge valve, the ignition GOX and propane solenoids, and their associated plumbing into a single panel. A drawing of this panel is shown in Figure 4.8a, and a photograph of the completed unit is shown in Figure 4.8b:

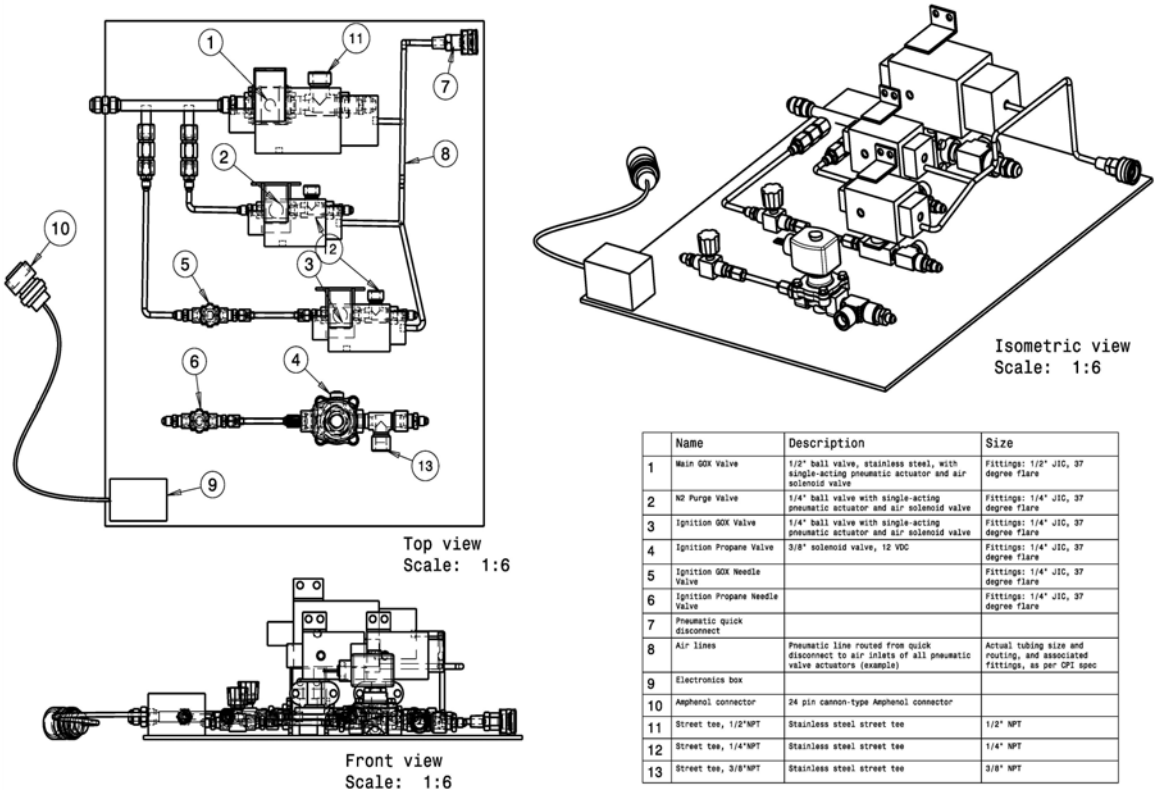

	Name	Description	Size
1	Main GOX Valve	1/2" ball valve, stainless steel, with single-acting pneumatic actuator and air solenoid valve	Fittings: 1/2" JIC, 37 degree flare
2	N2 Purge Valve	1/4" ball valve with single-acting pneumatic actuator and air solenoid valve	Fittings: 1/4" JIC, 37 degree flare
3	Ignition GOX Valve	1/4" ball valve with single-acting pneumatic actuator and air solenoid valve	Fittings: 1/4" JIC, 37 degree flare
4	Ignition Propane Valve	3/8" solenoid valve, 12 VDC	Fittings: 1/4" JIC, 37 degree flare
5	Ignition GOX Needle Valve		Fittings: 1/4" JIC, 37 degree flare
6	Ignition Propane Needle Valve		Fittings: 1/4" JIC, 37 degree flare
7	Pneumatic quick disconnect		
8	Air lines	Pneumatic line routed from quick disconnect to air inlets of all pneumatic valve actuators (example)	Actual tubing size and routing, and associated fittings, as per CPI spec
9	Electronics box		
10	Amphenol connector	24 pin cannon-type Amphenol connector	
11	Street tee, 1/2"NPT	Stainless steel street tee	1/2" NPT
12	Street tee, 1/4"NPT	Stainless steel street tee	1/4" NPT
13	Street tee, 3/8"NPT	Stainless steel street tee	3/8" NPT

Figure 4.8a: Feed distribution panel, drawing

Figure 4.8b: Feed distribution panel, as manufactured

The main GOX valve is a stainless steel ½" NPT, 3-piece ball valve with Teflon seats to ensure oxygen compatibility. A single-acting (spring return) pneumatic actuator allows remote actuation of the valve, and ensures that the valve will fail closed in case of any loss of power or pneumatic pressure.

The N_2 purge line and ignition GOX line join the main GOX line to the engine immediately downstream of the GOX valve and are both isolated with stainless steel check valves to prevent backflow.

The N_2 purge valve and ignition GOX valve are both pneumatically-actuated ball valves similar to the main GOX valve but smaller (1/4" NPT) due to their comparatively low flowrates.

The ignition propane valve is a 3/8" NPT solenoid valve with 12 VDC coil. Each ignition valve has a hand-operated needle valve immediately downstream to allow for adjustment of the ignition oxygen and propane flowrates.

The feed distribution panel additionally features a pneumatic quick disconnect fitting to connect pilot air to the three pneumatic actuators, and a 24-pin MIL-spec cannon connector to provide electrical control signals to the valves.

4.2.2.3 Regulated Supply Cylinders

Three compressed gas cylinders are required for engine operation. These include a large (T-size) GOX cylinder, an N_2 cylinder, and a small GOX cylinder for ignition oxygen. For later igniter designs, a propane cylinder will also be employed. Each cylinder has a reducing pressure regulator mounted directly to it, with a male 37° flare JIC fitting immediately downstream to connect it to the feed distribution panel. The most critical regulator is that on the main GOX line, as this must allow relatively high flowrates. A Tescom 44-1300 Series high-flow, hand loaded regulator with ¾" NPT ports and a 3/8" main valve with a flow coefficient (Cv) of 2.0 was selected for this purpose. For oxygen compatibility, the regulator trim is stainless steel, with CTFE valve seat & gaskets, Viton-A O-rings and Teflon backup rings.

4.2.2.4 Interconnecting Hose

Stainless steel braided Teflon flex hose with 37° flare JIC fittings were used for all interconnecting lines due to their oxygen compatibility. The main GOX line from the feed distribution panel to the engine and the line from the main GOX supply cylinder to the feed distribution panel are ½ inch diameter, while all other lines are ¼ inch diameter.

4.3 Engine Test Stand Hardware

4.3.1 Test Stand

The primary function of the test stand is to provide a strong, portable platform to secure the engine during test firings, and to enable a very small amount of travel of the engine with a minimum of friction to allow it to compress a load cell for thrust measurement. Accordingly, the base of the stand is fabricated from a steel platform, fabricated from I-beams, mounted on wheels for transportation and secured to anchor points on the ground during actual firings.

To the base is bolted a linear bearing slide, standing off from the base by a structure fabricated from aluminum plate. The engine mounting fixture is bolted to the bed of the bearing slide, and secures the engine using a pair of aluminum industrial pipe clamps. Figure 4.9 illustrates the test stand, Figure 4.10 shows the bearing slide and engine mounting fixture and Figure 4.11 shows the complete stand with engine in place.

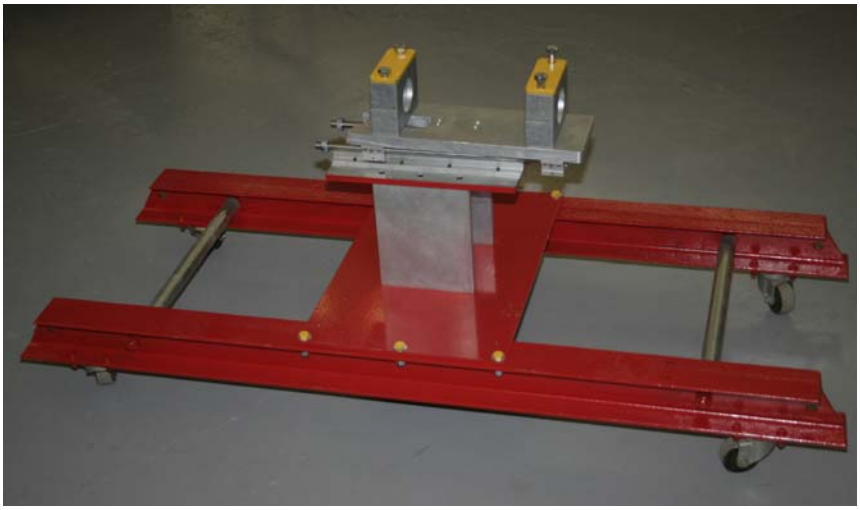

Figure 4.9: Test stand

Figure 4.10: Engine mounting fixture and bearing slide

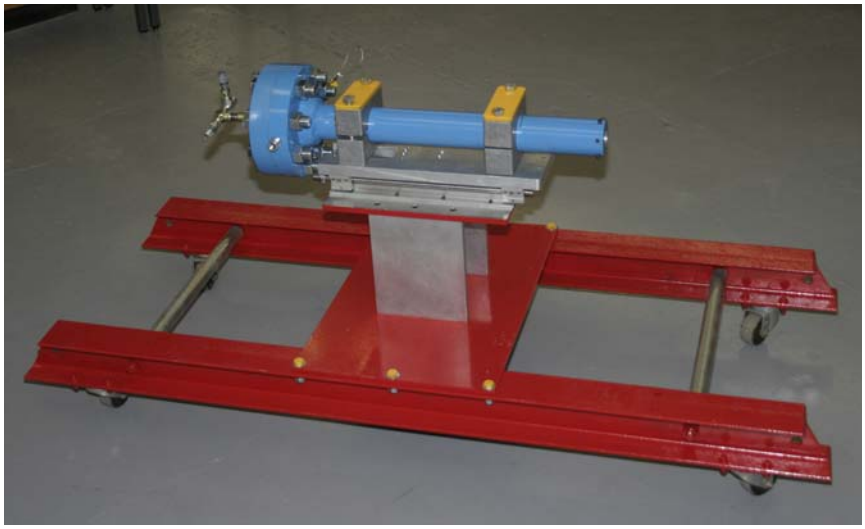

Figure 4.11: Test stand, engine in place

5. Injector

5.1 Injector Design

At its most basic level, the injector of a hybrid rocket engine is responsible for delivering oxidizer to the combustion chamber at the required flow rate. To minimize feed system coupled combustion instability by insuring that pressure oscillations in the combustion chamber do not cause large changes in the oxidizer flow rate, a well-designed injector must additionally offer a sufficiently large pressure drop. Around 20% of the chamber pressure is typical in meeting this requirement.

It should be noted that in hybrid rocket engines that burn liquid oxidizers, the injector must also provide the highest possible degree of atomization of the oxidizer. Unvaporized oxidizer droplets entering the fuel grain port has been noted as a significant source of combustion instability in hybrid rocket engines, particularly those employing liquid oxygen, and these instabilities become particularly significant as engines are scaled up to larger sizes[2]. For the present research, and given that the laboratory engine does not have the same requirement for low weight as would a flight system, it was decided to employ oxygen in its gaseous form as the oxidizer. This serves to simplify the design of the injector, as the requirement for liquid atomization and vaporization is removed.

Given the relatively small size of the research engine, and the small oxidizer flow rate that feeds it, a simple axial orifice was chosen for the injector. These are commercially available as threaded stainless steel inserts, removing the need to fabricate precise

orifices, and further offering the ability to replace the injector orifice for future research, if required. A relatively high pressure drop of 24% of chamber pressure, or 72 psi (496 KPa), was chosen for stability purposes.

For the calculation of the required orifice diameter, the method outlined by Bazarov *et al.*[25] was employed. This approach applies to subsonic flows through the orifice and assumes that the flow is essentially incompressible. The mass flow rate through the injector is given by

$$\dot{m}_i = \mu \rho_2 u_2 A_2 \tag{5.1}$$

where A_2 is the injector orifice area, and ρ_2 and u_2 are the gas density and velocity at the injector exit. μ is the flow coefficient, or ratio of actual to ideal mass flow rate, which for an incompressible fluid is expressed as

$$\mu = \frac{1}{1+\xi_i} \tag{5.2}$$

where ξ_i is the hydraulic loss coefficient of the injector, computed from

$$\xi_i = \xi_{in}\left(1-\frac{d_i^2}{d_1^2}\right)+\lambda\frac{l_i}{d_i} \tag{5.3}$$

Here, d_i is the orifice diameter, d_1 is the diameter of the gas flow upstream of the orifice, and l_i is the length of the orifice. λ is the drag coefficient of the injector passage, expressed for hydraulically smooth pipes in the turbulent regime as

$$\lambda = 0.3164\,\mathrm{Re}^{-0.25} \tag{5.4}$$

ξ_{in} is the hydraulic loss coefficient of the injector inlet and is a function of inlet geometry. For a sharp-edged conical inlet, it is a function of the convergence angle and the ratio of

convergent length to orifice diameter. Based on the geometry of the off-the-shelf orifices used in the present work, it was estimated as 0.25. Assuming isentropic flow through the orifice, the gas density at the exit may be obtained from

$$\rho_2 = \rho_{01}\left(\frac{p_2}{p_{01}}\right)^{1/\gamma} \tag{5.5}$$

and the ideal exit velocity u_2 may be expressed as

$$u_2 = \sqrt{2\frac{\gamma}{\gamma-1}RT_{01}\left[1-\left(\frac{p_c}{p_{01}}\right)^{\frac{\gamma-1}{\gamma}}\right]} \tag{5.6}$$

Note that p_{01}, the total pressure of the flow, is the sum of chamber pressure, p_c, and injector pressure drop Δp_i, and the total temperature T_{01} is the gas temperature upstream of the injector in the manifold.

For a given injector inlet pressure, the exit velocity reaches its theoretical maximum, u_{th}, in the limit of $p_c = 0$. Accordingly, the velocity coefficient λ_2 is defined as

$$\lambda_2 = \frac{u_2}{u_{th}} = \sqrt{\frac{\gamma+1}{\gamma-1}\left[1-\left(\frac{p_c}{p_{01}}\right)^{\frac{\gamma-1}{\gamma}}\right]} \tag{5.7}$$

This allows Eq. (5.1) to be expressed as

$$\dot{m}_i = \mu\frac{(p_c+\Delta p_i)A_n}{c^*}q(\lambda_2) \tag{5.8}$$

where c^* is the characteristic velocity, defined as

$$c^* = \frac{\sqrt{\gamma RT_{01}}}{\gamma\sqrt{\left(\frac{2}{\gamma+1}\right)^{\frac{\gamma+1}{\gamma-1}}}} \tag{5.9}$$

and the gasdynamic function $q(\lambda_2)$ is given by

$$q(\lambda_2) = \lambda_2 \left(\frac{\gamma+1}{2} \right)^{\frac{1}{\gamma-1}} \left(1 - \frac{\gamma-1}{\gamma+1} \lambda_2^2 \right)^{\frac{1}{\gamma-1}} \tag{5.10}$$

An iterative process is used to solve for the orifice diameter, beginning by defining the upstream gas properties γ, R, T_{01}, dynamic viscosity, as well as the target mass flow rate, injector inlet characteristics, injector length, and design injector pressure drop and chamber pressure. The process then proceeds as follows:

1. Assume an initial value of μ
2. Calculate p_{01} and determine λ_2 from Eq. (5.7)
3. Compute $q(\lambda_2)$ from Eq. (5.10)
4. Compute c^* from Eq. (5.9)
5. Determine the orifice area and diameter for the current iteration using Eq. (5.8)
6. Calculate ξ_i from Eq. (5.3) and determine μ from Eq. (5.2)
7. Repeat steps 3-6 until d_i converges

Employing this process suggested a final orifice diameter of 0.113 in. (2.87 mm).

To ensure a constant mass flow rate and a complete decoupling of the feed system from the combustion chamber, an additional choking orifice was inserted into the GOX feed line upstream of the injector. In order to ensure this orifice remains choked over the full range of foreseeable chamber pressures, an upstream pressure of at least 750 psi (5.17 MPa) was required. A 0.076 in. (1.93 mm) orifice was selected as most suitable for this, with an upstream pressure of 782 psi (5.39 MPa).

5.2 Injector CFD Analysis

To further investigate the characteristics of the oxidizer flow as it enters the fuel grain port, a CFD analysis of the injector flow into the combustion chamber was performed using the *FLUENT 6*™ CFD package.

5.2.1 Models[29]

The *FLUENT 6*™ CFD package employs the control volume technique to solve the governing Navier-Stokes equations. These include equations of continuity, momentum and energy for the necessary number of principle directions. In general terms, these are all conservation equations, and can be expressed in integral form as:

$$\int_V \frac{\partial(\rho\phi)}{\partial t} dV + \oint \rho\phi\vec{v} \cdot d\vec{A} = \oint (\Gamma_\phi \nabla\phi) \cdot d\vec{A} + \int_V S_\phi dV \tag{5.11}$$

Discretization of Equation (2.39) for a given control volume yields

$$\frac{\partial(\rho\phi)}{\partial t} V + \sum_f^{N_{faces}} (\rho_f \vec{v}_f \phi_f) \cdot \vec{A}_f = \sum_f^{N_{faces}} (\Gamma_\phi \nabla\phi_f) \cdot \vec{A}_f + S_\phi V \tag{5.12}$$

As this thesis only conducts steady-state CFD analysis, the time-dependent terms may be dropped. The geometry of the injector under study lends itself well to further simplification of the governing equations by treating the problem as 2-dimensional axisymmetric, removing the need to solve the full 3-dimensional equations and greatly reducing the computational requirements.

Equation (5.12) contains the unknown scalar variable ϕ, defined at the centre of the cell, as well as the unknown values in all neighbouring cells. In linearized form, it may be expressed as

$$a_P \phi = \sum_{nb} a_{nb} \phi_{nb} + b \tag{5.13}$$

where the subscript *nb* denotes neighbour cells, and a_P and a_{nb} are the linearized coefficients for ϕ and ϕ_{nb}. The resulting set of algebraic equations within a sparse coefficient matrix is solved using a point implicit (Gauss-Seidel) linear solver.

In order to interpolate face values ϕ_f from the discrete values of ϕ at the cell centres, FLUENT allows the choice of first-order or second-order upwind schemes, as well as power law, QUICK, and MUSCL schemes. The diffusion terms in Equation (5.12) are obtained by central differencing. For this thesis, the QUICK scheme was used. QUICK computes cell face values as a weighted average of second-order upwind and central difference values and offers higher-order solutions for quadrilateral and hexahedral meshes where unique upstream and downstream faces and cells can be identified, and is particularly accurate on structured grids aligned with the flow direction, as is the case in this mesh.

As well as interpolating scalar values at cell faces based on centre values, the computation of gradients is required. FLUENT allows the choice between Green-Gauss Cell-Based, Green-Gauss Node-Based, and Least Squares Cell-Based methods. The gradient of a scalar at the cell center *c0* may be expressed as

$$(\nabla \phi)_{c0} = \frac{1}{V} \sum_f \bar{\phi}_f \vec{A}_f \tag{5.14}$$

where the summation is over all faces enclosing the cell. The different methods for gradient evaluation differ in the way the face values $\bar{\phi}_f$ are computed. The default cell-based method treats them as the arithmetic average of the values at the neighbouring cell centres. The node-based method constructs the face values from the weighted average of the surrounding cell values, and offers greater accuracy for unstructured methods, particularly triangular and tetrahedral. The least-squares method is primarily used for polyhedral meshes. The default, Green-Gauss cell-based method was employed for this thesis.

To completely solve the flow, it is necessary to solve the complete system of Navier-Stokes equations. This is particularly challenging owing to the fact that the velocity field appears in all the momentum equations as well as the continuity equation, and the fact that the pressure appears in all momentum equations, yet there is no unique transport equation for pressure. FLUENT offers two different solvers, each with its own approach for dealing with this. For high-speed, compressible flows, the "density-based" solver is offered. In this approach, the energy equation is used as the transport equation for temperature, while the continuity equation serves as the transport equation for density. The equation of state (for example, the ideal gas law) is then used to compute the pressure. For lower speed incompressible flows, as is expected to be the case in a rocket injector, this method is less appropriate, since density is largely a constant and not linked to pressure by definition. Accordingly, a "pressure-based" solver is provided, and is employed here.

Using this scheme, the pressure field is extracted by solving a pressure or pressure-correction equation which comes from manipulating the continuity and momentum equations. The pressure correction equations are derived from continuity and momentum in such a way that the velocity field, corrected by pressure, always satisfies continuity. Since the governing equations are coupled and nonlinear, the entire set of equations is solved iteratively until the solution converges.

To implement this, FLUENT offers two different pressure-based schemes. In the segregated scheme, the governing equations are decoupled and solved in sequence. This approach is memory-efficient, since the discretized equations only need to be stored in memory one at a time. But, convergence is slow. The solution then proceeds as follows:

1. Update fluid properties (e,g, density, viscosity, specific heat) including turbulent viscosity (diffusivity) based on the current solution.
2. Solve the momentum equations, one after another, using the recently updated values of pressure and face mass fluxes.
3. Solve the pressure correction equation using the recently obtained velocity field and the mass-flux.
4. Correct face mass fluxes, pressure, and the velocity field using the pressure correction obtained from Step 3.
5. Solve the equations for additional scalars such as turbulent quantities and energy using the current values of the solution variables.
6. Update the source terms arising from the interactions among different phases (e.g., source term for the carrier phase due to discrete particles).

7. Check for the convergence of the equations.

These steps are continued until the convergence criteria are met.

Several algorithms for pressure-velocity coupling are provided within the segregated solver, including the default SIMPLE, and its variants SIMPLEC and PISO.

SIMPLEC extends SIMPLE by accelerating convergence in problems where the pressure-velocity coupling is hindering the solution and on highly skewed meshes. PISO performs two additional corrections which can greatly reduce the number of iterations required for convergence, though at the expense of slightly greater CPU time per iteration. It tends to offer superior performance on highly skewed meshes.

SIMPLEC was selected as pressure-velocity coupling algorithm for the solution of the injector model.

In addition to the segregated scheme, a coupled scheme is offered which solves the coupled momentum equations and pressure-based continuity equation simultaneously. The remaining equations (energy, etc.) are solved separately. This approach can offer significant improvement in the rate of convergence, particularly for steady-state flows, or transient flows when the mesh quality is poor, but the memory requirement increases by 1.5 to 2 times. It was decided in the present thesis work to consider this scheme as a fallback in the event of poor convergence with the default, segregated scheme.

As all the flows under study in this thesis are expected to exhibit a nontrivial degree of turbulence, the selection of a suitable turbulence model was necessary. Due to the fact

that the fluctuations in the velocity field that typify turbulent flows may be of high frequency and small scale, direct simulation tends to be too computationally expensive. Accordingly the Reynolds-averaged Navier-Stokes (RANS) equations may be employed, wherein the solution variables in the instantaneous Navier-Stokes equations are decomposed into a mean (ensemble-averaged) component and a fluctuating component. The equations are closed through use of the Spalart-Allmaras single-equation turbulence model for kinematic eddy viscosity. This model provides good accuracy and low computational expense, particularly for flows in which the anisotropy of turbulence does not have a dominant effect on the mean flow (highly swirling flows, for example). It was originally developed for aerospace applications involving wall-bounded flows, which makes it a promising choice for modeling the flow within an injector or nozzle. It is noted however[26] that it is often less effective at accommodating rapid changes in length scale, such as where an abrupt change from a wall-bounded to a free shear flow occurs. As the main objective of the present simulation is to ascertain the performance of the injector orifice, which is wall-bounded, and not to present a detailed study of the resulting oxidizer jet, it is not expected that this will be a significant drawback.

5.2.2 Mesh Generation and Refinement

The basic geometry of the injector orifice, pre-combustion chamber and inlet to the fuel port was determined from preliminary design, as well as the measured geometry of the injector orifice. The GAMBIT mesher was employed to model this geometry, treating it as an axisymmetric problem. To facilitate mesh sensitivity analysis, four meshes were considered: standard, coarse, fine and very fine. All four were structured grids consisting

of quadrilateral elements. These are illustrated in Figures 5.1a, 5.1b, 5.1c and 5.1d, respectively.

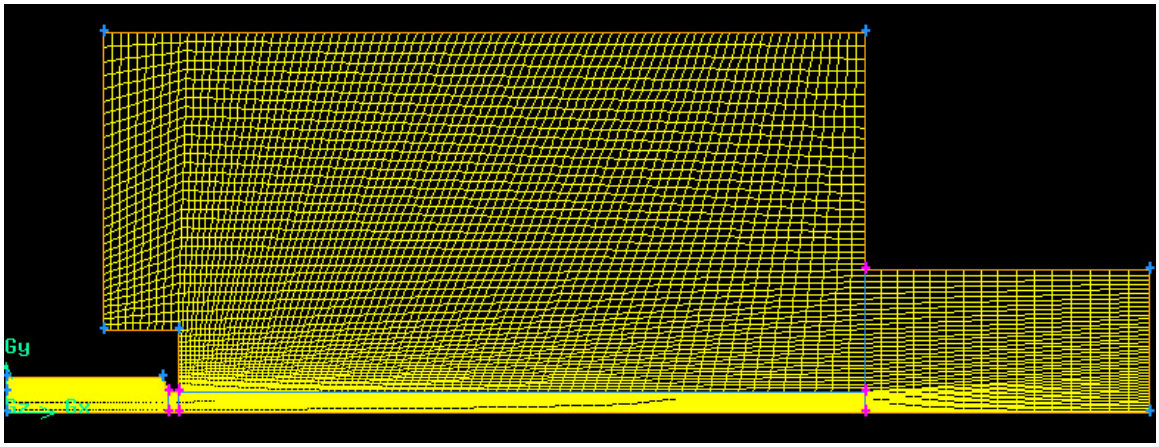

Figure 5.1a: Standard injector mesh

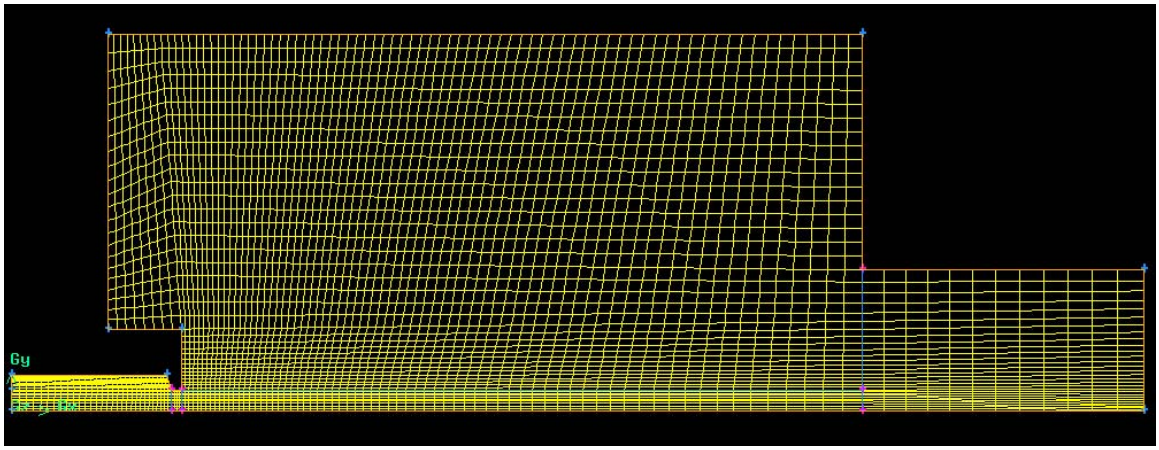

Figure 5.1b: Coarse injector mesh

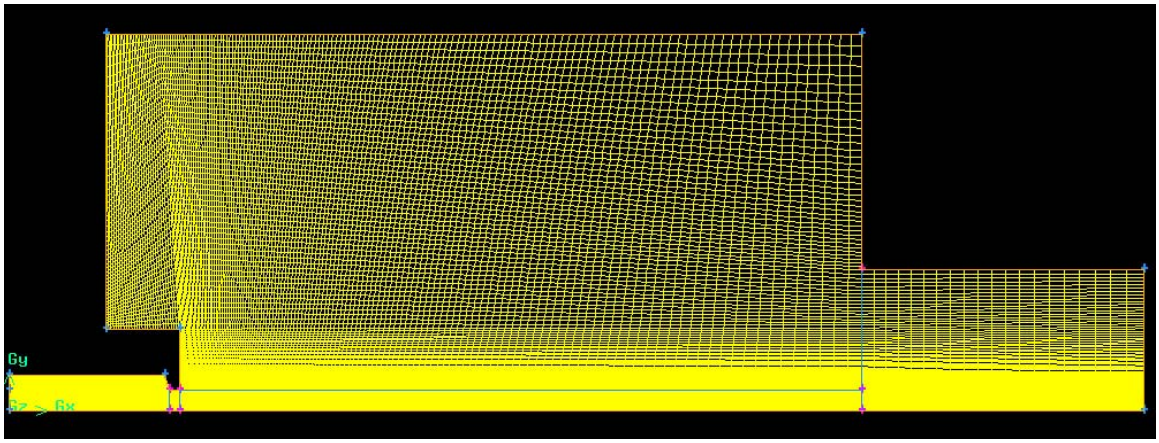

Figure 5.1c: Fine injector mesh

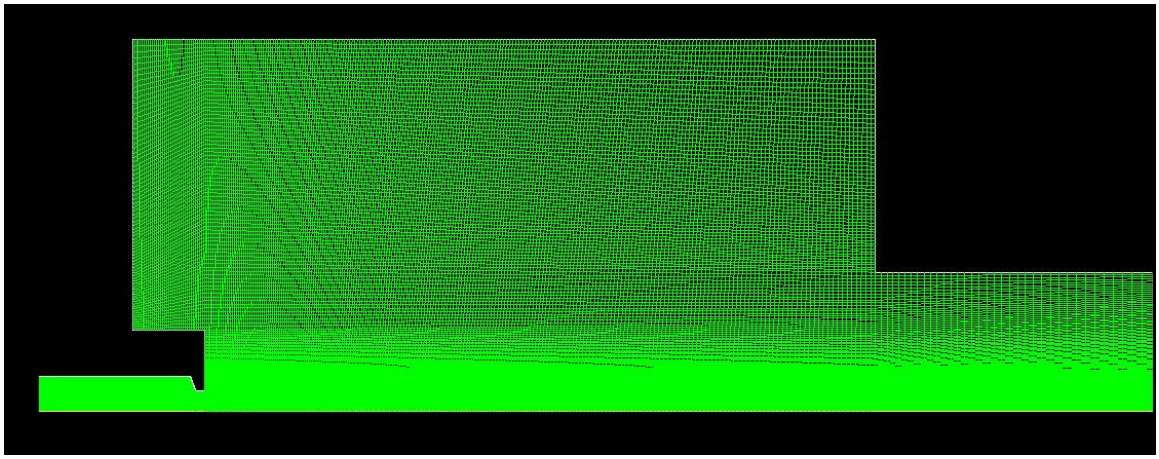

Figure 5.1d: Very fine injector mesh

The standard mesh consisted of 7 668 cells, with a maximum equisize skew of 0.30602. 49.58% of cells in this mesh had a skew of between 0 and 0.1. The coarse mesh included 4 384 cells, with a maximum equisize skew of 0.25219. 70.51% of cells had a skew of between 0 and 0.1. The fine mesh included 25 444 cells, with a maximum equisize skew of 0.49973. 76.16% of cells had a skew of between 0 and 0.1. The very fine mesh included 52 268 cells, with a maximum equisize skew of 0.33440. 90.26% of cells had a skew between 0 and 0.1.

5.2.3 Boundary Conditions

In setting up the problem, the working fluid was treated as an ideal gas and modeled as gaseous oxygen. The lower boundary of the domain was treated as an axis boundary condition. The injector inlet (the leftmost boundary) was set as a mass flow inlet, with a flow rate of 0.0307 kg/s, temperature of 283 K, and an initial guess pressure of 2 564 850 Pa, as determined during the initial injector design. The boundary at the far right of the computational domain was set as a pressure outlet, with the static pressure set to the design chamber pressure of 300 psi (2 068 472 Pa). All other boundaries were set as walls, with the no-slip condition invoked.

5.2.4 Results

For the very fine mesh, the resulting contour plot of velocity magnitude is plotted in Figure 5.2a. The streamlines are illustrated in Figure 5.2b, and a plot of the static pressure contours is shown in Figure 5.2c.

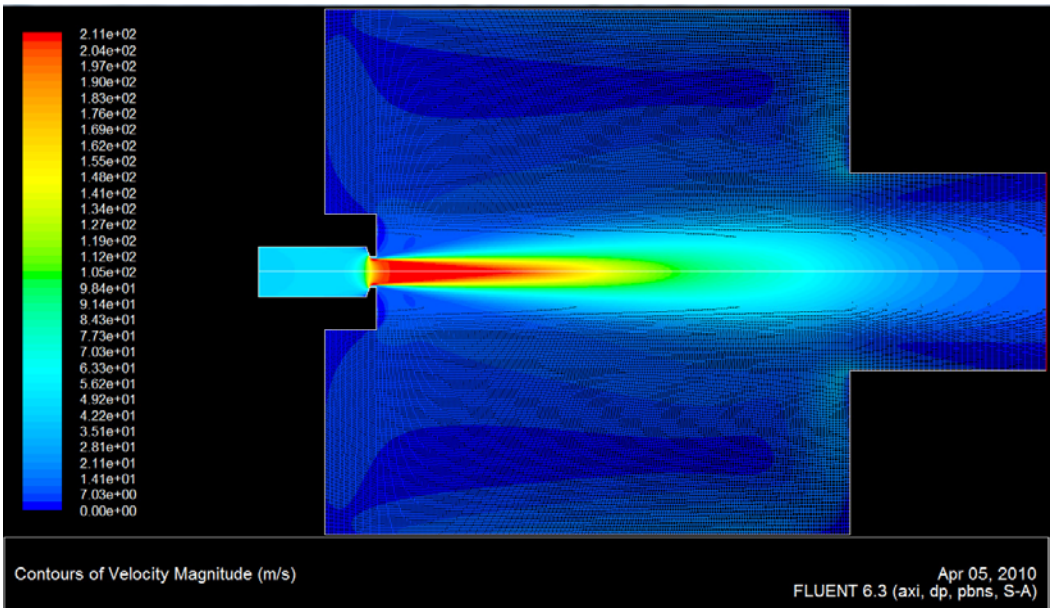

Figure 5.2a: Injector and head-end velocity magnitude

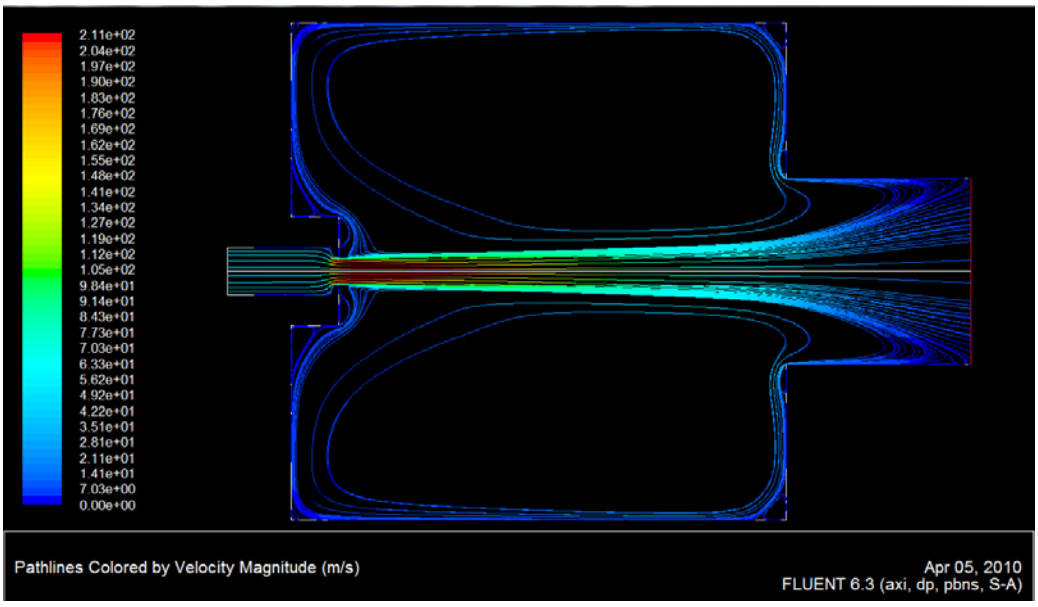

Figure 5.2b: Injector and head-end velocity pathlines

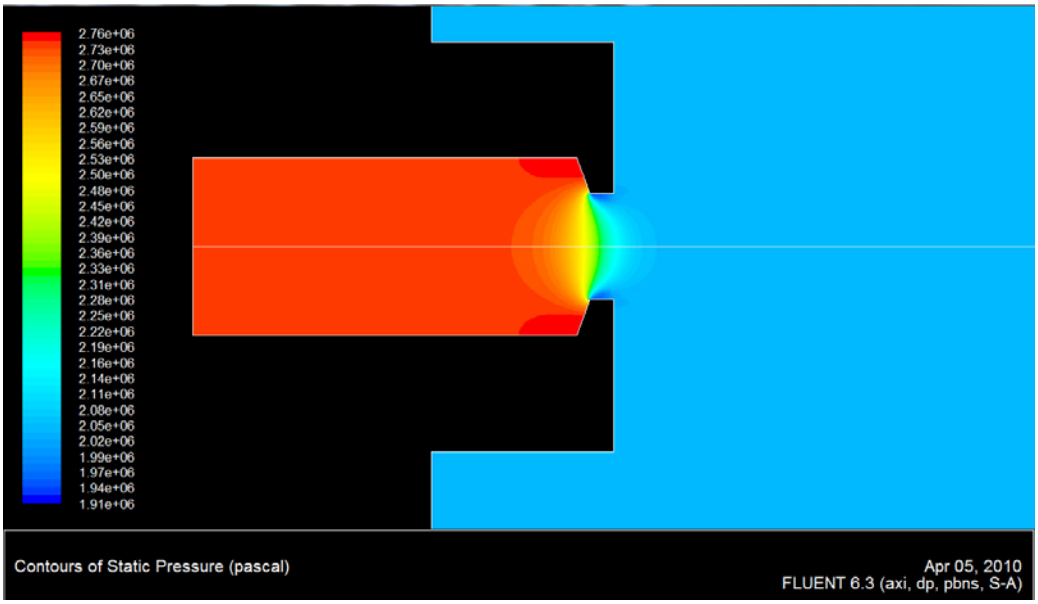

Figure 5.2c: Injector and head-end pressure contours

The velocity profile is as would be expected for a subsonic jet into a quiescent fluid. While less important for a small engine using a gaseous oxidizer, the recirculation zone visible ahead of the fuel grain has been noted as an important feature for stabilizing the combustion of larger hybrid rocket engines employing liquid oxygen, as the hot recirculation gases tend to aid in the vaporization of the oxygen.

For the purposes of verifying the injector design and determining the required injector inlet pressure to achieve the designed-for GOX flow rate, the static pressure across the inlet to the injector is plotted in Figure 5.3a. The computed inlet pressure distributions for all four meshes are included to facilitate the examination of the sensitivity of the solution to the chosen meshes.

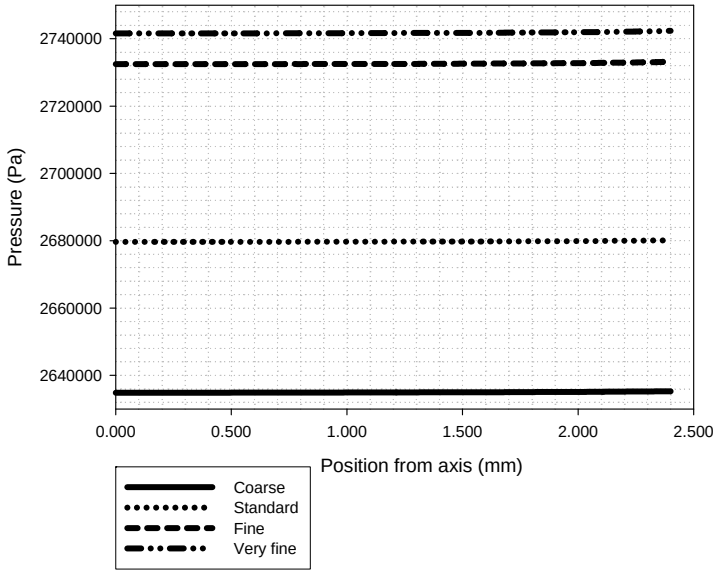

Figure 5.3a: Injector inlet static pressure distribution

From the figure, it is clear that the solution did not reach the point of being mesh independent, but that the change in the inlet pressure from refining the mesh was decreasing considerably. The very fine mesh included more than twice the number of cells as the fine mesh, yet the difference between their respective solutions for inlet pressure was comparatively small. Substantial further refinement of the mesh was impractical given the computational power available, but evidently it was becoming a case of diminishing returns.

For further comparison of the solution, the static pressure at the injector orifice's exit plane is plotted for all four meshes in Figure 5.3b.

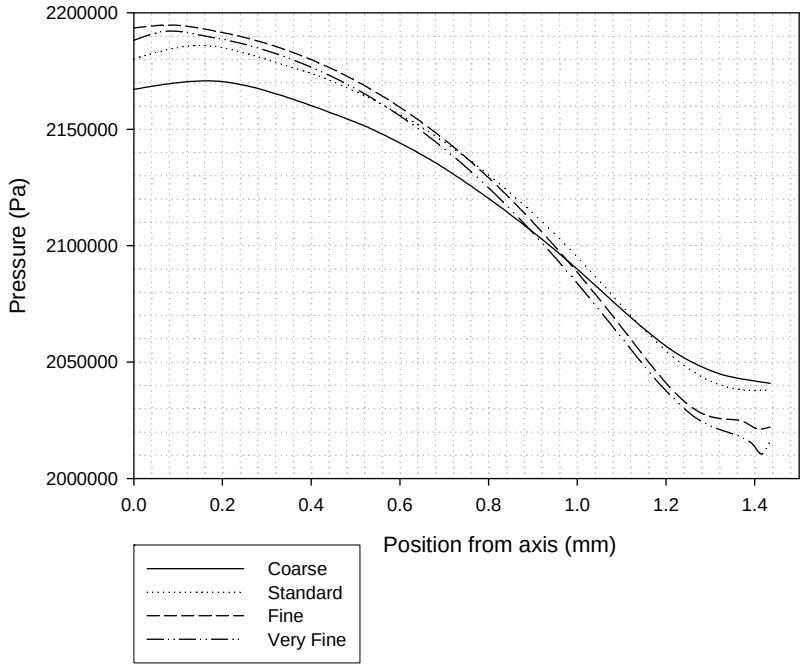

Figure 5.3b: Injector orifice exit static pressure distribution

From the plot, it may be seen that the coarser meshes appear to have a tendency to underpredict the extent to which the exit pressure varies radially. This is as would be expected, given the fact that coarser meshes will tend to be less effective at resolving the viscous effects in the boundary layer near the injector wall. As with the inlet pressure, it is clear that the change in the pressure profile from the fine mesh to the very fine mesh was comparatively minor. As one additional point of comparison, Figure 5.3c illustrates the variation of pressure along the axis for the four meshes.

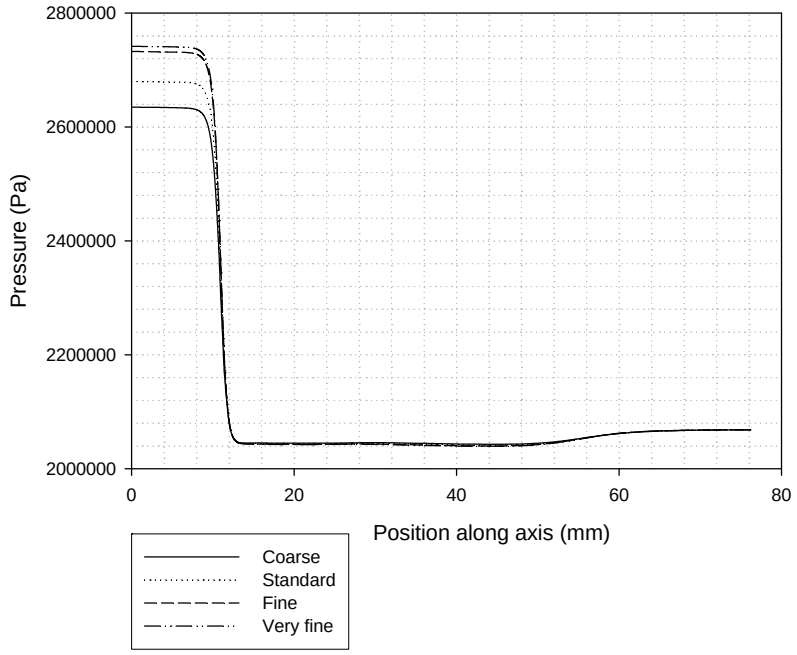

Figure 5.3c: Injector axis static pressure distribution

The sharp drop in static pressure as the flow is accelerated through the injector orifice may be clearly noted. The static pressure profiles downstream of the orifice are virtually identical, while the upstream pressure shows the same trend observed in the other plots, with the pressure tending to converge as the mesh is refined.

Based on the solution obtained with the different meshes, the computed inlet pressure is increasing as the mesh is refined, but that increase is clearly diminishing with further refinement of the mesh. It may thus be safely concluded that the required inlet pressure will be higher than that obtained with the very fine mesh, but only slightly. For the very fine mesh, the inlet pressure varied from 2.7416 MPa to 2.7423 MPa (398 psia). For the fine mesh, by comparison, the inlet pressure varied from 2.7325 MPa to 2.7331 MPa (396 psia). Thus in order to yield the target mass flow rate of 0.0307 kg/s, it appears that an

inlet pressure of approximately 2.75 MPa (399 psia) is required. This in turn suggests a roughly 99 psi average pressure drop across the injector to achieve the target flow rate. This is quite a bit higher than the 372 psia inlet pressure that was called for in the design, suggesting that either the CFD results overpredict the pressure drop through the injector, or that the calculations underpredict it. Experimental data will be required to determine which of the two approaches more closely corresponds to reality.

6. Nozzle

6.1 Nozzle Design

6.1.1 Design Considerations

The nozzle throat and exit area were determined during the preliminary design based on the design chamber pressure, the ambient (sea level) pressure, the design mass flowrate and the characteristic velocity. For the nozzle inlet, a 120° (full angle) conical convergent section was selected. Due to the nozzle's small size, an optimized, minimum-length nozzle contour designed to maximize efficiency would be prohibitively expensive to manufacture. Accordingly, the divergent section was designed as a 12° (full angle) cone. The preliminary nozzle design is shown in Figure 6.1.

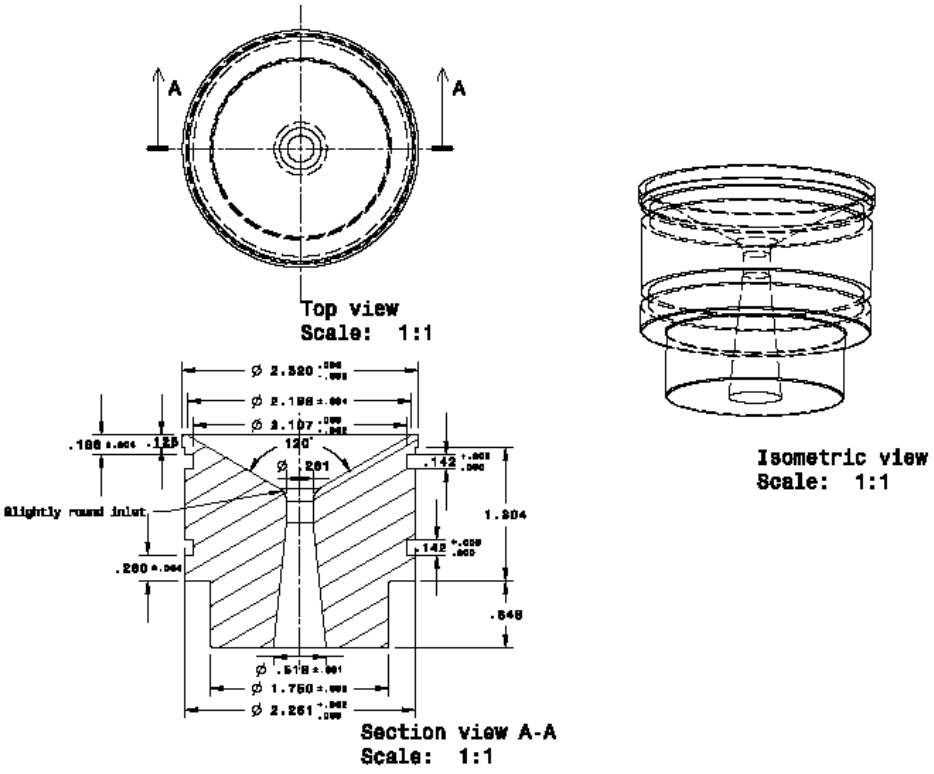

Figure 6.1: Preliminary nozzle configuration

The nozzle blank was designed to fit into the aft end of the combustion chamber, butting against the chamber liner and secured in place with the nozzle retaining ring. A gas-tight seal was provided by a pair of high temperature silicone O-rings.

Having determined the basic nozzle geometry for the test engine, the remaining practical consideration was which cooling approach to use. For the purposes of this thesis, two different versions of the nozzle were considered. In the interest of simplicity, ease of manufacturing, and low cost, the first nozzle produced was an uncooled version fabricated from high-density graphite. Preliminary calculations indicate that this nozzle should offer acceptable performance for relatively short duration initial firings. The

drawback of a graphite nozzle is its tendency to erode over time. If the graphite is exposed to an oxidizer-rich environment, the problem of erosion is greatly exacerbated. This erosion will place a limit on the life of a given graphite nozzle, while also causing the nozzle's performance to vary over the course of a given firing. For long-term experimental use, it is therefore desirable to have a nozzle that does not experience erosion, and so a water-cooled nozzle was also designed, and its performance modeled computationally. The time and resources available for the present project did not allow for the construction of this nozzle; its completion will be left for future work.

6.1.2 Uncooled Version

Graphite has been widely used in rocket nozzles due to its excellent resistance to high temperatures, good machinability, ready availability and relatively low cost. Early rocket nozzles, particularly in small, single-use solid propellant vehicles, were frequently machined from a single piece of graphite and this approach is still common for applications involving short durations and relatively low chamber pressures and thrust levels.

The disadvantages of graphite include relatively high weight, brittleness, and a tendency to experience erosion under the flow conditions typically present in rocket engines. The exact erosion rate is a strong function of the actual thermal and chemical conditions in the boundary layer over the nozzle surface. In particular, an oxidizing atmosphere at elevated temperatures can rapidly consume graphite. The presence of soot or particulates in the exhaust gas can also produce an abrasive action that will accelerate the erosion of a

nozzle. Additionally, graphite stock tends to vary widely in its quality and properties. These factors all make it difficult to calculate the expected erosion rates for a graphite nozzle with any accuracy, but it has been observed that typical erosion rates are around 0.004 – 0.006 in/sec (0.10-0.15 mm/s)[3]. Initial short-duration test firings will be required to better quantify the erosion behaviour of this nozzle with this HRE.

6.1.3 Cooled Version

To meet the requirements for a robust, versatile and reusable testbed, a non-eroding nozzle will ultimately be required. To guarantee this, a water-cooled nozzle was designed. This design offers the added benefit of allowing the cooling water temperature rise to be measured to quantify heat flux into the nozzle. Copper was selected as the nozzle material due to its extremely high thermal conductivity.

To estimate the gas-side nozzle heat flux in the convergent, throat and divergent sections, the method of Bartz[27] was employed, using the nozzle geometry, the combustion gas properties estimated with NASA's CEA code, and the requirement that the wall temperature not exceed 773 K. This approach tends to be conservative and was oriented towards producing a nozzle that will allow continued steady-state operation. The cooling problem was somewhat greater for such a small nozzle owing to the very high heat fluxes involved, and the difficulties of manufacturing anything but the simplest cooling passages at such a small scale.

This method begins by noting that the heat transfer from the combustion gases through the boundary layer to the nozzle wall may be expressed as

$$\dot{q} = h_g (T_{aw} - T_{wg}) \tag{6.1}$$

where T_{wg} is the gas-side wall temperature, typically a design input based on the maximum allowable temperature of the wall material. For the copper nozzle under consideration, this was taken to be 773 K. T_{aw} is the adiabatic wall temperature, which may be expressed in terms of the core (freestream) gas temperature and the effective recovery factor R, according to

$$T_{aw} = T_c R \tag{6.2}$$

where

$$R = \frac{1 + r\left(\frac{\gamma - 1}{2}\right)\mathrm{Ma}^2}{1 + \left(\frac{\gamma - 1}{2}\right)\mathrm{Ma}^2} \tag{6.3}$$

where the Mach number Ma and ratio of specific heats γ refer to the freestream conditions. The local recovery factor r, is the ratio of temperature increase due to friction, to that caused by adiabatic compression. This experimentally-determined value has been observed[1] to be typically around 0.91.

In Equation 6.1, the term h_g is the gas-side convective heat transfer coefficient. In SI units, it may be expressed as

$$h_g = \frac{4.18237 \times 10^{-3}}{D_t^{0.2}} \left(\frac{\mu^{0.2} C_p}{\mathrm{Pr}^{0.6}}\right) \left(\frac{p_c g}{c^*}\right)^{0.8} \left(\frac{D_t}{R}\right)^{0.1} \left(\frac{A_t}{A}\right)^{0.9} \sigma \tag{6.4}$$

R here refers to the radius of curvature at the nozzle throat, and σ is a correction factor for property variations across the boundary layer, expressed as

$$\sigma = \frac{1}{\left[\frac{1}{2}\frac{T_{wg}}{T_c}\left(1+\frac{\gamma-1}{2}\mathrm{Ma}^2\right)+\frac{1}{2}\right]^{0.68}\left[1+\frac{\gamma-1}{2}\mathrm{Ma}^2\right]^{0.12}} \tag{6.5}$$

In cases where the freestream Prandtl Number and dynamic viscosity are not known, it is noted by Huzel and Huang[28] that they may be estimated from

$$\mathrm{Pr} = \frac{4\gamma}{9\gamma-5} \tag{6.6}$$

and

$$\mu = 11.8408\text{x}10^{-8}\mathcal{M}^{0.5}T^{0.6} \tag{6.7}$$

One of the implications of Equation (6.4) is that the convective heat transfer reaches its maximum when the nozzle cross-sectional area *A* reaches its minimum, at the throat. This is thus the region that primarily drives the preliminary design.

Knowing the convective heat flux to the nozzle wall, steady state operation requires that this heat be transferred via conduction through the nozzle wall and into the coolant:

$$\dot{q} = \frac{k_{\text{wall}}}{t_{\text{wall}}}(T_{wg} - T_{wc}) \tag{6.8}$$

For a given wall material with thermal conductivity k_{wall} and thickness t_{wall}, and subject to the constraint that the wall thickness be sufficient to prevent the nozzle from failing structurally, Equation (6.8) will dictate the required coolant-side wall temperature to achieve that heat flux, as well as providing an early indicator of the feasibility of a given nozzle material.

Having calculated T_{wc}, the convective heat flux into the coolant itself may be determined from

$$\dot{q} = h_c (T_{wc} - T_{coolant}) \tag{6.9}$$

where h_c may be determined by invoking the definition of the Nusselt number

$$h_c = \frac{\mathrm{Nu}\, k_c}{D_c} \tag{6.10}$$

for a coolant with thermal conductivity k_c in a channel with hydraulic diameter D_c. The Nusselt number may be estimated for fully-developed turbulent flow in a pipe from the Colburn equation

$$\mathrm{Nu} = 0.023\,\mathrm{Re}^{0.8}\,\mathrm{Pr}^{0.4} = 0.023\left(\frac{u_c D_c}{\nu_c}\right)^{0.8}\left(\frac{\mu_c C_{p_c}}{k_c}\right)^{0.4} \tag{6.11}$$

and the coolant velocity u_c may be related to the pressure drop across the cooling passage, assuming a total length L_c, by the pipe flow equation

$$\Delta p = f\,\frac{L_c}{D_c}\frac{\rho_c u_c^2}{2} \tag{6.12}$$

where the friction factor f may be estimated from the Colebrook approximation for turbulent pipe flows

$$\frac{1}{\sqrt{f}} = -2\log\left(\frac{\varepsilon/D}{3.7} + \frac{2.51}{\mathrm{Re}\sqrt{f}}\right) \tag{6.13}$$

for a passage relative surface roughness ε/D.

Proceeding iteratively, a simple annular coolant passage was then designed to provide a sufficiently high h_c without requiring an unrealistically high coolant pressure drop. This

passage had a depth of 19.8 mm and width of 15.2 mm and should provide adequate cooling with a pressure drop of approximately 30 psi. The heat transfer calculations and cooling passage design are summarized in Table 6.1:

Table 6.1: Summary of nozzle cooling passage design

Gas-Side Heat Transfer				
	Chamber	***Throat***	***Exit***	***Units***
T_c:	3400	3054	1853	K
$\mathcal{M}$:	21.16	21.16	21.16	kg/kmol
C_p:	2136	2111	1960	J/Kg-K
g:	1.230	1.230	1.250	
T_{wg}:	773	773	773	K
Ma:	0.2000	1.0000	2.6500	
A:	0.002347	3.5E-05	0.000136	m^2
Pr:	0.810544	0.810544	0.8	
m:	7.16E-05	6.72E-05	4.98E-05	Pa-s
s:	1.392228	1.356136	1.166458	
h_g:	270.6879	11327.4	2522.776	W/m^2-K
Conduction Through Nozzle Wall				
T_{aw}:	3399	3368	3257	K
$\dot{q}$:	710717.87	29399593	6266463	W/m^2
t_{wall}:	0.015	0.003	0.003	m
T_{wc}:	744.18711	534.6249	722.1908	K
Coolant-Side Heat Transfer				
$T_{coolant}$:	280	K		
h_c required:	1530.8946	115433.8	14169.38	W/m^2-K
Cooling Passage Design				
Channel Height:	15.2	mm		
Channel Width:	19.8	mm		
D_c:	17.2	mm		
u_c:	50.0	m/s		
h_c:	120476	W/m^2-K		
L_c:	0.1788	m		
Dp:	27.39	psid		

This approach resulted in a preliminary cooling passage design that appears to provide sufficient cooling while also being feasible to manufacture. In order to verify the design further, a CFD analysis of the nozzle flow and associated heat transfer was performed using the *FLUENT 6*™ CFD package.

6.2 Nozzle CFD Analysis

CFD analysis of a rocket nozzle during a static firing at sea level presents many complexities that make it a considerable challenge to model, particularly where computational resources are limited. Ideally, the mesh used should encompass not only the nozzle but a sufficiently large region of the ambient air surrounding it to ensure that ambient static pressure may be specified at the boundaries, without interference from the nozzle exhaust jet. The resulting scenario, that of a supersonic gas jet entering a quiescent fluid, tends to be difficult for CFD packages to accurately model owing to the presence of such widely varying flow regimes. The shear and turbulent mixing between the exhaust jet and the ambient air adds additional complexity, which is compounded by the fact that the composition of the exhaust gas differs from that of the surrounding air, and many of the gas properties, including the relative proportions of the species that compose it, vary as it expands and cools through the nozzle.

In order to render this problem tractable within the scope of the present thesis the nozzle CFD analysis proceeded in two parts. In the first part, a relatively coarse mesh was generated to include the nozzle (both internal flow and the solid structure) and the

surroundings. To simplify the modeling of the jet, the chemical kinetics and the turbulent mixing, the working fluid was treated as air and modeled as an ideal gas.

In the second part, the problem was restricted to the nozzle core flow and surrounding structure, but the combustion gases were modeled based on NASA CEA simulations to give a more accurate model of the heat fluxes from the nozzle flow to the wall. The coolant passage was added to the model, and a pressure outlet boundary was placed at the nozzle outflow.

6.2.1 Models

As with the injector, the *FLUENT 6*™ CFD package was used, employing the control volume technique to solve the governing Navier-Stokes equations of continuity, momentum and energy.

Once again, the steady-state solver was used, and the axial symmetry of the problem was invoked to remove the need to solve the full 3-dimensional equations and greatly reduce the computational requirements.

Due to the fact that the flow of greatest interest was supersonic, FLUENT's "density-based" (or coupled) solver was used, employing the energy equation as the transport equation for temperature, the continuity equation as the transport equation for density, and the ideal gas law for the computation of the pressure. FLUENT`s solution algorithm proceeds as follows:

1. Update the fluid properties based on the current solution. (If the calculation has just begun, the fluid properties will be updated based on the initialized solution.)

2. Solve the continuity, momentum and energy equations simultaneously.
3. Solve equations for turbulence using the previously updated values of the other variables.
4. Check for convergence of the equation set.

These steps are continued until the convergence criteria are met.

FLUENT offers the choice of either a density-based implicit solver or a density-based explicit solver, each relating to how the governing equations are linearized. In the implicit scheme, the unknown value of a given variable in each cell is computed from a relation that includes both existing and unknown values from the neighbouring cells. Since this means that each unknown will appear in multiple equations, the system must be solved simultaneously. This approach offers broader stability characteristics, and tends to allow a converged steady-state solution to be obtained much faster. The scheme is also unconditionally stable regardless of the Courant number chosen, though lower Courant numbers can be required during startup, when changes in the solution are highly nonlinear. Although being comparatively memory-intensive, the method's stability characteristics motivated its selection for this thesis.

The point-implicit (Gauss-Seidel) linear solver was used to solve the linearized equations. In order to interpolate face values ϕ_f from the discrete values of ϕ at the cell centres, FLUENT's density-based solver allows the choice of first-order or second-order upwind schemes, as well as the MUSCL scheme. As the nozzle flow introduces the added complexity of supersonic flow and the shock waves this implies, a second-order accurate

solution was desired, since first-order solutions tend not to adequately resolve these regions. Accordingly, second-order upwinding was used for the flow, and the QUICK scheme was employed for the modified turbulent viscosity.

For the evaluation of gradients and derivatives, the default Green-Gauss cell-based method was employed, and convective fluxes were computed using the Advection Upstream Splitting Method (AUSM+) scheme. This method provides exact resolution of contact and shock discontinuities, and is known to be free of oscillations at both stationary and moving shocks[29].

As with the injector simulations, the Reynolds-averaged Navier-Stokes (RANS) equations were employed, closed through use of the Spalart-Allmaras single-equation turbulence model for kinematic eddy viscosity.

6.2.2 Mesh Generation and Refinement

Having determined the geometry of the nozzle from the preliminary and detailed design phases, the GAMBIT mesher was employed to model this geometry, treating it as an axisymmetric problem as was done with the injector. Initially, a relatively coarse structured mesh was generated consisting of quadrilateral elements, but having sufficient density to resolve the important geometry of the nozzle. This is illustrated in Figure 6.2a.

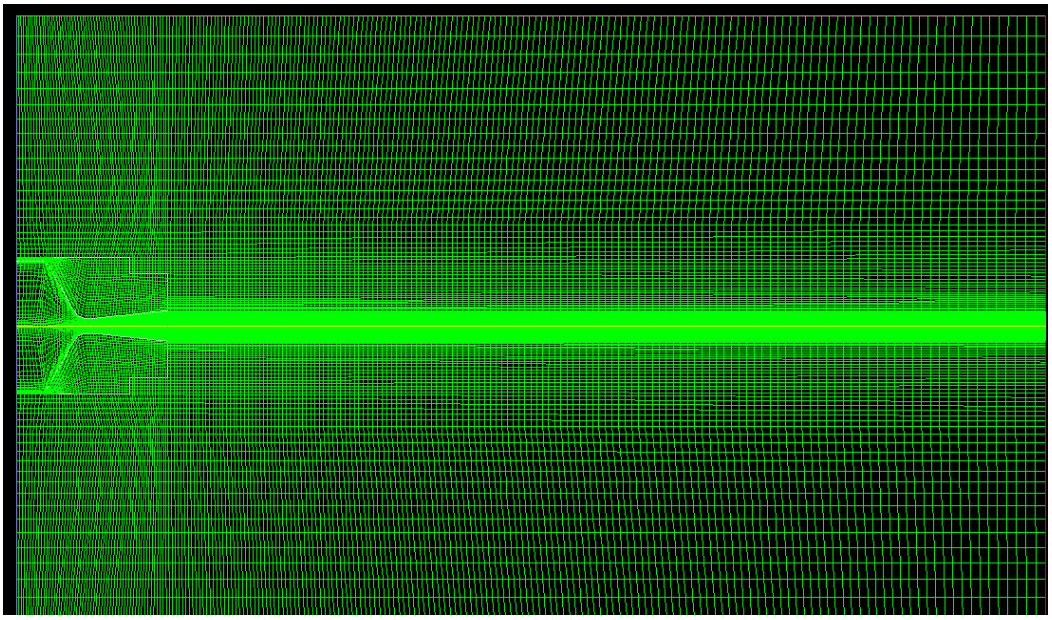

Figure 6.2a: Initial nozzle mesh

To facilitate mesh sensitivity analysis, FLUENT's adaptive meshing capabilities were employed to selectively refine this mesh in areas of particularly large gradients, high residuals, and large changes between neighbouring cell sizes. The resulting refined meshes are illustrated in Figures 6.2b and 6.2c.

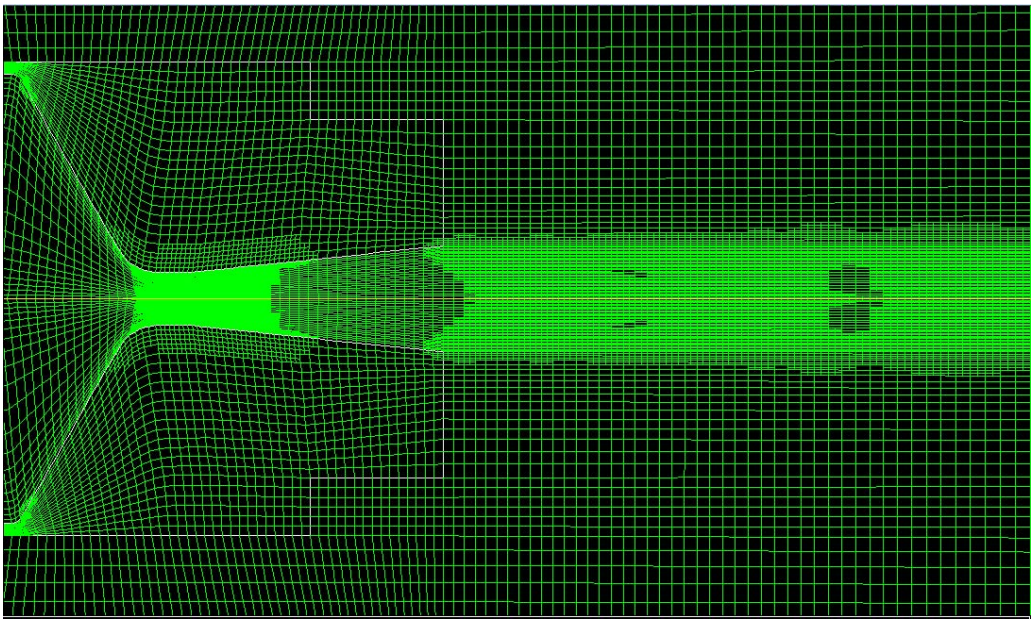

Figure 6.2b: Nozzle mesh, first adaption, detail

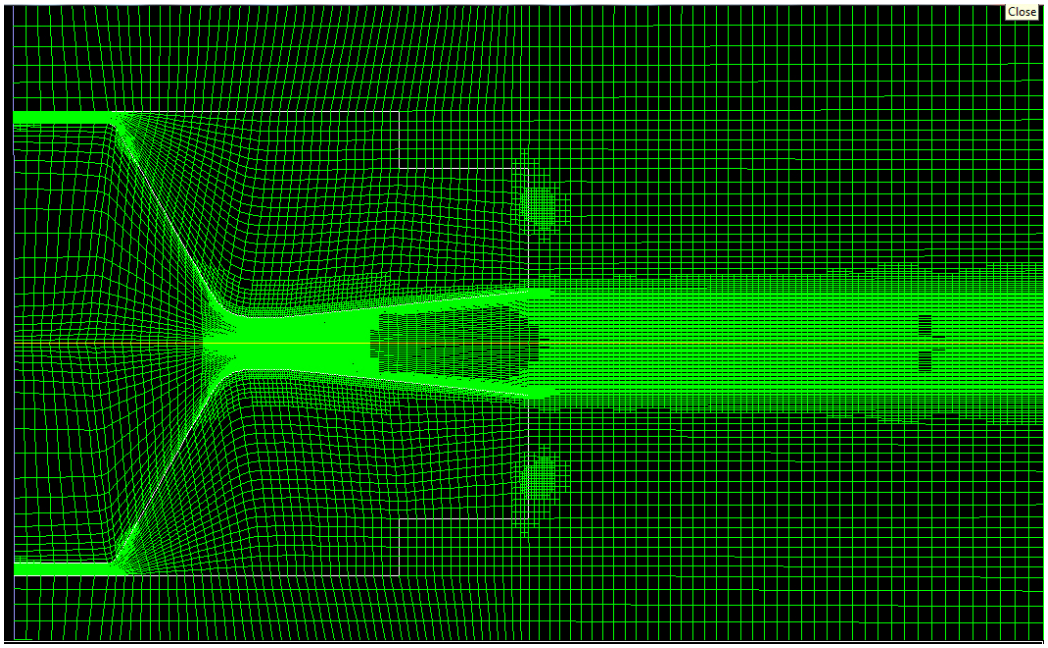

Figure 6.2c: Nozzle mesh, second adaption, detail

The initial coarse mesh consisted of 13 184 cells, with a maximum equisize skew of 0.82. 93.33% of cells in this mesh had a skew of between 0 and 0.1. After obtaining a converged 1st order solution with the coarse mesh, hanging-node isovalue adaption was performed based on the pressure residual, refining when the absolute value of the residual exceeded 50. To improve mesh quality, this was followed by volume adaption in order to keep changes in cell volume gradual. This was done based on the criterion that the change in volume between a given cell and its neighbours not exceed 2.5. The resulting mesh consisted of 25 115 cells, and offers much better resolution of shocks.

After obtaining a second-order solution on the refined mesh, a second hanging-node adaption was performed based on gradients of total pressure, followed again by volume adaption and a Laplace smoothing operation. The resulting mesh consisted of 61 967 cells.

An additional mesh was generated to investigate the water-cooled nozzle. This was created as a truncated version of the original meshes of Figures 6.2a – 6.2c, with the addition of the cooling passage and a pressure outlet boundary placed at the nozzle exit. The final version of this mesh, after isovalue adaption based on pressure residuals, volume adaption and smoothing consisted of 15 395 elements and is shown in Figure 6.2d.

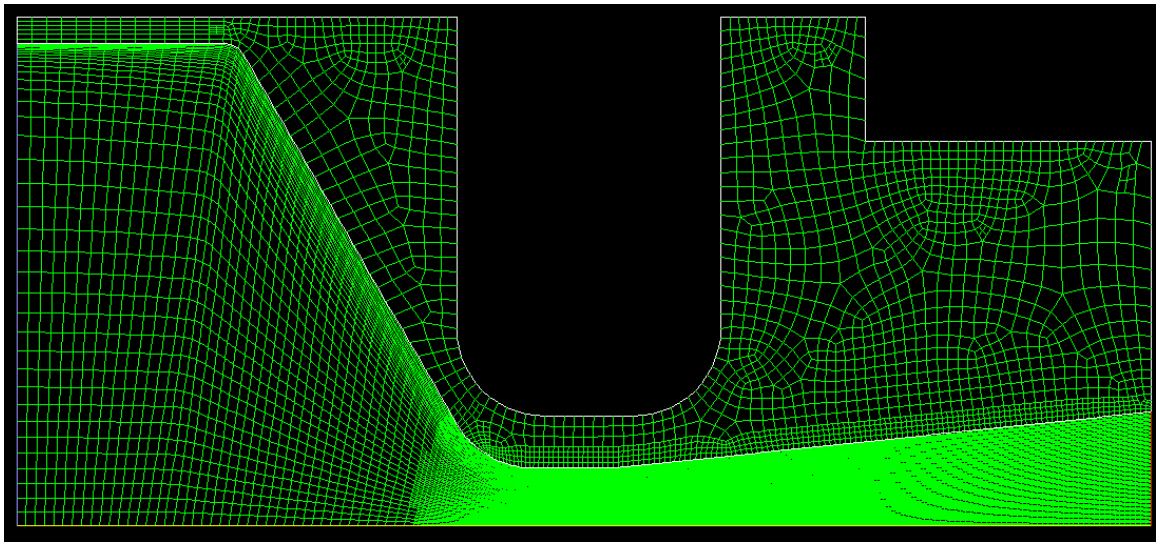

Figure 6.2d: Cooled nozzle mesh

6.2.3 Boundary Conditions

In setting up the problem, the working fluid was initially treated as a compressible ideal gas and modeled as air. The lower boundary of the domain was treated as an axis boundary condition. The inlet to the nozzle (the leftmost boundary) was set as a pressure inlet, with a gauge total pressure of 2.07 MPa (corresponding to the 300 psia design chamber pressure), temperature of 3200 K, and an initial guess pressure of 2 068 500 Pa,

as determined during the HRE's preliminary design. The turbulent viscosity ratio was set at 10. The boundary at the far right of the computational domain was set as a pressure outlet, with the static pressure set to ambient conditions (101 325 Pa), and a backflow total temperature of 300 K. A pressure far-field boundary was used for the topmost boundary of the computational domain, again with static pressure set to 101 325 Pa and temperature of 300 K, and the leftmost boundary of the domain was set as a pressure inlet with 101 325 Pa pressure and 300 K temperature. For the initial problem, conjugate heat transfer from the core nozzle flow and into the nozzle structure was also modeled, treating the nozzle wall as copper. While the primary purpose of this initial simulation was to investigate the core nozzle flow and not to look in great detail at heat transfer into the nozzle, the problem was set up in this way to allow for a better comparison with the cooled nozzle results.

To speed convergence, functions were defined for pressure (P1) and temperature (T1) to initialize these values within the convergent portion of the nozzle. These were simple linear interpolations based on the calculated pressure and temperature at the inlet and the throat. The functions used were:

$$P1 = 2\,068\,500 - 30\,050\,812\,x$$

$$T1 = 3200 - 16\,805\,x$$

For the cooled nozzle, two different working fluids were used. Initially, air modeled as a compressible ideal gas was employed to allow this truncated model to be compared with the original model that included the full exhaust jet to verify that the flow within the

nozzle was sufficiently similar to enable meaningful results. After this "calibration" run, the working fluid was changed to one that better approximated the engine exhaust gases. No attempt was made to model the variation of transport properties or the change in combustion gas composition through the nozzle, and instead these were considered "frozen" in the chamber. The relevant gas properties used in this model were determined from NASA CEA simulation and are summarized in Table 6.2.

Table 6.2: Combustion gas model

Density:	(ideal gas)	
Cp:	2179	J/kg-K
Thermal Conductivity:	0.3624	W/m-K
Viscosity:	0.0001036	kg/m-s
Molecular Wt:	20.3	kg/kmol

At the inlet of this nozzle, the same pressure inlet boundary condition was used. The pressure outlet boundary was relocated to the nozzle exit, and the wall boundary that defines the cooling passage was set as insulating (zero heat flux) for the first run using air. For the runs modeling the actual combustion gas, the cooling passage wall boundary was modified to account for convective heat transfer, with a heat transfer coefficient of 80 000 W/m^2-K and freestream temperature of 300 K. The choice of 80 000 W/m^2-K was motivated by a conservative reduction of the h_c for the cooling passage calculated in section 6.1.3.

6.2.4 Results

For the second adapted mesh, the resulting contour plot of Mach number is plotted in Figure 6.3a. Static pressure contours are illustrated in Figure 6.3b, and contours of static temperature are shown in Figure 6.3c.

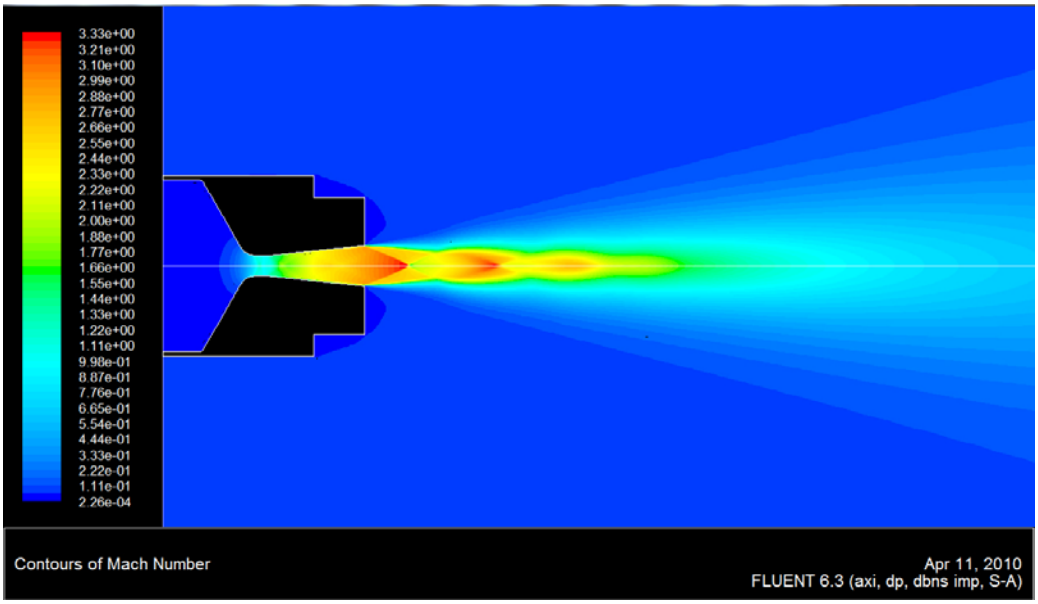

Figure 6.3a: Mach contours, second adapted mesh, uncooled nozzle

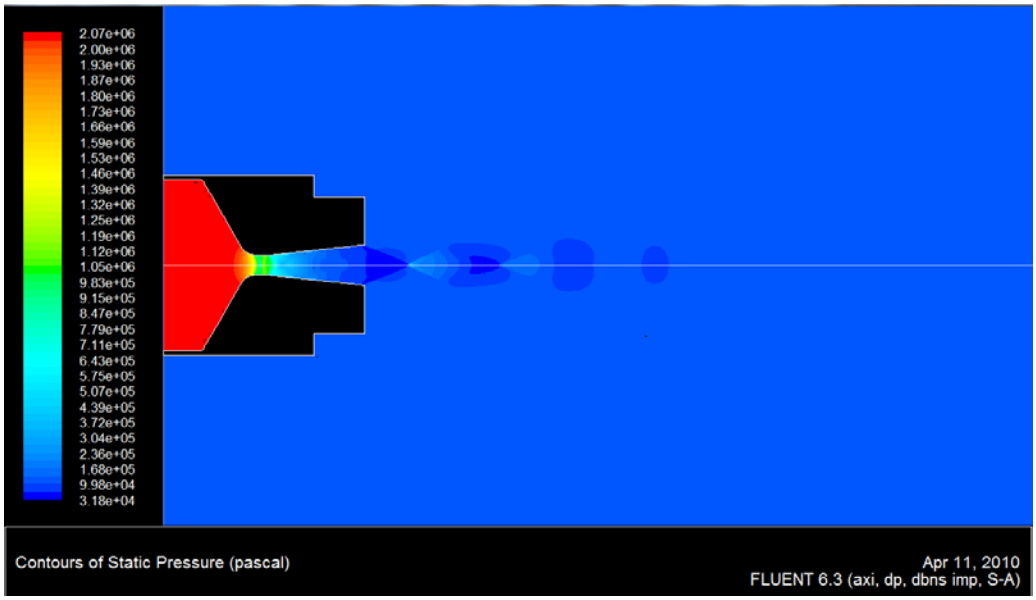

Figure 6.3b: Static pressure contours, second adapted mesh, uncooled nozzle

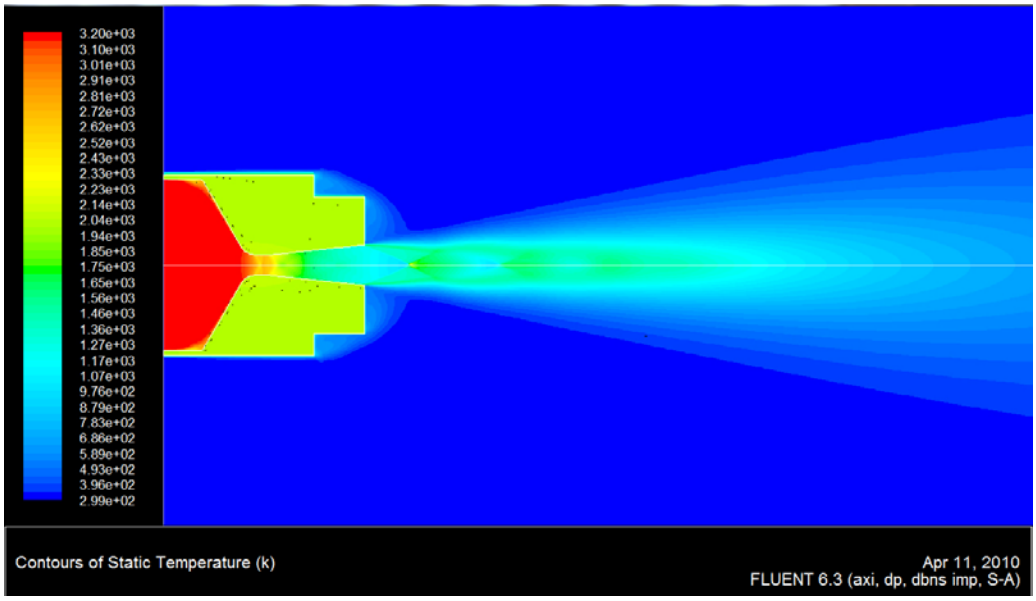

Figure 6.3c: Static temperature contours, second adapted mesh, uncooled nozzle

Although several features of this initial model are distinctly nonphysical, such as the use of 3200 K air as the working fluid and the copper nozzle structure at approximately 2000 K, the plots are nevertheless as would be expected for a flow expanding through a supersonic nozzle, with the flow choking and becoming sonic in the throat region.

To provide a more quantitative comparison, a mesh sensitivity analysis was performed in order to assess the solutions provided by the three uncooled nozzle meshes of figures 6.2a – 6.2c. Plots of the axial velocity, static pressure, and static temperature along the nozzle axis were generated for all three meshes and are shown in figures 6.4a, 6.4b and 6.4c, respectively.

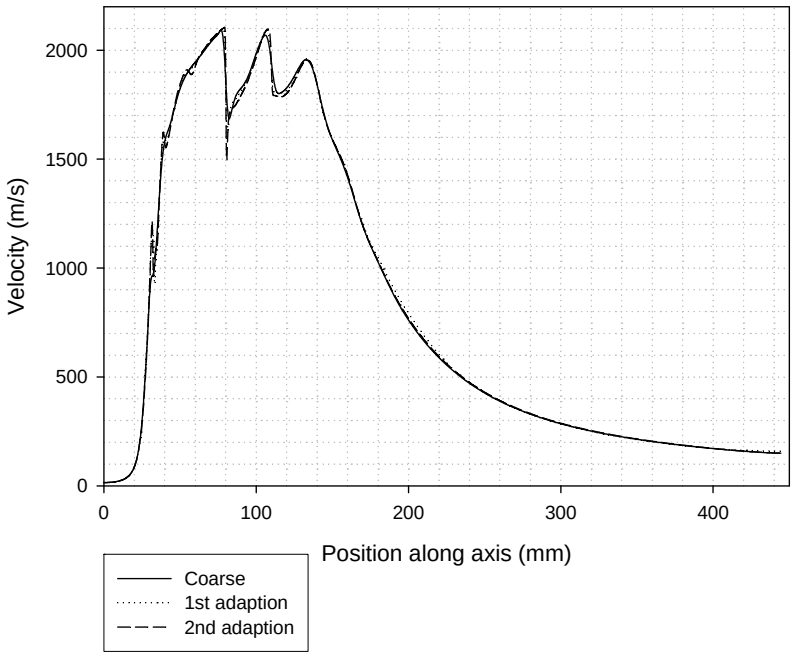

Figure 6.4a: Velocity along nozzle axis, uncooled meshes

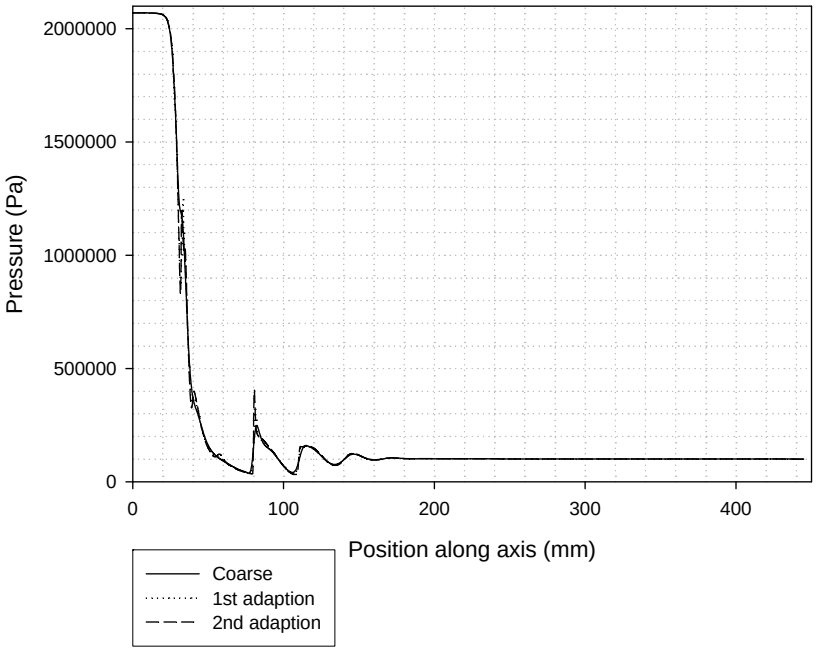

Figure 6.4b: Static pressure along nozzle axis, uncooled meshes

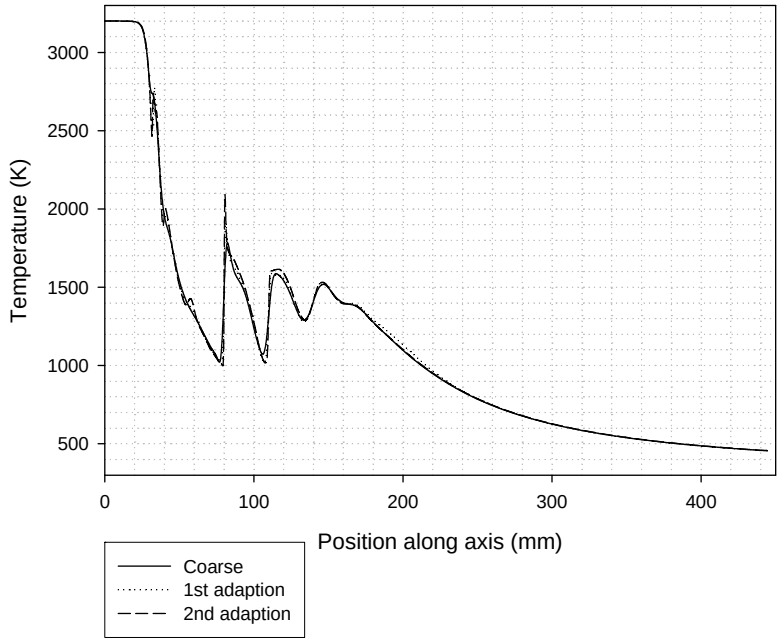

Figure 6.4c: Static temperature along nozzle axis, uncooled meshes

These plots indicate that the three meshes used to model the uncooled nozzle and exhaust jet provide results that are in very close agreement. The differences appear primarily in the region of shocks (the sudden, almost discontinuous jumps visible on the plots), with the most highly adapted mesh providing more definition in these regions. It appears likely that further refinement of the mesh would not be expected to provide a significant improvement in the quality of the results, at least as far as relates to the core flow itself.

Similar plots were then produced using the smaller cooled nozzle mesh depicted in figure 6.2d, but with the cooling channel wall set as an insulating boundary and with air as the working fluid. The results from the most refined of the earlier uncooled meshes are included for comparison, in order to assess whether the truncated mesh used for the cooled nozzle simulations provides reasonably accurate results for the flow within the

nozzle even though the exhaust plume is not included. The resulting plots of velocity, static pressure and static temperature along the nozzle axis are shown in figures 6.5a, 6.5b and 6.5c.

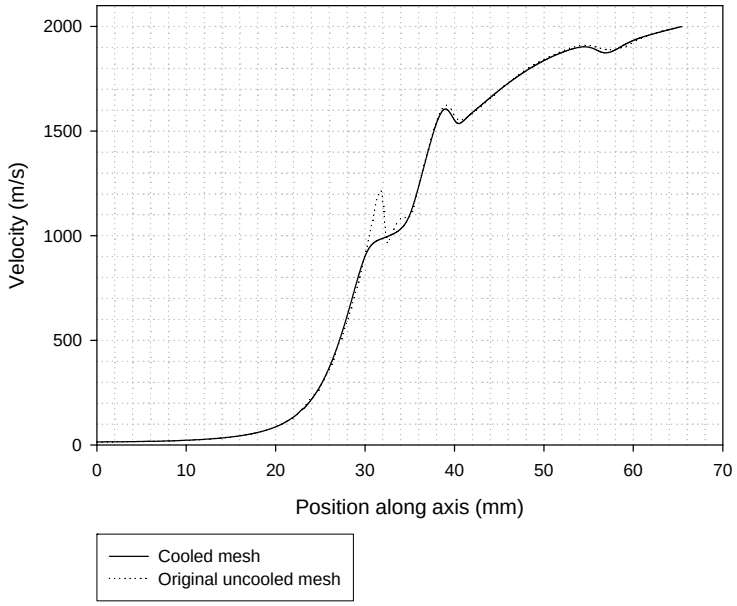

Figure 6.5a: Velocity along nozzle axis, cooled vs. uncooled meshes, air

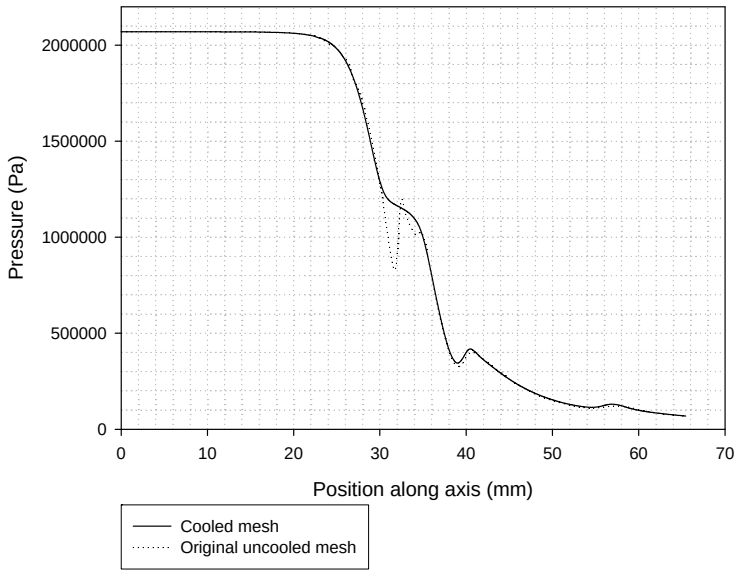

Figure 6.5b: Static pressure along nozzle axis, cooled vs. uncooled meshes, air

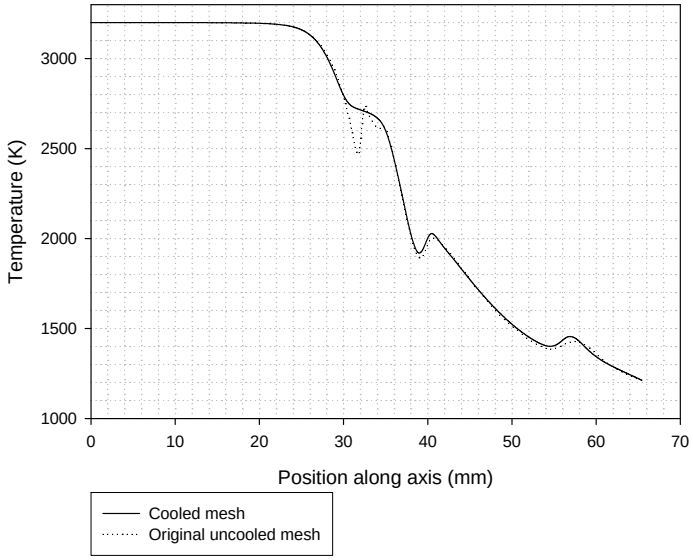

Figure 6.5c: Static temperature along nozzle axis, cooled vs. uncooled meshes, air

These plots suggest very good agreement between the larger, uncooled nozzle mesh including the exhaust plume and the truncated, cooled mesh. The discrepancies between the two are primarily in the vicinity of shocks, which appear to get smoothed out somewhat in the truncated mesh, but this notwithstanding, it seems likely that the truncated, cooled mesh can be expected to provide a reasonably faithful model of the flow within the nozzle.

Proceeding with modeling of the cooled nozzle, the working fluid and the cooling passage wall boundary were changed according to the model described in section 6.2.3. The resulting plot of the flow Mach number contours is shown in Figure 6.6a, while the temperature profile in the nozzle wall is shown in Figure 6.6b.

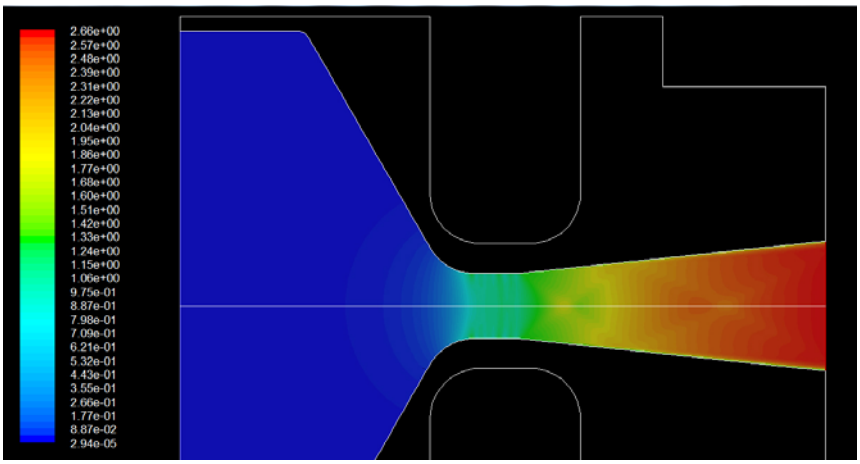

Figure 6.6a: Mach number contours, cooled nozzle

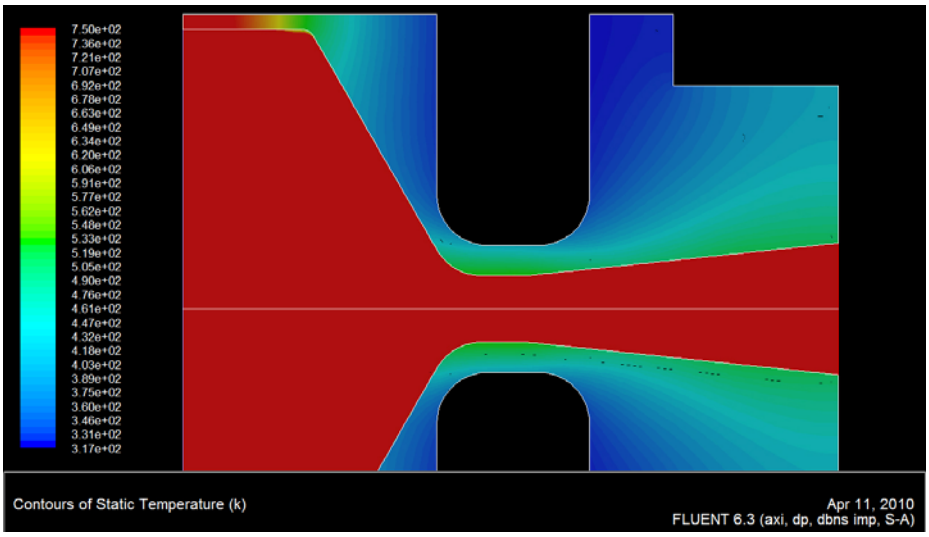

Figure 6.6b: Nozzle wall temperature profile, cooled nozzle

The Mach contours of Figure 6.6a are as would be expected for a conical supersonic nozzle, with the flow becoming sonic in the throat, and the faint pattern of resulting shocks reflecting off the walls of the diverging section. The highest temperature reached in the nozzle throat area was approximately 540 K, suggesting that if the coolant-side convective heat transfer coefficient of 80 000 W/m^2-K can indeed be met, then the nozzle walls in even the region of the throat where the highest heat fluxes occur should remain safely below their designed-for temperature of 773 K.

7. Experimental Data

7.1 Cold Flow

To better characterize the discharge coefficient (C_d) of the injector orifice, the flow rate of water through the orifice was measured at a range of pressure drops. This enables the more accurate setting of engine pressure levels to achieve chamber pressure and oxidizer flow rate requirements.

7.1.1 Theory and Test Methodology

From Sutton and Biblarz (2001)[3], the mass flow rate of an incompressible fluid having density ρ through a sharp-edged orifice of area A may be expressed as:

$$\dot{m} = CA\sqrt{2\rho\Delta p} \tag{7.1}$$

where C is the dimensionless discharge coefficient. It should be noted that this definition of C incorporates both the orifice and the inlet, according to

$$C = \frac{C_d}{\sqrt{1-\beta^4}} \tag{7.2}$$

where C_d is the discharge coefficient of the orifice, neglecting velocity of approach, and β is the ratio of orifice or throat diameter to inlet diameter.

From continuity, the resulting injection velocity may therefore be expressed as

$$U_i = C\sqrt{\frac{2\Delta p}{\rho}} \tag{7.3}$$

It is noted[30] that Equation (7.1) may be modified to account for subsonic gas flow with compressibility effects. This is done by multiplying by an experimentally-determined expansion factor Y:

$$\dot{m} = YCA\sqrt{2\rho\Delta p} \tag{7.4}$$

Y is a function of the ratio of specific heats γ, the ratio of orifice or throat diameter to inlet diameter (β), and the ratio of downstream to upstream absolute pressures.

The ideal method for flow testing would be to include a calibrated mass flow meter in the line upstream of the orifice and feed GOX at the target feed pressure, while maintaining back pressure on the orifice to simulate chamber pressure during normal engine operation. The resulting mass flow rate could then be read directly under conditions that closely approximate the engine's operating conditions. Due to the very high cost of a mass flowmeter, this was not an option for this thesis. C is essentially a constant however, and reasonably accurate results may be obtained by performing a flow test with water over a range of pressures and interpolating the C from this data, so long as the pressure drop across the orifice is not so large that cavitation occurs. In lieu of a flowmeter, the water may be collected over a set period of time, and the average flow rate determined from its weight.

7.1.2 Experimental Setup and Procedure

The apparatus for the tests consisted of a water tank pressurized from a regulated nitrogen cylinder. Downstream of the tank was a pressure gauge and ball valve, with the injector orifice connected via a length of stainless steel braided Teflon flex hose. Water was collected in a bucket, partially covered to reduce losses due to spraying, and a digital scale was used to weigh the water. This setup is illustrated in Figure 7.1.

Figure 7.1: Injector flow test setup

Each test run lasted 45 seconds, and inlet pressures from 10 to 45 psig in 5 psi increments were used. Prior to beginning a given run, the nitrogen regulator was adjusted until the outlet gauge indicated approximately the desired pressure, then the hose and orifice were moved to a second, "spill-over" bucket. The valve was opened, and the regulator was fine-tuned until the gauge reached the desired pressure. Once the pressure was set, the valve was opened and water was allowed to flow into the spill-over bucket until steady flow was observed. The hose was then transferred to the collection bucket and the timer was started. After 45 seconds, the hose was removed from the collection bucket and the valve was closed.

7.1.3 Test Data and Analysis

A plot of the resulting test data is shown in Figure 7.2.

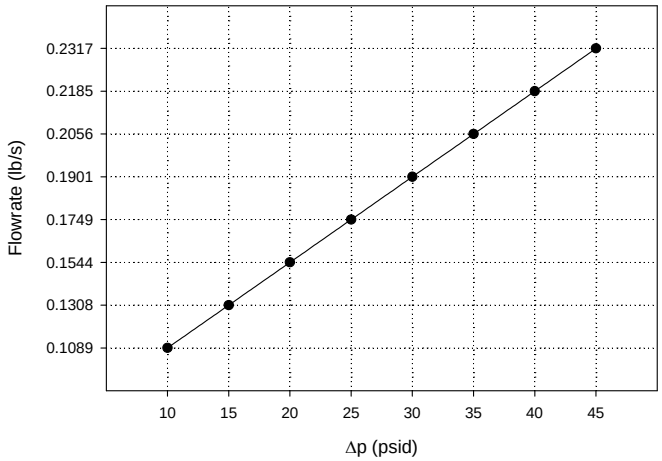

Figure 7.2: Flow test data

To determine the *C*, the mass flow rate in kg/s was plotted as a function of $A_i\sqrt{2\rho\Delta p}$, with A_i = 6.4702x10^{-6} m^2, ρ = 1000 kg/m^3, and Δp converted to units of Pascals. Linear regression was performed on the resulting plot, subject to the constraint that the trendline pass through the origin (zero flow for zero Δp). The resulting plot and trendline are shown in Figure 7.3.

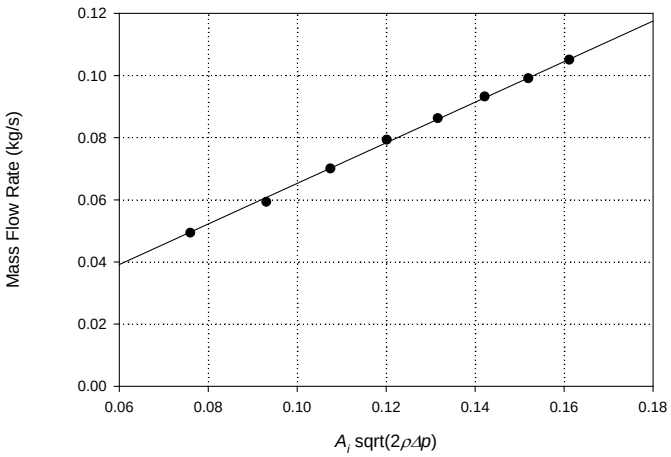

Figure 7.3: Flow test regression analysis

The slope of the trendline, and thus the *C*, is 0.653, with an R^2 value of 0.9988. This is within the expected range for orifices, and is extremely close to the value of 0.65 reported in Sutton and Biblarz (2001)[3] as being typical for a sharp-edged orifice. However, the actual geometry of the orifice being employed is that of a short, straight orifice with conical inlet, and the *C* reported in Sutton and Biblarz (2001)[3] for this type of orifice is typically in the range of 0.8 to 0.84, suggesting that the observed *C* is actually lower than would be expected.

To investigate this discrepancy further, flow rate data was obtained from O'Keefe Controls, the suppliers of the orifice. The O'Keefe data plots the volumetric water flow rate in litres per minute as a function of pressure drop in psi. Converting this to mass flow rate in lbs/s results in the plot of Figure 7.4. The data from Figure 7.1 is included for comparison.

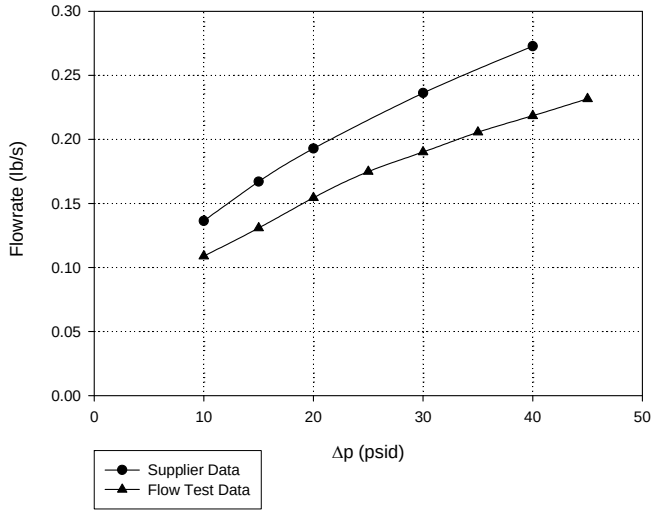

Figure 7.4: Orifice supplier test data

Performing the same regression analysis on the supplier data indicates a *C* of 0.814, which is in keeping with the *C* range in Sutton and Biblarz (2001)[3] for this type of orifice.

Employing Equation (7.3) to determine the pressure drop through the orifice at the HRE's intended mass flow rate of 0.0307 kg/s with $C = 0.814$, $\beta = \frac{0.113\,\text{in}}{0.3125\,\text{in}} = 0.3616$, and a *Y* factor of 0.94 [30] indicates an orifice pressure drop of 79.9 psid, which is in relatively good agreement with (though slightly higher than) the designed-for pressure drop of 72 psid (discussed in Section 5.1). For comparison, performing the same calculation using the *C* value of 0.653 determined from flow testing would suggest a significantly higher orifice pressure drop of 124 psid.

To further complicate the picture, the pressure drop determined from CFD simulation was in the vicinity of 99 psid, falling near the middle of the range between the Δp determined from design (72 psid) and that determined from flow testing.

Given that the *C* value from Sutton and Biblarz (2001)[3], the supplier's orifice flow data, and the theoretical design calculation of Section 5.1 are all in reasonably good agreement and corroborate the supplier-derived *C* of 0.814, it was decided to proceed using this value. In the event that the higher pressure drop predicted from CFD proves to be correct, the engine's performance will be unchanged, as the upstream choking orifice will remain choked and the mass flow rate will thus be unchanged. Hot-fire testing will determine which actual injector pressure drop is closest.

The lower *C* determined from the flow test could be a result of an inaccurate pressure gauge and/or unquantified flow losses in the test apparatus' plumbing between the gauge and the orifice itself. To investigate this, the flow test rig may be modified using a much more precise gauge and locating it immediately upstream of the test orifice, and by using a larger-diameter fitting upstream of the orifice to ensure that the flow upstream of the orifice is essentially stagnated. Unfortunately time constraints did not allow for further investigation of this.

7.1.4 Additional Cold Flow Testing

In addition to component-level orifice testing, cold flow testing was also performed on the system level. The entire feed system was initially pressurized with dry nitrogen (N_2) to 300 psig and observed for leaks. This was followed by the use of a low flow of N_2 through the main GOX line to set the main regulator to its required operating pressure, and a full pressure flow test running N_2 through the engine to test control systems, sensors, and confirm the absence of any leakage in the combustion chamber itself.

7.2 Hot Firings

As of the time of writing, the integration of the HRE and fire control system components was still underway and hot fire testing was still pending. Accordingly, the results of these firings and their analysis will remain as the subject of future work. It may be noted however that the initial hot fire testing is planned to proceed in two stages.

The first "hot" testing to be performed will involve the engine's ignition system. This will involve a series of runs at different ignition oxygen flow rates to ascertain the optimal flow rate for smooth fuel grain ignition. Initially, ignition is to be achieved by initiating a low GOX flow and passing current through medium-fine steel wool impregnated with paraffin. This method offers both simplicity and low cost. For future work, a torch igniter using a spark plug to ignite a fuel-rich mixture of GOX and propane is being considered. This would add the convenience of a reusable igniter permanently integrated into the HRE's head end, and also allow a "re-start" capability that is not achievable using a single-use steel wool igniter.

Having completed ignition system testing, full engine tests will proceed. Initial testing will involve both polyethylene and paraffin fuel grains with a target burn duration between 3 and 6 seconds. In addition to verifying the overall functionality of the complete laboratory-scale HRE system, a key objective of these firsts tests will be to investigate the erosion of the graphite nozzle, particularly in the region of the throat, and assess its suitability for additional firings, possibly of longer duration. The fuel grains

will also be removed and dissected after these tests for the estimation of regression rates and stoichiometric length considerations.

8. Conclusion and Recommendations for Future Work

8.1 Final Remarks

The construction of a complete hybrid rocket engine test facility has been completed as part of this thesis project. This component of the thesis represented a complex, multidisciplinary development program by the author and other parties involved, and covered a broad range of subsystems, and its final outcome has been a robust and flexible experimental hybrid rocket engine that can act as a platform for a number of experiments, a comprehensive and flexible oxidizer feed system, a strong but portable test stand, and comprehensive instrumentation.

While the multidisciplinary nature of this project meant that there were a great many subsystems that required detailed design consideration, particular focus was placed on the design and analysis of two of the most critical components, namely, the GOX injector and the nozzle.

Injector design, driven by system-level design considerations, was carried out using an analytical approach for the selection of an orifice with the desired flow characteristics and supplementing this with CFD modeling and experimental cold-flow testing to verify the orifice pressure drop required to achieve the design GOX mass flow rate. While the results of the CFD simulation and the cold-flow testing differed and were thus inconclusive, they highlighted both the fact that the flow through such a small orifice is very sensitive to the precise geometry of the flow path, as well as the need for further

experimental testing using carefully-designed, precision equipment. At the same time, the incorporation of a choking orifice upstream of the injector has ensured that the system will be robust enough to maintain the designed-for GOX flowrate even if the actual orifice pressure drop proves to lie near the higher end of its range.

The nozzle design was likewise driven by system-level considerations, as well as by the challenges of precision manufacturing on the small scale. Time and budgetary constraints precluded the completion of a water-cooled nozzle, but it is expected that the current uncooled graphite version will provide adequate performance for initial test firings of reasonably short duration. At the same time, the basic design of the cooled nozzle was completed analytically, and CFD results appear to confirm its soundness.

On the systems level, the design of the experimental engine and all support equipment was specifically intended to allow for its use over a wide range of operating conditions, and this has been achieved. As such, this experimental capability will provide a unique ability for the gathering of valuable data related to the fundamental processes of hybrid rocket engine performance and enabling the further corroboration and refinement of internal ballistics models, as well as enabling the evaluation of different fuels, materials, and specific critical hardware components for use in practical hybrid rocket engine systems. Further work building on the foundation that has been laid in the present thesis project is discussed in the following section.

8.2 Recommendations for Future Work

The most immediate further work, much of which is currently in progress, will involve additional cold-flow injector testing using a more precise test rig, the final integration of all the components of the HRE system, and the first series of test firings to verify system functionality and examine the durability of the graphite nozzle.
The completion of the design and fabrication of the water-cooled nozzle that was considered in this thesis would be another worthwhile project.

Fundamentally though, this thesis project has provided a basic experimental capacity that enables an extensive range of research into many different aspects of engineering.
The study of the diffusion flame combustion processes that occur in an HRE offers multiple avenues for research, and because these processes are so strongly coupled to the oxidizer flow, the investigation of a range of injector concepts would be a similarly fruitful area of endeavour. Multiple different propellant combinations may similarly be investigated. And as experimental data is obtained, this provides opportunities for refining the basic models of the phenomena associated with hybrid rocket combustion.

In addition to its value as a tool for basic combustion research, this experimental facility and the data it generates will be of use in the development of larger hybrid rocket engines and the investigation of the associated scaling effects, and will allow for the assessment and reduction of risk for a more comprehensive research and development effort in this regard.

As our awareness of the fragility of our planet's environment continues to grow, the need for further research and the vital role of space-based assets in that research has never been greater. Going hand in hand with this is the need for further research towards a truly cost-effective and environmentally benign means of launching these payloads, and simple hybrid rocket engines offer significant promise towards achieving this.

References

1. Humble, R.W., Henry, G.N. and Larson, W.J. 1995. *Space Propulsion Analysis and Design.* McGraw-Hill, New York

2. Chiaverini, M.J. and Kuo, K.K. 2007. *Fundamentals of Hybrid Rocket Combustion and Propulsion.* American Institute of Aeronautics and Astronautics, Inc., Reston, VA,

3. Sutton, G.P. and Biblarz, O. 2001. *Rocket Propulsion Elements, 7th ed.* Wiley & Sons, New York

4. Zilliac, G. and Karabeyoglu, M.A. 2006. Hybrid Rocket Fuel Regression Rate Data and Modelling. *AIAA/ASME/SAE/ASEE 42nd Joint Propulsion Conference*, AIAA Paper No. 2006-4504.

5. Karabeyoglu, A., Zilliac, G. Cantwell, B., De Zilwa S. and Castelluci, P. 2004. Scale-Up Tests of High Regression Rate Paraffin-Based Hybrid Rocket Fuels. *Journal of Propulsion and Power*, Vol 20., No. 6.

6. Karabeyoglu, M. A., Altman, D. and Cantwell, B.J. 2002. Combustion of Liquefying Hybrid Propellants: Part I General Theory. *Journal of Propulsion and Power*, Vol. 18, No 3, pp. 610-620.

7. Greatrix, D.R. 2007. Model for Predicting Fuel Regression Rate in Hybrid Rocket Engines. *AIAA/ASME/SAE/ASEE 43rd Joint Propulsion Conference*, AIAA Paper No. 2007-5346.

8. Greatrix, D.R. 2009. Regression Rate Estimation for Standard-Flow Hybrid Rocket Engines. *Aerospace Science & Technology*, Vol. 13, No. 7, pp. 358-363.

9. Greatrix, D.R. 2002. Hybrid Rockets – Internal Ballistic Modelling Considerations, *CSME Forum*, Kingston (Ontario), May 21-24 (conference proceedings, thermal systems).

10. Schulze, K.W. and Meyer, S.A. 1993. The Rapid and Low Cost Development of a Hybrid Rocket Motor. *AIAA/ASME/SAE/ASEE 29th Joint Propulsion Conference*, AIAA Paper No. 1993-2610.

11. Luchini, C.B., Wynne, P., Hudson, M.K. and Rooke, S. 1996. Hydrocarbon hybrid rocket fuel regression rate studies. AIAA/ASME/SAE/ASEE 32nd Joint Propulsion Conference, AIAA Paper No. 1996-2595.

12. Yuasa, S., Shimada, O., Imamura, T., Tamura, T. and Yamamoto, K. 1999. A Technique for Improving the Performance of Hybrid Rocket Engines. AIAA/ASME/SAE/ASEE 35th Joint Propulsion Conference, AIAA Paper No. 1999-2322.

13. Tamura, T., Yuasa, S. and Yamamoto, K. 1999. Effects of Swirling Oxidizer Flow on Fuel Regression Rate of Hybrid Rockets. AIAA/ASME/SAE/ASEE 35th Joint Propulsion Conference, AIAA Paper No. 1999-2323.

14. Corpening, J.H., Palmer, R.K. and Heister, S.D. 2003. Combustion of Advanced Non-Toxic Hybrid Propellants. AIAA/ASME/SAE/ASEE 39th Joint Propulsion Conference, AIAA Paper No. 2003-4596.

15. Karabeyoglu, M.A., Cantwell, B.J. and Altman, D. 2001. Development and Testing of Paraffin-Based Hybrid Rocket Fuels. AIAA/ASME/SAE/ASEE 37th Joint Propulsion Conference, AIAA Paper No. 2001-4503.

16. Grosse, M. 2009. Effect of a Diaphragm on Performance and Fuel Regression of a Laboratory Scale Hybrid Rocket Motor Using Nitrous Oxide and Paraffin. AIAA/ASME/SAE/ASEE 45th Joint Propulsion Conference, AIAA Paper No. 2009-5113.

17. Einav, O., Peretz, A., Hashmonay, B., Birnholz, A. and Sobe, Z. 2009. Development of a Lab-Scale System for Hybrid Rocket Motor Testing. AIAA/ASME/SAE/ASEE 45th Joint Propulsion Conference, AIAA Paper No. 2009-4888.

18. Carmicino, C., Orlandi, O., Russo Sorge, A., Dauch, F., De Amicis, R. and De Rosa, M. 2009. Basic Aspects of the Hybrid Engine Operation. AIAA/ASME/SAE/ASEE 45th Joint Propulsion Conference, AIAA Paper No. 2009-4937.

19. Connell, T. L., Santi, S.A., Risha, G.A., Muller, B.A. and Batzel, T.D. 2009. Experiment and Semi-Empirical Modeling of Lab-Scale Hybrid Rocket Performance. AIAA/ASME/SAE/ASEE 45th Joint Propulsion Conference, AIAA Paper No. 2009-5086.

20. Karabeyoglu, A., Zilliac, G. Cantwell, B., De Zilwa S. and Castelluci, P. 2004. Scale-Up Tests of High Regression Rate Paraffin-Based Hybrid Rocket Fuels. *Journal of Propulsion and Power*, Vol 20., No. 6.

21. Nakagawa, I., Hikone, S. and Suzuki, T. 2009. A Study on the Regession Rate of Paraffin-based Hybrid Rocket Fuels. AIAA/ASME/SAE/ASEE 45th Joint Propulsion Conference, AIAA Paper No. 2009-4935.

22. Gordon, S. and McBride, B. J. 1994. Computer Program for Calculation of Complex Chemical Equilibrium Compositions and Applications. NASA RP-1311.

23. Dornheim, M.A. "Ideal Hybrid Fuel Is... Wax?" Aviation Week and Space Technology, 20 Feb. 2003. Print.

24. Streeter, V.L. and Wylie, E.B. 1985. *Fluid Mechanics, 8th ed.* Wiley & Sons, New York, p. 215.

25. Yang, V., Habiballah, M., Hulka, J. and Popp, M. 2004. *Liquid Rocket Thrust Chambers: Aspects of Modeling, Analysis, and Design*. American Institute of Aeronautics and Astronautics, Reston, VA., pp.51-53.

26. ANSYS, Inc. 2006. *FLUENT 6.3 User's Guide*, Section 12.3.1. Electronic.

27. Bartz, D.R. 1957. A simple equation for rapid estimation of rocket nozzle convective heat transfer coefficients. *Jet Propulsion*, Vol. 27 No.1, pp.49-51.

28. Huzel, D.K. and Huang, D.H. 1992. *Modern Engineering for Design of Liquid-Propellant Rocket Engines.* American Institute of Aeronautics and Astronautics, Washington, DC., p.86

29. ANSYS, Inc. 2006. *FLUENT 6.3 User's Guide*, Section 25.5.3. Electronic.

30. Crane Co. 1999. *Flow of Fluids Through Valves, Fittings, and Pipe.* Technical Paper No. 410M. Crane Valves North America, Woodlands, TX.